UNIVERSIDADE FEDERAL DO CEARÁ

CENTRO DE TECNOLOGIA

DEPARTAMENTO DE ENGENHARIA ESTRUTURAL E CONSTRUÇÃO CIVIL

PROGRAMA DE PÓS-GRADUAÇÃO EM ENGENHARIA CIVIL

MESTRADO ACADÊMICO EM ENGENHARIA CIVIL

RENAN MELO BARROS

AN ISOGEOMETRIC FORMULATION FOR MATERIAL AND GEOMETRIC NONLINEAR ANALYSIS OF FUNCTIONALLY GRADED PLATES

FORTALEZA

2023

RENAN MELO BARROS

AN ISOGEOMETRIC FORMULATION FOR MATERIAL AND GEOMETRIC NONLINEAR
ANALYSIS OF FUNCTIONALLY GRADED PLATES

Dissertation submitted to the Programa de
Pós-Graduação em Engenharia Civil of the
Centro de Tecnologia of the Universidade
Federal do Ceará, as a partial requirement for
obtaining the title of Master of Science in Civil
Engineering. Concentration area: Structural
Engineering

Advisor: Prof. D. Sc. Evandro Parente
Júnior

Co-advisor: Prof. D. Sc. Marcelo Silva
Medeiros Junior

FORTALEZA

2023

RENAN MELO BARROS

AN ISOGEOMETRIC FORMULATION FOR MATERIAL AND GEOMETRIC NONLINEAR
ANALYSIS OF FUNCTIONALLY GRADED PLATES

> Dissertation submitted to the Programa de
> Pós-Graduação em Engenharia Civil of the
> Centro de Tecnologia of the Universidade
> Federal do Ceará, as a partial requirement for
> obtaining the title of Master of Science in Civil
> Engineering. Concentration area: Structural
> Engineering

Approved on: 20 de Dezembro de 2023

EXAMINATION BOARD

_____

Prof. D. Sc. Evandro Parente Júnior   (Advisor)
Universidade Federal do Ceará (UFC)

_____

Prof. D. Sc. Marcelo Silva Medeiros
Junior   (Co-advisor)
Universidade Federal do Ceará (UFC)

_____

Prof. Dr. Severino Pereira Cavalcanti Marques
Universidade Federal de Alagoas (UFAL)

_____

Prof. Dr. Luiz Antonio Taumaturgo Mororo
Universidade Federal do Ceará (UFC)

Aos meus pais, Eduilton e Claudia, meus maiores incentivadores.

ACKNOWLEDGEMENTS

"Any moment might be our last. Everything is more beautiful because we're doomed. You will never be lovelier than you are now. We will never be here again."

(Homer, *The Iliad*)

ABSTRACT

Composite materials recent spotlight is due to presenting a wide range of applications throughout many industries. Functionally Graded Materials (FGM) are a specific class of composites, presenting a smooth and continuous volume fraction gradation of their constituents. Due to the modernization of both machinery and methodologies associated to their fabrication, the FGM are receiving a growing attention in academic research. Functionally Graded Materials effective elastic properties vary along with the volume fractions, being evaluated by the employment of adequate micromechanical models. Due to the associated complexity, the development of analytical solutions for FGM problems is usually impossible. Thus, it is necessary to employ computational methods in order to obtain approximated solutions, such as the Finite Element Method (FEM) and the Isogeometric Analysis (IGA). This work employs both geometric nonlinearity, to include the structural effect of large displacements, and material nonlinearity, to allow the consideration of elastoplastic behavior. Regarding FG structures, the Tamura-Tomota-Ozawa model is used to estimate the effective plastic properties. Therefore, a 3D formulation that enables the consideration of tridirectional gradation for solids of any geometry is presented. Regarding plate problems, kinematic structural theories are used to enhance the model analysis efficiency. In this work, a novel NURBS-based Quasi-3D isogeometric formulation using a degenerated solid approach is developed. By presenting an integration over the volume, the same material nonlinearity algorithms for 3D models can be adopted. The presented formulations are employed in multiple types of analyses, considering multiple geometries, boundary conditions, FGM constituents and volume fraction profiles. Numerical examples present a close agreement with the literature for every formulation. Results show that the novel Quasi-3D approach is able to accurately represent both material and geometric nonlinear behavior in FG plates.

Keywords: functionally graded materials; isogeometric analysis; quasi-3D plate theory; tamura-tomota-ozawa model.

RESUMO

O grande interesse nos materiais compósitos resulta de sua vasta gama de aplicações em diversas indústrias. Materiais com Gradação Funcional (MGF) são uma classe específica de compósitos, que apresentam uma variação suave e contínua da fração de volume dos seus componentes. Devido à modernização dos equipamentos e metodologias associadas a sua fabricação, os MGF estão recebendo uma crescente atenção de pesquisas acadêmicas. As propriedades efetivas dos MGF variam junto com as frações de volume, sendo estimadas por meio de modelos micromecânicos adequados. Devido à sua complexidade, desenvolvimento de soluções analíticas para problemas de MGF é geralmente impossível. Portanto, é necessário o uso de métodos computacionais para se obter uma resposta aproximada, como o Método dos Elementos Finitos e a Análise Isogeométrica. Esse trabalho considera tanto a não-linearidade geométrica, para grandes deslocamentos, quanto a física, para comportamento elastoplástico. No que tange a estruturas com gradação funcional, o modelo de Tamura-Tomota-Ozawa é empregado para estimar as propriedades plásticas efetivas. Dessa forma, uma formulação 3D que permite gradação tridirecional para sólidos de qualquer geometria é apresentada. Focando em estruturas de placas, teorias cinemáticas são usadas para melhorar a eficiência do modelo de análise. Neste trabalho, uma nova abordagem de teoria Quasi-3D com formulação isogeometrica baseada em NURBS e utilizando o modelo de sólido degenerado é apresentada. Por apresentar uma integração sobre o volume, os mesmos algoritmos para análise elastoplástica 3D podem ser adotados. As formulações apresentadas são empregadas em diversos tipos de análise, considerando múltiplas geometrias, condições de contorno, constituintes de MGF e perfis de gradação. Exemplos númericos apresentam boa concordância com a literatura para cada formulação. Os resultados mostram que a formulação proposta é capaz de representar de forma acurada os comportamentos não-lineares físico e geométrico de placas com gradação funcional.

Palavras-Chave: materiais com gradação funcional; análise isogeométrica; teoria de placas quasi-3D; modelo de tamura-tomota-ozawa.

LIST OF FIGURES

LIST OF TABLES

CONTENTS

1   INTRODUCTION

Composites are designed by combining two or more materials at a macroscopic scale to create a new material with desirable physical properties that the individual components alone could not achieve[1, 2]. Due to their characteristics, these materials have been extensively explored within the literature, being applied across various industries, including aeronautics, naval and microelectronics[3, 4].

Functionally Graded Materials (FGM) represent an advanced class of composites, featuring a gradual and continuous variation of its constituents[5, 6]. This unique characteristic helps prevent stress concentrations and delamination experienced by laminates. Even though FGMs can be found in nature, the first manufactured composite was developed in 1984 by Japanese researchers, as a requirement of the aerospace program for a material capable of withstanding high temperature gradients whilst maintaining the desired stiffness[7].

Despite initially developed to address problems with temperatures and thermal gradients, the employment of FGMs has expanded to encompass diverse industries, including energy and electronics, assuming diversified functions and applications. Consequently, recent research regarding FGM has focused on exploring different fields of application[8, 9, 10], being a popular literature topic.

Functionally Graded Materials are commonly modeled as particulate composites with a variable concentration of inclusions[6, 11, 12]. Given their composite nature, homogenization methods can be applied to enhance the accuracy of material modeling across the gradation[13]. Consequently, effective properties are computed using micromechanical models, being evaluated within the structural domain in terms of the constituents' volume fractions[14, 15]. Despite the tendency to overlook this aspect observed in many related studies, the choice of the micromechanical model plays a crucial role in the analysis of FG structures, significantly impacting the obtained results[16, 14].

Furthermore, the Metal Matrix Composites (MMC) are the most popular FGM modeling type within the literature, generally adopting metal and ceramic constituents. However, other kinds of FGM can be manufactured, such as Carbon Nanotubes Reinforced FGM (CNTRC-FG)[17, 18] and Porous FGM[19, 20]. These composites exhibit slightly distinct properties compared to the usual matrix-inclusion FGM. As a result, the utilization of these advanced materials requires the development of accurate analysis methods to fully explore their potential.

In a broad sense, the analysis of Functionally Graded structures, given their complex

characteristics, cannot be carried out using analytical approaches. Thus, computational methods such as the Finite Element Method (FEM) and the Isogeometric Analysis (IGA)[21, 22] are employed in order to obtain approximate results. FEM has been the predominant computational method globally for quite some time. In contrast, IGA has been recently developed and is not typically adopted by commercial analysis software. However, it presents advantages over FEM, being able to exactly represent the structure geometry regardless the mesh refinement and to easily generate high continuity basis functions[21, 23].

Given the reliance on computational methods for the analysis process, it is crucial to maintain the model as close to reality as possible to ensure a good approximation. Even though many studies account for the geometric nonlinearity of Funtionally Graded structures [23, 24, 25, 26], way less consider the material nonlinearity[27, 28]. Neglecting these effects can be detrimental to accuracy, as the structural load-carrying capacity depends on the consideration of both types of nonlinearities.

While it is conceivable to model every structure as a 3D body, certain conditions, such as geometry or applied loads, might result in numerically negligible strains and stresses components. In this context, a dimensional reduction to a 2D or 1D model is possible, enhancing computational efficiency and simplifying both geometric modeling and the imposition of essential boundary conditions. This reduction can be achieved through the application of structural kinematic theories[29], resulting in plate, shell and beam models.

Concerning plates, two commonly employed kinematic theories are the Classical Plate Theory (CPT)[1], which entirely disregards transverse shear strains, and the First-order Shear Deformation Theory (FSDT)[30], which assumes shear strains to be constant through the thickness, requiring the use of a shear correction factor to achieve more accurate approximations. Both CPT and FSDT are implemented in commercial analysis programs.

Considering the possibility of material gradation along the thickness direction in Functionally Graded structures (FGMs), the use of High-order Shear Deformation Theories (HSDTs)[29] is advisable. They account for variable transverse shear strains across the thickness, aligning with the principles of the Continuum Mechanics. Regarding the literature in terms of kinematic assumptions, geometric nonlinearity is usually considered. However, in terms of constitutive relations, the accounting of material nonlinearity - specially for FG plate structures - could hardly be found in the bibliographical review conducted for this work: Moita et al.[31] used an HSDT with the Tamura-Tomota-Ozawa (TTO) to account for material nonlinearity in

FG plates, while Sharma and Kumar[32] used a shell formulation along with the TTO for FG plates subjected to thermomechanical loads.

An alternative approach involves adopting a Quasi-3D kinematic theory for the analysis of FG plates[33, 34, 35, 36, 37]. This theory shares considerations regarding geometric nonlinearity and transverse shear strains with High-order Shear Deformation Theories (HSDTs). However, it presents the distinctive feature of accounting for the thickness stretching[38]. This allows the Quasi-3D formulation to provide a general state of stress, making possible the use of 3D constitutive relations. Consequently, this characteristic facilitates the consideration of elastoplasticity in plate models.

Regarding the Quasi-3D literature, to the best of the author's knowledge, despite numerous studies presenting various methodologies, none of them have utilized an Isogeometric analysis approach for a polynomial formulation. Additionally, due to being based on a plate model, the mathematical development in these works is often framed in terms of internal forces, which is not suitable for capturing the elastoplastic behavior.

Given this context, this work develops a novel NURBS-based Reddy's Quasi-3D formulation, which adopts a degenerated solid approach and serves as an alternative for the elastoplastic analysis of FG plates. Additionally, a general geometric nonlinear 3D formulation for the elastoplastic analysis of Functionally Graded structures is also introduced.

1.1 Aims and scope

This work aims to establish a methodology for material and geometric nonlinear analysis of Functionally Graded structures, with a specific focus on plates. Considering the aforementioned purpose, the specific aims of this work are:

(a) Develop a general isogeometric formulation for the analysis of FG solids featuring tridirectional gradation;

(b) Establish a methodology for conducting elastoplastic and geometric nonlinear analysis of FG 3D models;

(c) Propose a novel NURBS-based approach for elastoplastic and geometric nonlinear analysis of FG plates using the Reddy's Quasi-3D theory;

(d) Compare the results obtained by the proposed Quasi-3D formulation against those from the 3D model and other existing plate theories;

(e) Assess the accuracy and efficiency of different structural theories to FG plates with varying

geometries, boundary conditions, micromechanical models and constituents.

1.2 Organization of the text

The subjects covered in this work are presented as follows. The second chapter discusses the fundamental concepts and applications of Functionally Graded structures. Additionally, the chapter provided an overview of the evaluation of elastoplastic properties.

The third chapter describes the kinematic theory and constitutive relations employed for simulating the elastoplastic and geometric nonlinear behavior of 3D models. This includes a general formulation and its specialization for an isogeometric approach.

The fourth chapter introduces a novel NURBS-based approach for the Reddy's Quasi-3D theory and discusses its specialization to simpler kinematic theories. It also outlines the constitutive relations used to consider the elastoplastic behavior on FG plate models.

The fifth chapter presents the numerical examples, assessing the accuracy and performance of the proposed Quasi-3D approach. The general 3D formulation is validated and employed to establish benchmarks, while other plate theories serve as an additional source of validation and comparison for FG structures.

Finally, the sixth chapter presents the concluding remarks of this work and suggestions for future research.

2 FUNCTIONALLY GRADED MATERIALS OVERVIEW

Functionally Graded Materials are composites characterized by a gradual and continuous variation in their composition, changing the volume fraction of constituents along a specified direction. This distinctive feature allows a regular stress distribution profile within the structure, mostly preventing the occurrence of stress concentration. Consequently, the employment of FG structures avoid some common failure mechanisms presented by the laminated composites[5, 1]. An example of an FG plate is shown in Fig. 1.

While some natural materials, like bamboos, human bones and skin, present a gradation of their properties, the concept of FGM was first conceived in a laboratory environment in 1984 by Japanese researchers. They were seeking for a material capable of bear extreme temperatures while providing the necessary mechanical strength for aerospace structures, effectively serving as a thermal barrier. Nowadays, FGMs find application in various industries, such as energy, aerospace, biomedical, ballistic and electronics[39, 7, 10]. A realistic FGM model can be seen in Fig. 2.

FGMs are typically composed of ceramic inclusions, presenting high stiffness and thermal resistance, embedded in a metallic matrix, which provides high toughness and ductility to achieve the desired properties. Common materials used for the ceramic inclusions are silicon nitride (Si_3N_4), aluminum oxide (Al_2O_3), and silicon carbide (SiC), whereas the ones for the metallic matrix are stainless-steel (SUS304), aluminum alloys (Al), and titanium (Ti). It is worth noting that ongoing research studies other types of FGMs, including porous and Carbon Nanotube reinforced FGMs.

Figure 1 – Functionally graded plate.
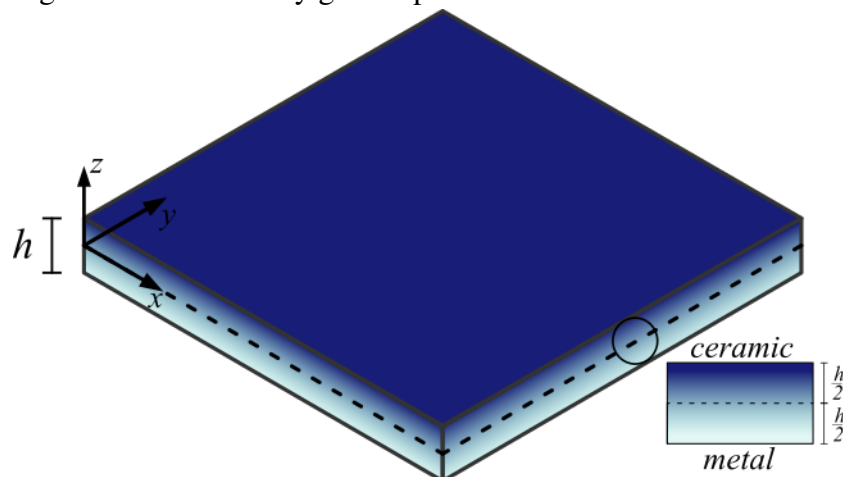
Source: The author.

Figure 2 – Functionally graded composite.
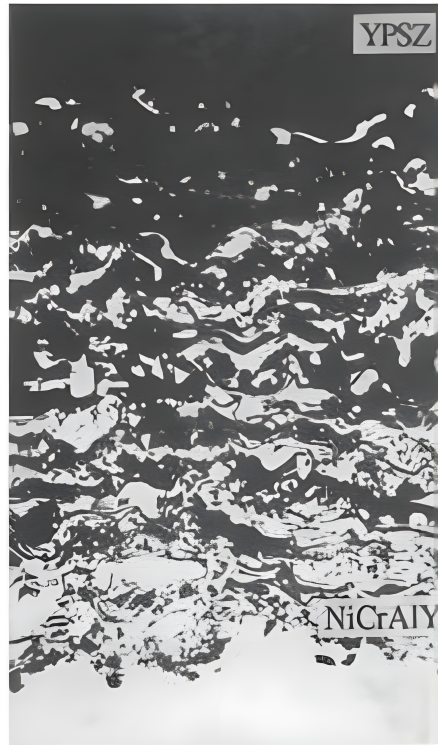
Source: Shiota and Miyamoto[40].

Despite the growing global interest in Functionally Graded structures, it is important to remark that experimental results for these materials remain limited due to the high cost associated with their fabrication, as the manufacturing process often involves a complex set of techniques.

2.1 Volume fraction profile

The gradation profiles are determined by the distribution of the volume fractions of their constituents, often described by closed-form equations. The most employed equation in the literature to define the gradation profile is the Power-Law function, or P-FGM[5, 41, 42]:

$$V_c = V_{c,b} + (V_{c,t} - V_{c,b})\left(\frac{1}{2} + \frac{z}{h}\right)^N \tag{2.1a}$$

$$V_m = 1 - V_c \tag{2.1b}$$

where the subscripts c and m are referring to ceramic and metal, respectively, while $V_{c,t}$ and $V_{c,b}$ are the ceramic constituent volume fractions at the top and bottom of the structure. Many profiles can be achieved for the same constituents by varying the exponent N, which is referred to as

Figure 3 – Volume fraction gradation profiles.

(a) P-FGM   (b) S-FGM
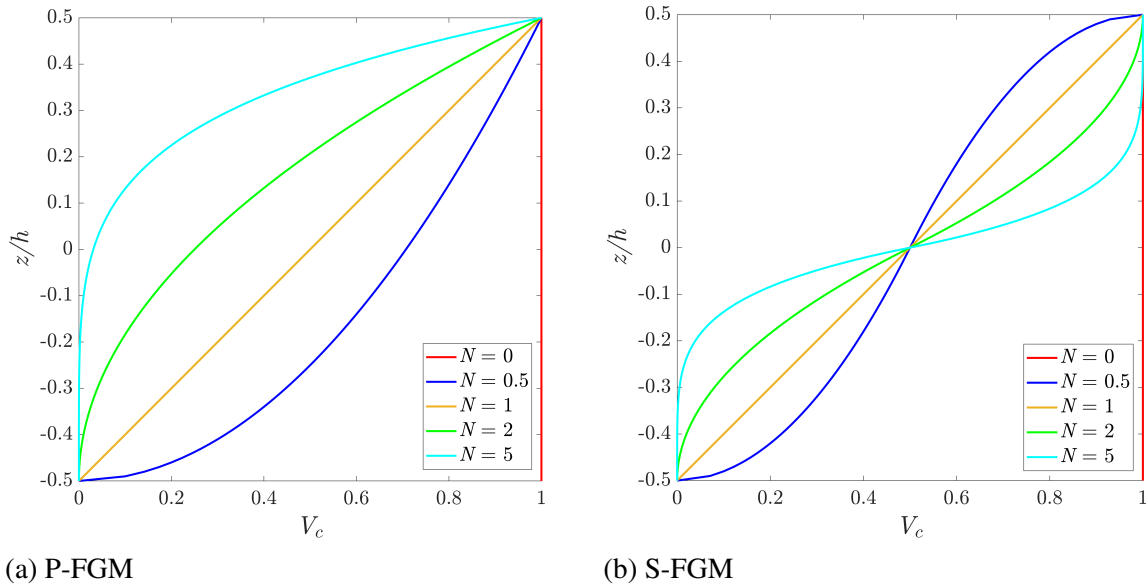
Source: The author.

non-homogeneity index.

It can be noted that for $N = 0$, the FGM matches the ceramic constituent, whilst for $N \to \infty$ the FGM resembles the metallic constituent. Additionally, it is important to mention that although many studies consider $V_{c,t} = 1$ and $V_{c,b} = 0$, a more realistic approximation for the lowest metallic matrix volume fraction would be around 30%, reflecting the practical requirements of fabrication processes[13].

Alternatively, various other equations can be employed to simulate the gradation profile. One of these equations is the sigmoid (S-FGM) function, which generates an S-shaped curve. It can be preferred due to providing a smoother gradation when compared to the P-FGM function, especially in the regions near to the top and bottom surfaces, ensuring that there are no abrupt changes in the volume fraction. It can be computed as:

$$V_c = \begin{cases} V_{c,b} + (V_{c,t} - V_{c,b})\left(1 - \frac{1}{2}\left(\frac{h-2z}{h}\right)^N\right), & 0 \leq z \leq \frac{h}{2} \\ V_{c,b} + (V_{c,t} - V_{c,b})\left(\frac{1}{2}\left(\frac{h-2z}{h}\right)^N\right), & -\frac{h}{2} \leq z \leq 0 \end{cases} \tag{2.2}$$

Fig. 3 illustrates the distinct gradation profiles obtained for different equations and multiple exponents N. In this work, the adopted profile is the P-FGM.

In addition to these methods, some authors have adopted the basis functions used by the computational method, as Hermite polynomials for the Finite Element Method and B-Splines functions for the Isogeometric analysis[43, 44]. This approach can be beneficial for optimization

problems, as it enhances the design flexibility, and also for problems that require a symmetrical profile, which can be trivially achieved.

2.2 Effective properties

Once the gradation profile is defined, the effective properties are expected to vary along with volume fraction. In order to determine how this variation occurs, micromechanical models can be employed. They are homogenization techniques that evaluate the macroscopic elastic effective properties in terms of the physical properties and volume fraction of each phase (metallic matrix and ceramic inclusions).

The simplest micromechanical schemes are the Reuss[45] and Voigt[46] models, with the Voigt model, also known as Rule of Mixtures, being the most widely used in the literature. It assumes an uniform strain field for both the matrix and inclusions, allowing the properties to be evaluated by:

$$P(z) = \sum_{i=1}^{n} P_i V_i(z) \tag{2.3}$$

where P_i is the material property and V_i is the associated volume fraction. The Voigt model resembles a linear weighted average between the properties of each constituent, providing a straightforward method for determining the effective properties for the FGM. On the other hand, the Reuss model assumes that the phases are subjected to a uniform stress field. The properties are obtained by:

$$\frac{1}{P(z)} = \sum_{i=1}^{n} \frac{V_i(z)}{P_i} \tag{2.4}$$

The high simplicity of both models is achieved by neglecting important parameters, such as the shape and orientations of inclusions. Therefore, although they are commonly used, the Rule of Mixtures often leads results that are not in good agreement with available experimental data[14, 47]. Using this model may simulate stiffer structures, underestimating stresses and strains, which can compromise structural safety. Consequently, the Voigt and Reuss models are used to establish, respectively, extreme upper and lower bounds for the evaluation of effective properties across the entire range of inclusion volume fractions[14, 48].

To mitigate the issues mentioned above, other micromechanical models are available, including the the Mori-Tanaka, the Hashin-Shtrikman bounds and the Self-Consistent Method, which can be employed for more accurate predictions[15, 49].

The Hashin-Shtrikman bounds adopt a different approach compared to the Voigt and Reuss models. They incorporate auxiliary fields to represent deviations from a chosen reference solution. This approach minimizes the impact of possible errors presented by the approximations on the final results[48, 49], resulting in a narrower range for the evaluation of effective properties and enhancing the precision of homogenization procedure.

The lower Hashin-Shtrikman boundary involves considering the softer constituent as the matrix phase. In the case of a matrix phase being reinforced by randomly distributed spherical particles, the volume fraction profile is employed to evaluate the bulk (K) and shear (G) moduli:

$$K(z) = K_m + \frac{V_c}{\dfrac{1}{K_c - K_m} + \dfrac{V_m}{K_m + \dfrac{4G_m}{3}}} \tag{2.5a}$$

$$G(z) = G_m + \frac{V_c}{\dfrac{1}{G_c - G_m} + \dfrac{V_m}{G_m + f_m}} \tag{2.5b}$$

where:

$$f_m = \frac{G_m(9K_m + 8G_m)}{6(K_m + 2G_m)} \tag{2.6}$$

Then, the Young's modulus and the Poisson's ratio are given by:

$$E(z) = \frac{9K(z)G(z)}{3K(z) + G(z)} \tag{2.7a}$$

$$\nu(z) = \frac{3K(z) - 2G(z)}{2(3K(z) + G(z))} \tag{2.7b}$$

The upper bound can be readily achieved by interchanging the matrix and inclusion regimes in the formulation.

Alternatively, the Mori-Tanaka model can also be used to evaluate the effective properties [50, 48]. Given a dilute distribution of inclusions, it assumes that, at a sufficient distance between them, the strain or stress fields caused by the external load prevail, disregarding possible interactions between inclusions. In the special case where an isotropic matrix is reinforced by isotropic spherical particles, the effective properties approximation is equal to the Hashin-Shtrikman lower bound[47].

Regarding the Self-Consistent Method (SCM), while it was primarily developed to address single-phase polycrystalline problems, it presents beneficial features to FGM applications.

The method does not discriminate between the two phases, making no assumptions about which constituent is each phase [15, 14]. It accounts for the interaction between inclusions, which is crucial in modeling the effective medium. The SCM employs a semi-explicit formulation where the effective properties are not directly determined from the volume fraction and physical properties of the constituents, but through an iterative scheme:

$$V_c(z) = \frac{\frac{K_m}{K_m+\frac{4}{3}G(z)} + \frac{5G_c}{G(z)-G_c} + 2}{\frac{K_m}{K_m+\frac{4}{3}G(z)} + \frac{5G_c}{G(z)-G_c} - \frac{K_c}{K_c+\frac{4}{3}G(z)} - \frac{5G_m}{G(z)-G_m}} \tag{2.8a}$$

$$K(z) = \frac{1}{\frac{V_c(z)}{K_c+\frac{4}{3}G(z)} + \frac{1-V_c(z)}{K_m+\frac{4}{3}G(z)}} - \frac{4}{3}G(z) \tag{2.8b}$$

The Young's modulus and the Poisson's ratio are then given using Eq. (2.7a) and (2.7b). It is worth remarking that this model provides a reliable estimation for the effective properties, with results falling within the Hashin-Shtrikman bounds. Despite being a complex method, the SCM can be valuable when information about the FGM is limited[51, 52]. Alternatively, the Generalized Self-Consistent Method (GSCM) is an extension of the SCM that covers a broader range of microstructural variations and is more commonly employed in recent studies[53, 54].

Fig. 4 presents a comparison of the Young's modulus homogenization results obtained using micromechanical models against experimental data. Although the Voigt model exhibits a poor agreement, it remains the most widely used homogenization method in the literature. On the other hand, despite its simple approach to the evaluation of effective properties, the Mori-Tanaka technique demonstrates a remarkable agreement with experimental data for Al/SiC composites, boasting a coefficient of determination $R^2 = 96.9\%$[13]. The Generalized Self-Consistent Method also yields very close results, with a slight accuracy gain over Mori-Tanaka for this specific dataset, but it involves a significantly more complex implementation. Thus, this work exclusively uses the Voigt and Mori-Tanaka models.

Fig. 5 illustrates the effective elastic modulus of an Al/Al_2O_3 FG plate for various power indices N, being assessed by both micromechanical models. It is evident that the Voigt model consistently returns a higher effective property across the entire gradation when the resulting material is non-homogeneous, implying in a overall stiffer structure.

2.3 Tamura-Tomota-Ozawa model

Structural failure can be attributed to instability or material failure, and in practical scenarios these factors often occur simultaneously. It happens due to an inelastic material

response leading to a destabilizing structural effect, or the reverse, where an overload results in inelastic deformation. Since this work focuses on FGM as particulate metal matrix composites (MMC), material failure is primarily determined by the behavior of the ductile phase, thus necessitating the employment of an elastoplastic analysis to thoroughly determine the structural response[32].

Figure 4 – Comparison among homogenization schemes and experimental results for Al/SiC MMC.
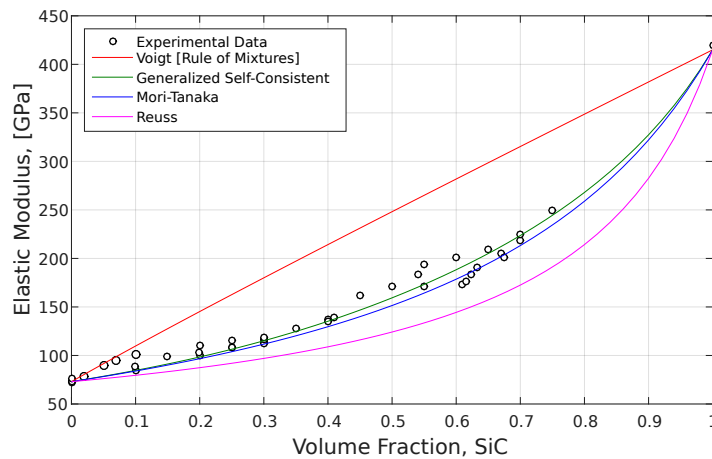
Source: Medeiros Jr., Parente Jr. and Melo[47].

Figure 5 – Effective elastic modulus of an Al/Al_2O_3 FG plate by Voigt and Mori-Tanaka models.
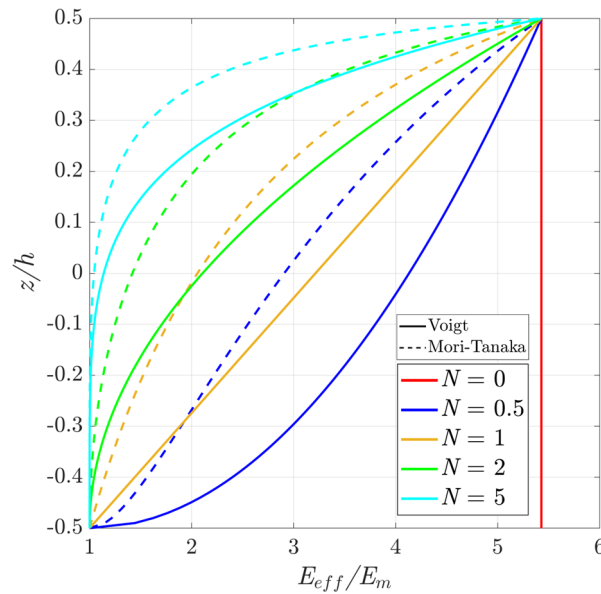
Source: The author.

To accurately capture the overall mechanical performance of FGM, more sophisticated failure criteria are required. This is because the mechanical behavior depends on the properties of the composites' individual phases. The homogenization methods previously discussed can be solely used to determine effective elastic properties. In order to obtain variables related to the plastic regime, an additional model capable of approximating both the yield stress and the hardening law is necessary[13, 55, 28].

While the Tsai-Hill criteria are commonly used in the literature for laminated, anisotropic, composites, they may not be suitable for FGM structures. FGMs are often isotropic, despite non-homogeneous, and present a continuous gradation between their phases. Consequently, alternative models are typically employed for material failure analysis in FGMs.

The Tamura-Tomota-Ozawa (TTO) model is widely used to simulate the performance of MMCs[56, 57]. This model assumes that the failure is governed by the ductile constituent, resulting in the matrix displaying an elastoplastic behavior while the inclusions remain elastic.

Furthermore, the TTO model defines the composite uniaxial stress and strain as the corresponding average uniaxial stresses and strains of both constituents. Therefore, an additional parameter, the stress-to-strain ratio (q), is introduced:

$$q = \frac{\sigma_1 - \sigma_2}{\varepsilon_1 - \varepsilon_2}, \qquad 0 < q < \infty \tag{2.9}$$

where σ_i and ε_i are the average stresses and strains of each constituent. This parameter is used to improve the approximation of the composite behavior to an available set of experimental data.

The effective yield stress is evaluated by:

$$\sigma_{y,\text{eff}} = \sigma_{y,m} \left[V_m + \left(\frac{q + E_m}{q + E_c} \right) \frac{E_c}{E_m} (1 - V_m) \right] \tag{2.10}$$

where $\sigma_{y,m}$ is the yield strength of the metallic phase, E_m and E_c are the Young's moduli for metal and ceramic constituents respectively. Additionally, the FGM material nonlinearity is considered by assuming the hardening law to be linear with the hardening modulus depending on the volume fraction. This definition is confusing within the literature, since most studies define the elastoplastic tangent modulus with the variable H[58, 13], which is commonly used to define the hardening modulus[59]. These moduli, despite presenting close values, carry distinct physical meaning. Therefore, for the sake of clarity, in this work the plastic modulus is defined as:

$$E_p = \frac{V_m E_{p,m} \xi + (1 - V_m) E_c}{V_m \xi + (1 - V_m)} \tag{2.11}$$

where E_p is the effective elastoplastic tangent modulus, $E_{p,m}$ is the metal elastoplastic tangent modulus, and $\xi = (q+E_c)/(q+E_{p,m})$. Then, the effective hardening modulus H can be evaluated using the uniaxial formula[60]:

$$H = \frac{E\,E_p}{E - E_p} \tag{2.12}$$

Fig. 6 illustrates the variation in yield strength of an FG structure comprised of metal matrix and ceramic inclusions. It can be seen that the ceramic represents a brittle phase and the metal represents a ductile phase, whilst the composite presents an intermediate behavior depending on the volume fraction. It also shows the bilinear failure response governed by ductile phase, highlighting the influence of the parameter q on the yield strength.

Figure 6 – Schematic stress-strain curve for FGM.
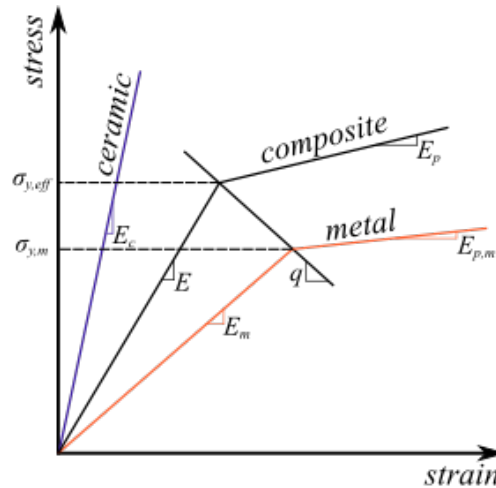
Source: Adapted from Nayak, Bhowmick and Saha[61].

In order to define the plastic regime, the von Mises yielding criterion is employed. The material behaves elastically until it reaches the yield stress, after which it undergoes plastic deformation. The yield criterion can be defined as:

$$f = \sqrt{3J_2} - \sigma_y(\overline{\varepsilon}^p) = \sqrt{\frac{3}{2}s_{ij}s_{ij}} - \sigma_y(\overline{\varepsilon}^p) \leq 0 \tag{2.13}$$

where f is the yield surface, and s_{ij} is the deviatoric stress tensor given by:

$$s_{ij} = \sigma_{ij} - \frac{1}{3}\delta_{ij}\sigma_{kk} \tag{2.14}$$

and $\sigma_y(\overline{\varepsilon}^p)$ is the uniaxial yield stress expressed in terms of the accumulated plastic strain.

This work employs an associative flow rule, where the direction of the plastic flow depends solely on the current stress state and yield surface. Consequently, the plastic strain rate can be mathematically described as:

$$\dot{\varepsilon}_{ij}^{p} = \dot{\gamma}\frac{\partial f}{\partial \sigma_{ij}} \tag{2.15}$$

where $\dot{\gamma} \geq 0$ is the plastic multiplier. Since plastic deformation is irreversible, the accumulated equivalent plastic strain $\bar{\varepsilon}^{p}$ serves as an internal state variable to monitor the loading history:

$$\bar{\varepsilon}^{p} = \int \sqrt{\frac{2}{3}\dot{\varepsilon}_{ij}^{p}\dot{\varepsilon}_{ij}^{p}}\,dt \tag{2.16}$$

Additionally, the material stiffens as plastic deformation occurs. The strain hardening is isotropic and, as previously stated, linear, resulting in:

$$\sigma_y\left(\bar{\varepsilon}^{p}\right) = \sigma_{y0} + H\,\bar{\varepsilon}^{p} \tag{2.17}$$

where H is the composite effective hardening and σ_{y0} is the effective initial yield stress. A more detailed discussion about the elastoplastic behavior, including the computational aspects, is presented in Section 3.5.

3   ANALYSIS OF FG SOLIDS

In the process of conducting a structural analysis, the primary objective is to accurately predict the mechanical behavior and performance of a body when subjected to external loads. This typically includes determining displacements, strains and stresses within the structure. Indeed, there are multiple categories of analysis, including buckling, post-buckling and vibration, among others.

Still within the realm of structural analysis, static and stability are significant areas of application. In these scenarios, experimental data suggests that both geometric and material nonlinearities are present during structural failure. Therefore, in this work, both types of nonlinearities are considered to provide a more consistent approximation of structural behavior.

A general Finite Element formulation is primarily presented, since it is the most commonly adopted computational method. Then, an Isogeometric Analysis approach is further discussed. Both formulations presented in this chapter have been implemented in an in-house software developed in C++ called *Finite Element Analysis Tool* (FAST), following the references defined in each section. The implementations are validated later in this work by comparing numerical results against evaluations found in the existing literature.

3.1   Displacements and Strains

In order to provide a general computational approach for analysis of FG solids, a Finite Element Method formulation is presented. The displacements (u, v, w) within the element can be expressed in terms of the nodal displacements (u_i, v_i, w_i):

$$u = \sum_{i=1}^{n} N_i u_i, \quad v = \sum_{i=1}^{n} N_i v_i, \quad w = \sum_{i=1}^{n} N_i w_i \tag{3.1}$$

where N_i are the basis functions and n is the number of nodes. Alternatively, the matrix formulation is defined as:

$$\hat{\mathbf{u}} = \begin{bmatrix} u \\ v \\ w \end{bmatrix} = \sum_{i=1}^{n} \begin{bmatrix} N_i & 0 & 0 \\ 0 & N_i & 0 \\ 0 & 0 & N_i \end{bmatrix} \begin{bmatrix} u_i \\ v_i \\ w_i \end{bmatrix} = \sum_{i=1}^{n} \mathbf{N}_i \mathbf{u}_i = \mathbf{N}\mathbf{u} \tag{3.2}$$

Furthermore, employing an isoparametric approach, the element geometry is described by the same basis functions used to interpolate the displacements:

$$x = \sum_{i=1}^{n} N_i x_i, \quad y = \sum_{i=1}^{n} N_i y_i, \quad z = \sum_{i=1}^{n} N_i z_i \tag{3.3}$$

where x_i, y_i and z_i are the global coordinates.

Additionally, finite elements can be employed to simplify the representation of FGM composites, allowing the volume fraction of each node to be approximated by the basis functions, similarly to the interpolation of displacements[62, 63]. Consequently, the volume fraction profile within the element is expressed as:

$$V_c = \sum_{i=1}^{n} N_i V_{c,i} \tag{3.4}$$

The effective properties can then be evaluated by any of the aforementioned micromechanical models discussed in Chapter 2.

Since strains require derivatives in 3D Cartesian space and the displacements are described in parametric coordinates, these derivatives have to be transformed by employing the chain rule. The matrix formulation for derivatives is given as follows:

$$\begin{bmatrix} N_{i,r} \\ N_{i,s} \\ N_{i,t} \end{bmatrix} = \mathbf{J} \begin{bmatrix} N_{i,x} \\ N_{i,y} \\ N_{i,z} \end{bmatrix} \tag{3.5}$$

where $\mathbf{J}$ is the Jacobian matrix, which is evaluated by:

$$\mathbf{J} = \begin{bmatrix} \sum_{i=1}^{n} N_{i,r} x_i & \sum_{i=1}^{n} N_{i,r} y_i & \sum_{i=1}^{n} N_{i,r} z_i \\ \sum_{i=1}^{n} N_{i,s} x_i & \sum_{i=1}^{n} N_{i,s} y_i & \sum_{i=1}^{n} N_{i,s} z_i \\ \sum_{i=1}^{n} N_{i,t} x_i & \sum_{i=1}^{n} N_{i,t} y_i & \sum_{i=1}^{n} N_{i,t} z_i \end{bmatrix} \tag{3.6}$$

Finally, in order to obtain the derivatives in the cartesian space:

$$\begin{bmatrix} N_{i,x} \\ N_{i,y} \\ N_{i,z} \end{bmatrix} = \mathbf{J}^{-1} \begin{bmatrix} N_{i,r} \\ N_{i,s} \\ N_{i,t} \end{bmatrix} \tag{3.7}$$

In this work, the total Lagrangian formulation for continuum (i.e. solid) elements is used. The formulation considers large displacements but assumes small strains. Thus, Green-Lagrange strains and Piola-Kirchhoff II stresses are adopted in further mathematical developments. Both parameters are computed with respect to the undeformed structural configuration.

The Green-Lagrange strains are comprised of both linear and nonlinear contributions. Given a displacement field, they can be defined in a matrix formulation as follows[64]:

$$\varepsilon = \begin{bmatrix} \varepsilon_x \\ \varepsilon_y \\ \varepsilon_z \\ \gamma_{xy} \\ \gamma_{xz} \\ \gamma_{yz} \end{bmatrix} = \underbrace{\begin{bmatrix} u_{,x} \\ v_{,y} \\ w_{,z} \\ u_{,y}+v_{,x} \\ u_{,z}+w_{,x} \\ u_{,z}+w_{,y} \end{bmatrix}}_{\varepsilon_l} + \underbrace{\begin{bmatrix} \frac{1}{2}(u_{,x}^2 + v_{,x}^2 + w_{,x}^2) \\ \frac{1}{2}(u_{,y}^2 + v_{,y}^2 + w_{,y}^2) \\ \frac{1}{2}(u_{,z}^2 + v_{,z}^2 + w_{,z}^2) \\ u_{,x}u_{,y}+v_{,x}v_{,y}+w_{,x}w_{,y} \\ u_{,x}u_{,z}+v_{,x}v_{,z}+w_{,x}w_{,z} \\ u_{,y}u_{,z}+v_{,y}v_{,z}+w_{,y}w_{,z} \end{bmatrix}}_{\varepsilon_{nl}}$$ (3.8)

The required derivatives for the aforementioned 3D formulation can be evaluated as:

$$\begin{aligned} u_{,x} &= \sum_{i=1}^{n} N_{i,x}u_i, \quad u_{,y} = \sum_{i=1}^{n} N_{i,y}u_i, \quad u_{,z} = \sum_{i=1}^{n} N_{i,z}u_i, \\ v_{,x} &= \sum_{i=1}^{n} N_{i,x}v_i, \quad v_{,y} = \sum_{i=1}^{n} N_{i,y}v_i a, \quad v_{,z} = \sum_{i=1}^{n} N_{i,z}v_i, \\ w_{,x} &= \sum_{i=1}^{n} N_{i,x}w_i, \quad w_{,y} = \sum_{i=1}^{n} N_{i,y}w_i, \quad w_{,z} = \sum_{i=1}^{n} N_{i,z}w_i \end{aligned}$$ (3.9)

Thus, the vector β becomes:

$$\beta = \begin{bmatrix} u_{,x} \\ u_{,y} \\ u_{,z} \\ v_{,x} \\ v_{,y} \\ v_{,z} \\ w_{,x} \\ w_{,y} \\ w_{,z} \end{bmatrix} = \sum_{i=1}^{n} \begin{bmatrix} N_{i,x} & 0 & 0 \\ N_{i,y} & 0 & 0 \\ N_{i,z} & 0 & 0 \\ 0 & N_{i,x} & 0 \\ 0 & N_{i,y} & 0 \\ 0 & N_{i,z} & 0 \\ 0 & 0 & N_{i,x} \\ 0 & 0 & N_{i,y} \\ 0 & 0 & N_{i,z} \end{bmatrix} \begin{bmatrix} u_i \\ v_i \\ w_i \end{bmatrix} = \mathbf{G}\mathbf{u}$$ (3.10)

By organizing the displacement derivatives from the vector $\beta = [u_{,x}, u_{,y}, ..., w_{,z}]^T$, the strain matrix formulation can be written as:

$$\varepsilon = \varepsilon_l + \varepsilon_{nl} = \mathbf{H}\beta + \frac{1}{2}\mathbf{A}\beta$$ (3.11)

where:

$$
\mathbf{H} = \begin{bmatrix}
1 & 0 & 0 & 0 & 0 & 0 & 0 & 0 & 0 \\
0 & 0 & 0 & 0 & 1 & 0 & 0 & 0 & 0 \\
0 & 0 & 0 & 0 & 0 & 0 & 0 & 0 & 1 \\
0 & 1 & 0 & 1 & 0 & 0 & 0 & 0 & 0 \\
0 & 0 & 1 & 0 & 0 & 1 & 1 & 0 & 0 \\
0 & 0 & 0 & 0 & 0 & 0 & 0 & 1 & 0
\end{bmatrix} ; \quad
\mathbf{A} = \begin{bmatrix}
u_{,x} & 0 & 0 & v_{,x} & 0 & 0 & w_{,x} & 0 & 0 \\
0 & u_{,y} & 0 & 0 & v_{,y} & 0 & 0 & w_{,y} & 0 \\
0 & 0 & u_{,z} & 0 & 0 & v_{,z} & 0 & 0 & w_{,z} \\
u_{,y} & u_{,x} & 0 & v_{,y} & v_{,x} & 0 & w_{,y} & w_{,x} & 0 \\
u_{,z} & 0 & u_{,x} & v_{,z} & 0 & v_{,x} & w_{,z} & 0 & w_{,x} \\
0 & u_{,z} & u_{,y} & 0 & v_{,z} & v_{,y} & 0 & w_{,z} & w_{,y}
\end{bmatrix}
$$

$$(3.12)$$

By substituting $\beta = \mathbf{Gu}$ in Eq. (3.11):

$$
\varepsilon = \mathbf{HGu} + \frac{1}{2}\mathbf{AGu} \tag{3.13}
$$

Therefore, the matrix which describes the strain-displacement relations is defined by:

$$
\varepsilon = \mathbf{Bu}, \quad \mathbf{B} = \mathbf{B}_0 + \frac{1}{2}\mathbf{B}_L \tag{3.14}
$$

where $\mathbf{B}_0$ and $\mathbf{B}_L$ are the linear and nonlinear contributions, respectively defined as:

$$
\mathbf{B}_0 = \mathbf{HG}; \quad \mathbf{B}_L = \mathbf{AG} \tag{3.15}
$$

3.2 Equilibrium Equations

Using the Principle of Virtual Work, the equilibrium for any given solid is achieved when the internal virtual work (δU) equals the external virtual work (δW_{ext}), assuming that the displacement field obeys the essential boundary conditions of the problem. Mathematically, this is described as:

$$
\delta U = \delta W_{ext} \implies \int_V \delta\varepsilon^T \sigma \, dV = \int_V \delta\hat{\mathbf{u}}^T \mathbf{b} \, dV + \int_S \delta\hat{\mathbf{u}}^T \mathbf{q} \, dS + \sum_{j=1}^{nj} \hat{\mathbf{u}}_j^T \mathbf{F}_j \tag{3.16}
$$

where $\delta\varepsilon$ is the virtual strain vector, σ is the stress vector, $\mathbf{b}$ denoted the body forces, $\mathbf{q}$ stands for the surface forces and $\mathbf{F}_j$ are the concentrated forces applied to the body. In order to simplify this formulation, the internal virtual work can be expressed in terms of the internal force vector ($\mathbf{g}$):

$$
\delta U = \delta\mathbf{u}^T \mathbf{g} = \int_V \delta\varepsilon^T \sigma \tag{3.17}
$$

Since the Green-Lagrange strains are being adopted, it can be shown that:

$$\delta\varepsilon = \overline{\mathbf{B}}\delta\mathbf{u} \tag{3.18}$$

with:

$$\overline{\mathbf{B}} = \mathbf{B}_0 + \mathbf{B}_L \tag{3.19}$$

what implies in:

$$\mathbf{g} = \int_V \overline{\mathbf{B}}^T \sigma \, dV \tag{3.20}$$

On the other hand, the external virtual work can be described as:

$$\delta W_{ext} = \delta\mathbf{u}^T \int_V \mathbf{N}^T \mathbf{b} \, dV + \delta\mathbf{u}^T \int_S \mathbf{N}^T \mathbf{q} \, dS + \delta\mathbf{u}^T \sum_{j=1}^{nj} \mathbf{N}_j^T \mathbf{F}_j = \delta\mathbf{u}^T \mathbf{f} \tag{3.21}$$

where the external load vector ($\mathbf{f}$) is given by:

$$\mathbf{f} = \int_V \mathbf{N}^T \mathbf{b} \, dV + \int_S \mathbf{N}^T \mathbf{q} \, dS + \sum_{j=1}^{nj} \mathbf{N}_j^T \mathbf{F}_j \tag{3.22}$$

Therefore, the equilibrium equations can be written as:

$$\mathbf{g} = \mathbf{f} \tag{3.23}$$

It is important to highlight two things. First, this equation is valid for all geometric and material nonlinear problems. Second, the volume and surface parameters used in the integrals are evaluated for the undeformed geometry, due to the use of the Total Lagrangian approach as previously mentioned.

3.3 Tangent Stiffness Matrix

As will be further discussed, the tangent stiffness matrix is an important part of the nonlinear analysis. It is computed by differentiating the internal forces vector with respect to the displacement vector:

$$\mathbf{K}_T = \frac{\partial\mathbf{g}}{\partial\mathbf{u}} = \underbrace{\int_V \overline{\mathbf{B}}^T \frac{\partial\sigma}{\partial\mathbf{u}} \, dV}_{\mathbf{K}_E} + \underbrace{\int_V \frac{\partial\overline{\mathbf{B}}^T}{\partial\mathbf{u}} \sigma \, dV}_{\mathbf{K}_G} = \mathbf{K}_E + \mathbf{K}_G \tag{3.24}$$

where $\mathbf{K}_E$ and $\mathbf{K}_G$ represent the material and geometric stiffness matrices. While the evaluation of $\partial\mathbf{B}^T/\partial\mathbf{u}$ might seem straightforward, the partial derivative $\partial\sigma/\partial\mathbf{u}$ is determined by:

$$\frac{\partial\sigma}{\partial\mathbf{u}} = \frac{\partial\sigma}{\partial\varepsilon}\frac{\partial\varepsilon}{\partial\mathbf{u}} = \mathbf{C}_T\overline{\mathbf{B}} \tag{3.25}$$

where $\mathbf{C}_T$ is called tangent constitutive matrix. and it relies on the material behavior and the specific constitutive model used in the analysis[60, 59]. In this work, by employing an elastoplastic analysis process, the evaluation of $\mathbf{C}_T$ matrix is discussed in details throughout the next section. Furthermore, the material stiffness matrix contribution is defined as:

$$\mathbf{K}_E = \int_V \overline{\mathbf{B}}^T \mathbf{C}_T \overline{\mathbf{B}} \, dV \tag{3.26}$$

Additionally, the contribution from the geometric stiffness matrix is evaluated by[65]:

$$\mathbf{K}_G = \int_V \mathbf{G}^T \mathbf{S} \mathbf{G} \, dV \tag{3.27}$$

where:

$$\mathbf{S} = \begin{bmatrix} \overline{\mathbf{S}} & 0 & 0 \\ 0 & \overline{\mathbf{S}} & 0 \\ 0 & 0 & \overline{\mathbf{S}} \end{bmatrix}, \qquad \overline{\mathbf{S}} = \begin{bmatrix} \sigma_{xx} & \sigma_{xy} & \sigma_{xz} \\ \sigma_{xy} & \sigma_{yy} & \sigma_{yz} \\ \sigma_{xz} & \sigma_{yz} & \sigma_{zz} \end{bmatrix} \tag{3.28}$$

It is worth emphasizing that, seeking for a more computationally efficient implementation, the integration process is performed by the Gaussian integration technique for each integration point along the three parametric directions. The number of points depends on the shape functions and the gradation profile. The assembly of the finite elements' contributions to the global stiffness matrix is accomplished through the use of the Direct Stiffness Method.

3.4   Nonlinear Analysis

In the context of static analysis of nonlinear structures subjected to displacement-independent loads, the equilibrium equations can be written as:

$$\mathbf{r}(\mathbf{u}, \lambda) = \mathbf{g}(\mathbf{u}) - \lambda \mathbf{q} = 0, \qquad \mathbf{f} = \lambda \mathbf{q} \tag{3.29}$$

where $\mathbf{r}$ is the residual, $\mathbf{q}$ is a reference load vector and λ is referred to as the load factor, a parameter that governs the rate of load increment.

In order to obtain an appropriate solution for the nonlinear equilibrium equations, numerical methods are employed. The Newton-Raphson is the most used approach within the literature for solving such problems. This method is based on the linearization of the residual:

$$\mathbf{r}_n = \mathbf{r} + \mathbf{K}_T \delta \mathbf{u} + \frac{\partial \mathbf{r}}{\partial \lambda} \quad \Rightarrow \quad \mathbf{K}_T = \frac{\partial \mathbf{r}}{\partial \mathbf{u}} = \frac{\partial \mathbf{g}}{\partial \mathbf{u}} \tag{3.30}$$

where the subscript n is denotes the new residual, $\mathbf{K}_T$ is the tangent stiffness matrix and $\partial \mathbf{r}/\partial \lambda$ is the internal load vector $\mathbf{g}$.

Furthermore, considering that $\mathbf{r}_n = 0$, Eq. (3.30) can be rewritten as:

$$\mathbf{K}_T \delta \mathbf{u} - \delta \lambda \mathbf{q} = -\mathbf{r} \qquad (3.31)$$

However, as there are n equations and $n+1$ variables, where n is the number of structural DoFs, this system of equations is under-determined.

Therefore, the Load Control Method is briefly described here for a clearer understanding of the solution procedure. In this method, a load factor (λ) is assigned for each step. Since it remains constant throughout each iteration, $\delta \lambda$ is zero. Therefore, Eq. (3.31) can be rewritten as:

$$\mathbf{K}_T \delta \mathbf{u} = -\mathbf{r} \qquad (3.32)$$

After the evaluating the displacement increment, the new nodal displacements are updated as:

$$\mathbf{u}_{n+1} = \mathbf{u}_n + \delta \mathbf{u} \qquad (3.33)$$

Subsequently, these displacements are used to compute both new internal force vector and residual. This iterative process continues until the equilibrium equation is satisfied, which means the residual is smaller than an adopted numerical tolerance:

$$\frac{\|\mathbf{r}\|}{max(1, \|\mathbf{f}\|)} \leq TOL \qquad (3.34)$$

This methodology is commonly employed within the literature due to presenting a quadratic rate of convergence, resulting in a reduced computational cost.

This method is widely used to trace the nonlinear equilibrium paths of stable structures[66]. However, the consideration of nonlinearities may result in the appearance of limit points along the equilibrium path. In these cases, it is necessary to use more complex path-following algorithms, such as the displacement control and arc-length methods[67, 68, 69].

3.4.1 Linear stability

Furthermore, for stability problems where prebuckling displacements are negligible, a linear analysis process can be employed. It is postulated that the instability occurs when the

tangential matrix is equal to the material stiffness matrix, whereas the geometric stiffness matrix depends on a load factor λ:

$$\mathbf{K}_E = \mathbf{K}_0, \quad \mathbf{K}_G = \lambda \overline{\mathbf{K}}_G \tag{3.35}$$

By defining the tangent stiffness matrix to be singular at the bifurcation point, the classical eigenvalue buckling solution is achieved[70] :

$$(\mathbf{K}_0 + \lambda \overline{\mathbf{K}}_G)\boldsymbol{\phi} = 0 \tag{3.36}$$

However, although providing an accurate approximation for the critical buckling load, this methodology is incapable of modeling the postbuckling behavior. Given that both nonlinearities are considered in this work, it is crucial be able to study the structural equilibrium path. Therefore, the aforementioned numerical path-following methods can be employed to accurately determine the structure's load-displacement curve.

3.5 Elastoplasticity

Prior to yield, the stresses can be evaluated by the Hooke's Law:

$$\sigma = \mathbf{C}\varepsilon \tag{3.37}$$

where $\mathbf{C}$ is the elastic constitutive matrix given by:

$$\mathbf{C} = \frac{E}{(1+v)(1-2v)} \begin{bmatrix} (1-v) & v & v & 0 & 0 & 0 \\ v & (1-v) & v & 0 & 0 & 0 \\ v & v & (1-v) & 0 & 0 & 0 \\ 0 & 0 & 0 & \frac{(1-2v)}{2} & 0 & 0 \\ 0 & 0 & 0 & 0 & \frac{(1-2v)}{2} & 0 \\ 0 & 0 & 0 & 0 & 0 & \frac{(1-2v)}{2} \end{bmatrix} \tag{3.38}$$

When dealing with FG structures, it is important to remark that the adopted values for the elastic modulus (E) and Poisson's ratio (v) are the composite effective properties evaluated by the proposed micromechanical model. Due to the use of numerical integration, Eqs. (3.37) and (3.38), as well as the composite properties, are only evaluated at the Gauss points.

Regarding the framework of the small strain theory of plasticity presented in Neto, Peric and Owen[59], total strain can be decomposed into the sum of an elastic, by definition

reversible, and a plastic, by definition permanent, components:

$$\varepsilon = \varepsilon^e + \varepsilon^p \quad \Longrightarrow \quad \varepsilon^e = \varepsilon - \varepsilon^p \tag{3.39}$$

Given that the elastic domain is delimited by a yield surface f, according to the plasticity theory, any admissible stress state must lie either inside or on the boundary of the yield surface. Furthermore, a standard associative flow rule defines that the plastic strain rate can be given as:

$$\dot{\varepsilon}^p = \dot{\gamma} \mathbf{N} \tag{3.40}$$

where $\mathbf{N}$ is the Prandtl-Reuss flow vector:

$$\mathbf{N} \equiv \partial f / \partial \sigma \tag{3.41}$$

and $\dot{\gamma}$ is the non-negative plastic multiplier. For stress levels within the yield surface, only elastic straining may occur, while for stress states at the yield surface, either elastic unloading or plastic yielding may happen. This yield criterion is expressed as:

$$\text{If } f(\sigma, \sigma_y) < 0 \Longrightarrow \dot{\varepsilon}^p = 0$$

$$\text{If } f(\sigma, \sigma_y) = 0 \Longrightarrow \begin{cases} \dot{\varepsilon}^p = 0 \text{ for elastic unloading} \\ \dot{\varepsilon}^p \neq 0 \text{ for plastic loading} \end{cases} \tag{3.42}$$

Assuming that the plastic multiplier also must satisfy the complementary condition:

$$f \dot{\gamma} = 0 \tag{3.43}$$

The methodology defined by Eq. (3.42) can be better developed by defining the constraints related to each case. For instance, the plastic strain rate vanishes within elastic domain:

$$f < 0 \quad \Longrightarrow \quad \dot{\gamma} = 0 \quad \Longrightarrow \quad \dot{\varepsilon}^p = 0 \tag{3.44}$$

On the other hand, the plastic flow may only occur when the stress level coincides with the boundary of the yield surface:

$$f = 0 \quad \Longrightarrow \quad \dot{\gamma} \geq 0 \tag{3.45}$$

The specifics yield condition, flow rule and accumulated equivalent plastic strain used in this work have been presented in Section 2.3, where the Tamura-Tomota-Ozawa model was discussed. It is important to once again remark that the plastic regime is based on the von Mises yield criterion, using the second invariant of the deviatoric stress tensor (J_2) approach.

3.5.1 Returning Mapping

The return mapping is a computational technique used to update the stress state and strain variables for materials experiencing plastic deformation. It employs an iterative procedure to ensure that the stress state remains within the yield surface as required by the plasticity theory[59, 60]. To accomplish this, the return mapping algorithm is divided into two parts: the elastic predictor and the return mapping process, which will be better described below.

Assuming that a strain increment is provided:

$$\Delta\varepsilon = \varepsilon_{n+1} - \varepsilon_n \tag{3.46}$$

The first step is the elastic predictor process. During this step, the strain increment is treated as fully elastic, whilst the accumulated plastic strain remains constant. Thus, the elastic trial strain and trial plastic strain are defined as:

$$
\begin{aligned}
\varepsilon_{n+1}^{e\,trial} &= \varepsilon_n^e + \Delta\varepsilon \\
\overline{\varepsilon}_{n+1}^{p\,trial} &= \overline{\varepsilon}_n^p
\end{aligned}
\tag{3.47}
$$

Thereafter, the corresponding elastic trial stress is calculated using Eq. (3.38). Subsequently, it is determined whether the trial stresses σ_{n+1}^{trial} lies within the trial yield surface: $f^{trial} = f(\sigma^{trial})$. Depending on the outcome, two different situations are possible:

– if $f^{trial} \leq 0$ the process is, indeed, purely elastic and the elastic trial state is the solution to the problem. The states variables are, then, set as:

$$
\begin{aligned}
\varepsilon_{n+1}^e &= \varepsilon_{n+1}^{e\,trial} \\
\sigma_{n+1} &= \sigma_{n+1}^{trial} \\
\overline{\varepsilon}_{n+1}^p &= \overline{\varepsilon}_{n+1}^{p\,trial} = \overline{\varepsilon}^p \\
\sigma_{y_{n+1}} &= \sigma_{y_{n+1}}^{trial} = \sigma_{y_n}
\end{aligned}
\tag{3.48}
$$

– otherwise σ_{n+1}^{trial} is out of elastic domain and the process is elastoplastic. Therefore, the return-mapping technique has to be employed in order to evaluate the proper solution.

In this work, linear isotropic hardening plasticity is considered. Hence, by using Eq. (2.17), the yield criterion reads as:

$$
\begin{aligned}
f(\Delta\gamma) &\equiv q_{n+1}^{trial} - 3G\Delta\gamma - \sigma_y(\overline{\varepsilon}^p + \Delta\gamma) = 0 \quad \Rightarrow \\
f(\Delta\gamma)^{trial} &= q_{n+1}^{trial} - 3G\Delta\gamma - [\sigma_0 + (\overline{\varepsilon}_n^p + \Delta\gamma)H] = 0
\end{aligned}
\tag{3.49}
$$

where:

$$q_{n+1}^{trial} = \sqrt{\frac{3}{2} s_{n+1}^{trial} : s_{n+1}^{trial}} \tag{3.50}$$

Then, the incremental plastic multiplier solution is obtained using a closed-form equation:

$$\Delta\gamma = \frac{f^{trial}}{3G + H} \tag{3.51}$$

As only deviatoric stresses are corrected and projected onto the plastic surface, the trial hydrostatic (p) and deviatoric (s) stresses must be evaluated. Finally, the updated state variables are defined by[59]:

$$
\begin{aligned}
p_{n+1} &= p_{n+1}^{trial} \\
s_{n+1} &= \left(1 - \frac{\Delta\gamma 3G}{q_{n+1}^{trial}}\right) s_{n+1}^{trial} \\
\sigma_{n+1} &= s_{n+1} + p_{n+1}\mathbf{I} \\
\varepsilon_{n+1}^e &= \frac{1}{2G} s_{n+1} + \frac{1}{3}\varepsilon_{v_{n+1}}^{e\,trial}\mathbf{I} \\
\bar{\varepsilon}_{n+1}^p &= \bar{\varepsilon}_n^p + \Delta\gamma
\end{aligned}
\tag{3.52}
$$

The entire state update procedure described above is summarized in Algorithm 1. This box provides a step-by-step overview of the state update procedure for plasticity in the material. It encompasses elastic prediction, plastic admissibility checks and return mapping, detailing how the state variables are updated at each step. Additionally, in Fig. 7, the plastic corrector algorithm is illustrated. The adopted algorithm is based on the closest point projection since an associative flow rule is employed. It can be used for both perfectly plastic and linearly hardening materials[71]. The circular shape of the yield surface is due to the von Mises model. By considering the hardening, the radius of the yield surface increases whenever there is plastic deformation, whereas in the case of perfect plasticity, the updated surface at t_{n+1} remains the same as at t_n.

3.5.2 Tangent constitutive matrix

With σ_{n+1} expressed in terms of both the elastic trial strain and the internal variable evaluated at time t_n, it is possible to define the consistent tangent operator:

$$\mathbf{C} = \frac{\partial\sigma}{\partial\varepsilon_{n+1}} \tag{3.53}$$

Algoritmo 1: Update State Procedure

I) Elastic predictor: Given $\Delta\varepsilon$ and state variables, the elastic trial state is evaluated

$$\varepsilon_{n+1}^{e\,trial} = \varepsilon_n^e + \Delta\varepsilon, \qquad \overline{\varepsilon}_{n+1}^{p\,trial} = \overline{\varepsilon}_n^p$$

II) Plastic admissibility: If $f(\Delta\gamma)^{trial} \leq 0$, update state variables:

$$\varepsilon_{n+1}^e = \varepsilon_{n+1}^{e\,trial}, \quad \sigma_{n+1} = \sigma_{n+1}^{trial}, \quad \overline{\varepsilon}_{n+1}^p = \overline{\varepsilon}_{n+1}^{p\,trial} = \overline{\varepsilon}^p, \quad \sigma_{y_{n+1}} = \sigma_{y_{n+1}}^{trial} = \sigma_{y_n}$$

Then exit the procedure.

III) Return mapping: Plastic correction and update state variables:

$$\Delta\gamma = \frac{f^{trial}}{3G + H}$$

$$p_{n+1} = p_{n+1}^{trial}, \qquad s_{n+1} = \left(1 - \frac{\Delta\gamma 3G}{q_{n+1}^{trial}}\right) s_{n+1}^{trial}$$

$$\sigma_{n+1} = s_{n+1} + p_{n+1}\mathbf{I}$$

$$\varepsilon_{n+1}^e = \frac{1}{2G}s_{n+1} + \frac{1}{3}\varepsilon_{v_{n+1}}^{e\,trial}\mathbf{I}$$

$$\overline{\varepsilon}_{n+1}^p = \overline{\varepsilon}_n^p + \Delta\gamma$$

Then exit the procedure.

However, it is essential to note that σ_{n+1} is generally non-differentiable because its definition can change depending on the nature of the step. Consequently, two one-sided derivatives are determined: the elastic tangent modulus ($\mathbf{C}^e$) and the elastoplastic tangent modulus ($\mathbf{C}^{ep}$). The former is related to the elastic predictor procedure, whereas the latter is associated with the plastic corrector. Therefore, in order to correctly assemble the tangent stiffness matrix, it is crucial to determine the appropriate tangent operator.

If the stress is within the yield surface and no further plastic loading is anticipated, the elastic tangent modulus used corresponds to the elastic constitutive matrix associated with the proposed formulation. For example, in the case of a general 3D structure, Eq. (3.38) is employed. On the other hand, if the stress is on the yield surface and further plastic loading is expected to occur, the elastoplastic consistent tangent must be evaluated. Under plastic flow, the update for σ_{n+1} is given as[59]:

$$\sigma_{n+1} = \left[\mathbf{C}^e - \frac{\Delta\gamma 6G^2}{\sigma_{n+1}^{trial}}\mathbf{I}_d\right] : \varepsilon_{n+1}^{e\,trial} \tag{3.54}$$

where $\Delta\gamma$ is the solution to the return-mapping algorithm given by Eq. (3.49) and $\mathbf{I}_d$ is the deviatoric projection tensor[59]. Therefore, the elastoplastic consistent tangent modulus can be

obtained with a straightforward application of tensor differentiation rules by substituting Eq. (3.54) into Eq. (3.53):

$$\frac{\partial \sigma_{n+1}}{\partial \varepsilon_{n+1}^{e\,trial}} = \mathbf{C}^e - \frac{\Delta\gamma 6G^2}{\sigma_{n+1}^{trial}} \mathbf{I}_d - \frac{6G^2}{\sigma_{n+1}^{trial}} \varepsilon_{d\,n+1}^{e\,trial} \otimes \frac{\partial \Delta\gamma}{\partial \varepsilon_{n+1}^{e\,trial}} + \frac{\Delta\gamma 6G^2}{(\sigma_{n+1}^{trial})^2} \varepsilon_{d\,n+1}^{e\,trial} \otimes \frac{\partial \sigma_{n+1}^{trial}}{\partial \varepsilon_{n+1}^{e\,trial}} \tag{3.55}$$

where:

$$\frac{\partial \sigma_{n+1}^{trial}}{\partial \varepsilon_{n+1}^{e\,trial}} = 2G\sqrt{\frac{3}{2}} \overline{\mathbf{N}}_{n+1} \tag{3.56}$$

in which the defined unit flow vector is defined as:

$$\overline{\mathbf{N}}_{n+1} \equiv \sqrt{\frac{2}{3}} \mathbf{N}_{n+1} = \frac{\mathbf{s}_{n+1}^{trial}}{\|\mathbf{s}_{n+1}^{trial}\|} \tag{3.57}$$

and also:

$$\frac{\partial \Delta\gamma}{\partial \varepsilon_{n+1}^{e\,trial}} = \frac{2G}{3G+H} \sqrt{\frac{3}{2}} \overline{\mathbf{N}}_{n+1} \tag{3.58}$$

Finally, by substituting Eq. (3.56) and Eq. (3.58) into Eq. (3.55), the elastoplastic tangent operator consistent with the implicit return-mapping algorithm for the von Mises with isotropic hardening model can be computed as follows:

$$\begin{aligned}
\mathbf{C}^{ep} &= \mathbf{C}^e - \frac{\Delta\gamma 6G^2}{\sigma_{n+1}^{trial}} \mathbf{I}_d + 6G^2 \left(\frac{\Delta\gamma}{\sigma_{n+1}^{trial}} - \frac{1}{3G+H} \right) \overline{\mathbf{N}}_{n+1} \otimes \overline{\mathbf{N}}_{n+1} \\
&= 2G \left(1 - \frac{\Delta\gamma 3G}{\sigma_{n+1}^{trial}} \right) \mathbf{I}_d + 6G^2 \left(\frac{\Delta\gamma}{\sigma_{n+1}^{trial}} - \frac{1}{3G+H} \right) \overline{\mathbf{N}}_{n+1} \otimes \overline{\mathbf{N}}_{n+1} + K\mathbf{I} \otimes \mathbf{I}
\end{aligned} \tag{3.59}$$

It is important to emphasize that this $\mathbf{C}^{ep}$ operator is symmetric.

Alternatively, in early implicit elastoplastic implementations, the continuum tangent operator was exclusively employed. For the von Mises model with isotropic strain hardening, it can be defined as:

$$\mathbf{C}_c^{ep} = \mathbf{C}^e - \frac{6G^2}{3G+H} \overline{\mathbf{N}} \otimes \overline{\mathbf{N}} \quad \Rightarrow \quad \mathbf{C}^{ep} = \mathbf{C}_c^{ep} - \frac{\Delta\gamma 6G^2}{\sigma_{n+1}^{trial}} \left[\mathbf{I}_d - \overline{\mathbf{N}}_{n+1} \otimes \overline{\mathbf{N}}_{n+1} \right] \tag{3.60}$$

Ensuring the consistency of the numerical method, if $\Delta\gamma$ is set to zero, as in the first iteration of each load increment, both elastoplastic operators become equal. However, as $\Delta\gamma$ increases, the difference between the continuum and consistent approaches grows.

Since, the consistent tangent operator is required to guarantee the quadratic convergence presented by the Newton-Raphson approach[59], using the continuum tangent operator for assembling the stiffness matrix could significantly reduce the overall convergence rate in the global iterative process[59]. Consequently, this work exclusively employs the consistent tangent operator.

Figure 7 – Schematic plastic corrector algorithm.
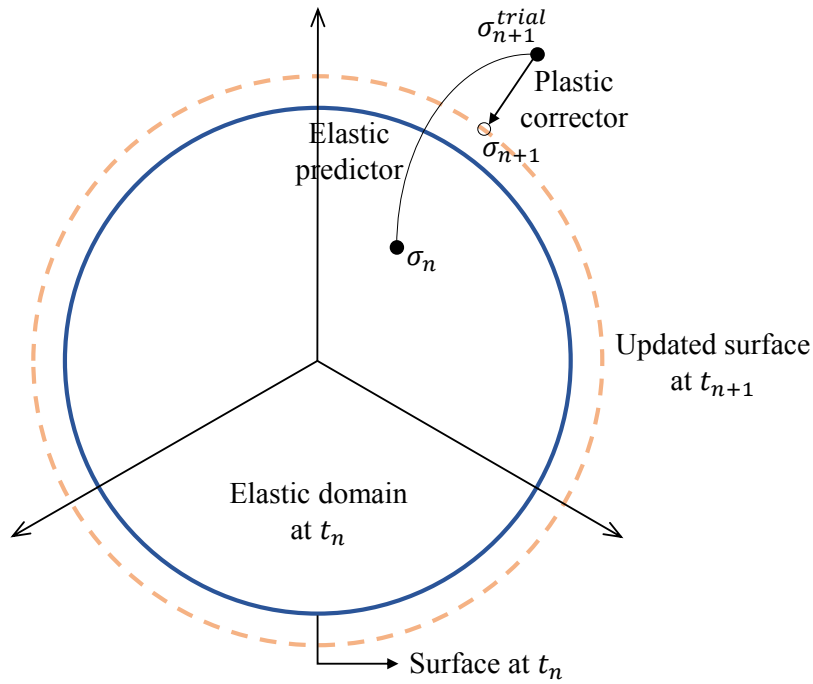
Source: The author.

3.6 Isogeometric analysis

Regarding the Isogeometric analysis (IGA)[21], the functions provided by CAD systems are integrated into the numerical simulation. This innovative approach utilizes the geometric representation provided by CAD systems to not only define the geometry of the solid but also to compute the field solution. In this work, the isogeometric representation relies exclusively on Non-Uniform Rational B-Splines (NURBS) due to their unique characteristics and features. A more comprehensive exploration of the unique attributes of NURBS is presented in subsequent Appendix A.

In the realm of IGA, any given structure can be expressed as a linear combination of the basis functions in conjunction with their associated control points. When considering Cartesian coordinates within a three-dimensional real space, their coordinates can be expressed by[21, 23]:

$$x = \sum_{i=1}^{np} R_i(\xi, \eta, \zeta) x_i, \quad y = \sum_{i=1}^{np} R_i(\xi, \eta, \zeta) y_i, \quad z = \sum_{i=1}^{np} R_i(\xi, \eta, \zeta) z_i \tag{3.61}$$

where $R_i(\xi, \eta, \zeta)$ are the NURBS basis functions and x_i, y_i, z_i are the $\mathbf{p}_i$ control points coordinates. Then, the displacements can be approximated using the same basis functions adopted to describe the geometry. Thus, the displacements are described as:

$$u = \sum_{i=1}^{np} R_i(\xi, \eta, \zeta) u_i, \quad v = \sum_{i=1}^{np} R_i(\xi, \eta, \zeta) v_i, \quad w = \sum_{i=1}^{np} R_i(\xi, \eta, \zeta) w_i \tag{3.62}$$

Additionally, in this work, the Bézier extraction procedure is employed[72]. This methodology involves transforming NURBS basis functions into local Bézier shape functions. Thus, instead of evaluating basis functions over a complete patch, numerical integration can be carried out efficiently over the local elements corresponding to the knot spans. Therefore, this procedure allows this NURBS-based approach to be included into the finite element framework. If required, a more detailed explanation can be found in Barroso[23]. Consequently, following the establishment of the shape functions for the Isogeometric analysis elements, the remainder of the 3D formulation shown in the previous sections remain valid.

Moreover, similar to the methodology introduced to finite elements[62, 63], Isogeometric analysis can also extend its application to represent FGM composites. However, in this particular context, the Isogeometric Analysis approach presents a noteworthy difference when compared to the one previously defined for FEM. Since control points are not generally interpolated by NURBS, the volume fraction is initially evaluated for n_{sp} sample points considering the initial geometry. Given that n_{sp} is greater than the number of control points n_p, the volume fraction V_c at the control points can be computed by employing the least square method[73]:

$$\left(\overline{\mathbf{R}}^T \overline{\mathbf{R}}\right) \mathbf{V}_c = \left(\overline{\mathbf{R}}^T \overline{\mathbf{V}}_c\right) \tag{3.63}$$

where $\overline{\mathbf{R}}$ is the matrix of NURBS basis functions and $\overline{\mathbf{V}}_c$ is the matrix of volume fractions, both regarding sample points. Then, the NURBS basis functions are used to represent the volume fraction gradation within the solid:

$$V_c = \sum_{i=1}^{np} R_i V_{c,i} \tag{3.64}$$

In this work, this methodology is implemented in a MATLAB routine and provides an input compatible with the analysis software.

4 ISOGEOMETRIC ANALYSIS OF FG PLATES USING A QUASI-3D THEORY

Plates are plane structures whose thickness is significantly smaller than the other dimensions. Consequently, they can be effectively modeled as two-dimensional structures. In the literature, various kinematic theories are employed to assess the mechanical behaviour, with the most widely used ones being the Classical Plate Theory (CPT) and the Reissner-Mindlin Plate Theory (RMPT)[29, 33].

The CPT is the oldest theory presented for modeling plate behavior, being characterized by the simplest kinematic hypothesis. By completely disregarding the influence of transverse shear strains, it is solely recommended for the analysis of conventional thin plates.

The RMPT distinguishes itself by being able to account for the influence of transverse shear strains, assuming them to be constant throughout the thickness. Consequently, this theory is also referred to in the literature as the First-order Shear Deformation Theory (FSDT). However, as per the Continuum Mechanics, transverse shear strains of homogeneous and isotropic materials exhibit a quadratic variation along the thickness. Thus, a correction factor needs to be applied in order to enhance the result accuracy. This characteristic allows the FSDT to be applicable for both thick and thin plate analysis.

Furthermore, several High-order Shear Deformation Theories (HSDT)[74, 75, 76, 77] have been proposed to account for the variable nature of transverse shear strains through the thickness of the plate. Since they are able to obey the boundary condition of shear-free upper and lower surfaces, these theories avoids the requirement of any correction factors.

Nevertheless, all the aforementioned kinematic theories overlook the thickness stretching effect by assuming the normal transverse strain to be zero, focusing solely on the effects related to the plate mid-surface. Consequently, Quasi-3D plate theories were developed to address this limitation, including the thickness stretching while retaining the behavior of transverse shear strain discussed earlier[33, 78, 35, 79]. Thus, this approach presents a general 3D state of stress instead of the reduced state commonly portrayed by other plate theories.

Besides the differences of the presented kinematic hypotheses among the formulations, some theories require distinct continuity in basis functions during the analysis process using computational methods. The CPT, HSDT and Quasi-3D require C^1 continuity, while the FSDT requires a C^0 continuity. This makes the use of FSDT more practical for general applications, leading to its widely adoption in many commercial analysis software. However, given that transverse shear strains and normal stretching effects can be crucial due to material

gradation, the Quasi-3D theory is employed. In this work, among the alternatives presented in the literature, the Reddy's Quasi-3D Theory is adopted due to its relative simplicity.

Furthermore, in order to develop a novel formulation capable of utilizing 3D constitutive relations, the Quasi-3D formulation is defined based on a degenerate solid approach. This methodology is commonly employed for shell elements, where the geometry is represented by the mid-surface in addition to a normal vector. Consequently, the plate geometry is modeled by a surface, while the strain and stresses are related using 3D constitutive equations and the numerical integration uses the same scheme adopted for solid elements. Therefore, while the literature employs a mathematical development based on stress-resultants, this methodology allows for a stress-focused approach, making it more suitable to the consideration of material nonlinearity.

4.1 Reddy's Quasi-3D Plate Theory

According to the Reddy's Quasi-3D Theory[33], the displacement field within the plate can be obtained by expanding the midplane displacements along the thickness direction. Primarily, the in-plane displacements are expanded up to cubic terms to obtain quadratic transverse shear strains, whilst the transverse displacement is up to quadratic terms to obtain a linear variation of the stretching, as follows:

$$u_1(x,y,z) = u(x,y) - z\beta_x + z^2\phi_x + z^3\psi_x$$
$$u_2(x,y,z) = v(x,y) - z\beta_y + z^2\phi_y + z^3\psi_y \quad (4.1)$$
$$u_3(x,y,z) = w(x,y) + z\beta_z + z^2\phi_z$$

where the parameters u, v, w are the displacements along the xy-plane when $z = 0$, i.e., the undeformed plate midplane. It is important to note that, by using the general displacement field represented in Eq. (4.1), there are 11 generalized displacements ($u, v, w, \beta_x, \beta_y, \beta_z, \phi_x, \phi_y, \phi_z, \psi_x, \psi_y$), which would require 11 differential equations in order to determine them.

However, the displacement field can be simplified by applying boundary conditions regarding the strains. Thus, by assuming that the plate top and bottom surfaces are free of any tangential forces and transverse shear stresses:

$$\gamma_{xz}(x,y,\pm h/2) = -\beta_x + w_{,x} + \frac{h}{2}(2\phi_x + \beta_{z,x}) + \frac{h^2}{4}(3\psi_x + \phi_{z,x}) = 0$$
$$\gamma_{yz}(x,y,\pm h/2) = -\beta_y + w_{,y} + \frac{h}{2}(2\phi_y + \beta_{z,y}) + \frac{h^2}{4}(3\psi_y + \phi_{z,y}) = 0 \quad (4.2)$$

Then, it is possible to define ψ_i in terms of w, β_i, $\phi_{z,i}$ and also ϕ_i in terms of $\beta_{z,i}$:

$$\psi_x = \frac{-\phi_{z,x}}{3} - \frac{4}{3h^2}(-\beta_x + w_{,x}), \quad \phi_x = -\frac{\beta_{z,x}}{2}$$
$$\psi_y = \frac{-\phi_{z,y}}{3} - \frac{4}{3h^2}(-\beta_y + w_{,y}), \quad \phi_y = -\frac{\beta_{z,y}}{2}$$

(4.3)

By applying Eq. (4.3) in Eq. (4.1), the new displacement field is given as follows:

$$u_1(x,y,z) = u(x,y) - z\beta_x - \frac{z^2}{2}\beta_{z,x} - z^3\frac{4}{3h^2}(w_{,x} - \beta_x) - \frac{z^3}{3}\phi_{z,x}$$
$$u_2(x,y,z) = v(x,y) - z\beta_y - \frac{z^2}{2}\beta_{z,y} - z^3\frac{4}{3h^2}(w_{,y} - \beta_y) - \frac{z^3}{3}\phi_{z,y}$$
$$u_3(x,y,z) = w(x,y) + z\beta_z + z^2\phi_z$$

(4.4)

These equations can be written as:

$$u_1(x,y,z) = u_1(x,y,z) + zw_{,x} - zw_{,x} = u(x,y) - zw_{,x} + (z - z^3\frac{4}{3h^2})(w_{,x} - \beta_x) - \frac{z^2}{2}\beta_{z,x} - \frac{z^3}{3}\phi_{z,x}$$
$$u_2(x,y,z) = u_2(x,y,z) + zw_{,y} - zw_{,y} = v(x,y) - zw_{,y} + (z - z^3\frac{4}{3h^2})(w_{,y} - \beta_y) - \frac{z^2}{2}\beta_{z,y} - \frac{z^3}{3}\phi_{z,y}$$
$$u_3(x,y,z) = w(x,y) + z\beta_z + z^2\phi_z$$

(4.5)

Therefore, it is possible to observe that the number of generalized displacements is reduced to 7 ($u, v, w, \beta_x, \beta_y, \beta_z, \phi_z$), where β_x and β_y are the rotations, β_z and ϕ_z are the stretching related terms.

Furthermore, it is interesting to note that the aforementioned displacement field shown in Eq. (4.5) can be generalized to accommodate other variations across the thickness:

$$u_1(x,y,z) = u(x,y) - zw_{,x} + f(z)(w_{,x} - \beta_x) + h(z)\beta_{z,x} + g(z)\phi_{z,x}$$
$$u_2(x,y,z) = v(x,y) - zw_{,y} + f(z)(w_{,y} - \beta_y) + h(z)\beta_{z,y} + g(z)\phi_{z,y}$$
$$u_3(x,y,z) = w(x,y) + h^*(z)\beta_z + g^*(z)\phi_z$$

(4.6)

where $f(z)$ dictates the transverse shear strains profile, and $h(z)$, $g(z)$, $h^*(z)$ and $g^*(z)$ are related to the stretching. For a function to be a valid solution, the plate top and bottom surfaces have to be free of any tangential forces and transverse shear stresses:

$$\gamma_{xz} = f'(\pm\frac{h}{2})(w_{,x} - \beta_x) = 0 \quad \Rightarrow \quad f'(\pm\frac{h}{2}) = 0$$

(4.7)

Subsequently, it is assumed that both β_z and ϕ_z must have no influence on the transverse shear strains throughout the thickness:

$$\gamma_{xz} = f'(z)(w_{,x} - \beta_x) + (h'(z) + h^*(z))\beta_{z,x} + (g'(z) + g^*(z))\phi_{z,x} \quad \Rightarrow$$

$$h'(z) + h^*(z) = 0, \quad g'(z) + g^*(z) = 0 \quad \forall \quad \frac{-h}{2} \leq z \leq \frac{h}{2} \tag{4.8}$$

$$h^*(z) = -h'(z), \quad g^*(z) = -g'(z)$$

Finally, by substituting Eq. (4.8) in Eq. (4.6), a general displacement field for the Quasi-3D Plate Theory can be defined as:

$$u_1(x,y,z) = u(x,y) - zw_{,x} + f(z)(w_{,x} - \beta_x) + h(z)\beta_{z,x} + g(z)\phi_{z,x}$$

$$u_2(x,y,z) = v(x,y) - zw_{,y} + f(z)(w_{,y} - \beta_y) + h(z)\beta_{z,y} + g(z)\phi_{z,y} \tag{4.9}$$

$$u_3(x,y,z) = w(x,y) - h'(z)\beta_z - g'(z)\phi_z$$

The corresponding strains are given by:

$$\varepsilon_{xx} = u_{,x} - zw_{,xx} + f(z)(w_{,xx} - \beta_{x,x}) + h(z)\beta_{z,xx} + g(z)\phi_{z,xx}$$

$$\varepsilon_{yy} = v_{,y} - zw_{,yy} + f(z)(w_{,yy} - \beta_{y,y}) + h(z)\beta_{z,yy} + g(z)\phi_{z,yy}$$

$$\varepsilon_{zz} = -h''(z)\beta_z - g''(z)\phi_z$$

$$\gamma_{xy} = u_{,y} + v_{,x} - 2zw_{,xy} + f(z)(2w_{,xy} - \beta_{x,y} - \beta_{y,x}) + 2h(z)\beta_{z,xy} + 2g(z)\phi_{z,xy} \tag{4.10}$$

$$\gamma_{xz} = f'(z)(w_{,x} - \beta_x)$$

$$\gamma_{yz} = f'(z)(w_{,y} - \beta_y)$$

Additionally, in order to consider the geometric nonlinearity, the strains are assumed to be small, whilst the displacements and rotations are assumed to be moderately large. Thus, the nonlinear terms are given by:

$$(u_{1,x})^2 = (u_{2,x})^2 = (u_{1,y})^2 = (u_{2,y})^2 \approx 0$$

$$(u_{3,x})^2 \approx (w_{,x})^2, \quad (u_{3,y})^2 \approx (w_{,y})^2, \quad u_{3,x}u_{3,y} \approx w_{,x}w_{,y} \tag{4.11}$$

Therefore, the von Karman[64] membrane strains contributions are added into the strains defined

by Eq. (4.10):

$$\varepsilon_{xx} = u_{,x} + \frac{1}{2}w_{,x}^2 - zw_{,xx} + f(z)(w_{,xx} - \beta_{x,x}) + h(z)\beta_{z,xx} + g(z)\phi_{z,xx}$$

$$\varepsilon_{yy} = v_{,y} + \frac{1}{2}w_{,y}^2 - zw_{,yy} + f(z)(w_{,yy} - \beta_{y,y}) + h(z)\beta_{z,yy} + g(z)\phi_{z,yy}$$

$$\varepsilon_{zz} = -h''(z)\beta_z - g''(z)\phi_z \tag{4.12}$$

$$\gamma_{xy} = u_{,y} + v_{,x} + w_{,x}w_{,y} - 2zw_{,xy} + f(z)(2w_{,xy} - \beta_{x,y} - \beta_{y,x}) + 2h(z)\beta_{z,xy} + 2g(z)\phi_{z,xy}$$

$$\gamma_{xz} = f'(z)(w_{,x} - \beta_x)$$

$$\gamma_{yz} = f'(z)(w_{,y} - \beta_y)$$

The polynomial profile provides a straightforward approach to representing the displacement behavior. By defining the functions as follows:

$$f(z) = z - z^3\frac{4}{3h^2}, \quad h(z) = -z^2/2, \quad g(z) = -z^3/3 \tag{4.13}$$

the Reddy's displacement field described in Eq. (4.5) is obtained and will be employed in this study (being called as Q3D7).

Furthermore, it is important to remark that, according to variational methods[70], when derivatives of order m appear in the functional, essential boundary conditions also involves derivatives of order zero through $m-1$, with the zeroth derivative being the variable itself. Therefore, although this formulation presents 7 DoFs (u, v, w, β_x, β_y, β_z, ϕ_z), other 6 essential boundary conditions are also set during the mathematical development: $w_{,x}$, $w_{,y}$, $\beta_{z,x}$, $\beta_{z,y}$, $\phi_{z,x}$, $\phi_{z,y}$.

As a weak form approach will be further employed, only essential boundary conditions are directly enforced, but the natural boundary conditions associated with them are documented in the literature[33]. For instance, simply supported ends may only enforce some of the 7 DoFs. On the other hand, clamped ends require the enforcement of the other 6 essential boundary conditions, which results in a more complex process.

Regarding the strain-displacement relations, it can be noted that the transverse shear strains, γ_{xz} and γ_{yz}, exhibit a quadratic variation through the thickness, as expected due to using the same profile as the Reddy's Third-order Theory[29]. Additionally, the transverse normal strain ε_{zz} is defined by a complete linear polynomial along the thickness, characterizing the plate stretching.

4.1.1   Specialization to other theories

The parameters $f(z)$, $h(z)$, $g(z)$ presented in Eqs. (4.9) and (4.10) can be modified to achieve various profiles and even simpler kinematic theories.

While Reddy's formulation present a complete linear polynomial for the thickness normal strain, as shown in Eq. (4.5), some works within the literature neglect the quadratic term ($g(z) = 0$), leading to a constant normal strain throughout the thickness. However, previous research on shell structures has shown that the sole inclusion of a linear term leads to Poisson locking, not being able to accurately represent the stretching[80, 81].

On the other hand, Moita et al.[34] only excludes the linear term ($h(z) = 0$). Consequently, while no longer qualifying as a complete polynomial, the normal strain throughout the thickness presents a linear behavior. In order to explore potential capabilities and limitations, this alternative Quasi-3D approach is also further employed in this work (also called as Q3D6). The displacement field is given as follows:

$$u_1(x,y,z) = u(x,y) - z\,w_{,x} + (z - z^3\frac{4}{3h^2})(w_{,x} - \beta_x) - \frac{z^3}{3}\phi_{z,x}$$

$$u_2(x,y,z) = v(x,y) - z\,w_{,y} + (z - z^3\frac{4}{3h^2})(w_{,y} - \beta_y) - \frac{z^3}{3}\phi_{z,y} \qquad (4.14)$$

$$u_3(x,y,z) = w(x,y) + z^2\phi_z$$

Then, the strain-displacement relations are described as:

$$\varepsilon_{xx} = u_{,x} - z\,w_{,xx} + (z - z^3\frac{4}{3h^2})(w_{,xx} - \beta_{x,x}) + \frac{z^3}{3}\phi_{z,xx}$$

$$\varepsilon_{yy} = v_{,y} - z\,w_{,yy} + (z - z^3\frac{4}{3h^2})(w_{,yy} - \beta_{y,y}) + \frac{z^3}{3}\phi_{z,yy}$$

$$\varepsilon_{zz} = -2z\phi_z$$

$$\gamma_{xy} = u_{,y} + v_{,x} - 2zw_{,xy} + (z - z^3\frac{4}{3h^2})(2w_{,xy} - \beta_{x,y} - \beta_{y,x}) + \frac{z^3}{3}\phi_{z,xy} \qquad (4.15)$$

$$\gamma_{xz} = (1 - 3z^2\frac{4}{3h^2})(w_{,x} - \beta_x)$$

$$\gamma_{yz} = (1 - 3z^2\frac{4}{3h^2})(w_{,y} - \beta_y)$$

Regarding the geometric nonlinearity, the assumptions and terms are the same as defined in Eq. (4.11).

Furthermore, if both thickness stretching terms are disregarded ($h(z) = g(z) = 0$),

the resulting field is a general Higher-order Shear Deformation Theory:

$$u_1(x,y,z) = u(x,y) - zw_{,x} + f(z)(w_{,x} - \beta_x)$$

$$u_2(x,y,z) = v(x,y) - zw_{,y} + f(z)(w_{,y} - \beta_y) \tag{4.16}$$

$$u_3(x,y,z) = w(x,y)$$

Within the HSDT literature, transverse shear strains were described by polynomials[33], trigonometric[75], hyperbolic[76] and exponential[77] functions. Additionally, the First-order Shear Deformation Theory can also be obtained by varying $f(z)$. Some of these functions are shown in Table 1.

Table 1 – $f(z)$ adopted by multiple kinematic theories.

Kinematic Theory	$f(z)$	$f'(z)$
TSDT [74]	$z - \frac{4z^3}{3h^2}$	$1 - \frac{4z^2}{h^2}$
SSDT [75]	$\frac{h}{\pi} \sin \frac{\pi z}{h}$	$\cos \frac{\pi z}{h}$
SHSDT [76]	$h \sinh \frac{z}{h} - z \cosh \frac{1}{2}$	$\cosh \frac{z}{h} - \cosh \frac{1}{2}$
ESDT [77]	$z \frac{4}{3h^2}^{-2(z/h)^2}$	$\frac{4}{3h^2}^{-2(z/h)^2} \left(1 - \frac{4z^2}{h^2}\right)$
FSDT [29]	z	1

Source: The author.

4.2 Displacements and Strains

The proposed kinematic theory requires a C^1 continuity in the basis functions, which is evident by the inclusion of second-order derivatives in the strain-displacement relations. Consequently, due to it being easily attainable through the use of Non-Uniform Rational B-Splines (NURBS) properties, the isogeometric basis functions are the only ones employed within the following mathematical development. Hence, as previously stated, any given body can be represented as a linear combination of basis functions and their corresponding control points. Considering a degenerate solid approach, the Cartesian coordinates can be expressed as[22, 23]:

$$x = \sum_{i=1}^{np} R_i(\xi,\eta) x_i, \quad y = \sum_{i=1}^{np} R_i(\xi,\eta) y_i, \quad z = \zeta \frac{h}{2} \tag{4.17}$$

where $R_i(\xi,\eta)$ are the NURBS basis functions, ζ is the parametric direction related to the thickness, h is the plate thickness and x_i, y_i are the mid-surface control points coordinates. It is pertinent to observe that the in-plane coordinates are solely defined with respect to ξ and η, whereas the out-of-plane coordinate exclusively takes ζ into account.

The IGA formulation proposes that the displacements are approximated using the same basis functions adopted to describe the geometry. Thus, given that the formulation incorporates a total of 7 DoF, the displacements can be expressed as follows:

$$u = \sum_{i=1}^{np} R_i u_i, \quad v = \sum_{i=1}^{np} R_i v_i, \quad w = \sum_{i=1}^{np} R_i w_i, \quad \beta_x = \sum_{i=1}^{np} R_i \beta_{x,i}, \quad \beta_y = \sum_{i=1}^{np} R_i \beta_{y,i},$$

$$\beta_z = \sum_{i=1}^{np} R_i \beta_{z,i}, \quad \phi_z = \sum_{i=1}^{np} R_i \phi_{z,i}$$

(4.18)

Alternatively, the matrix formulation is defined as:

$$\hat{\mathbf{u}} = \begin{bmatrix} u \\ v \\ w \\ \beta_x \\ \beta_y \\ \beta_z \\ \phi_z \end{bmatrix} = \sum_{i=1}^{np} \begin{bmatrix} R_i & 0 & 0 & 0 & 0 & 0 & 0 \\ 0 & R_i & 0 & 0 & 0 & 0 & 0 \\ 0 & 0 & R_i & 0 & 0 & 0 & 0 \\ 0 & 0 & 0 & R_i & 0 & 0 & 0 \\ 0 & 0 & 0 & 0 & R_i & 0 & 0 \\ 0 & 0 & 0 & 0 & 0 & R_i & 0 \\ 0 & 0 & 0 & 0 & 0 & 0 & R_i \end{bmatrix} \begin{bmatrix} u_i \\ v_i \\ w_i \\ \beta_{x,i} \\ \beta_{y,i} \\ \beta_{z,i} \\ \phi_{z,i} \end{bmatrix} = \sum_{i=1}^{np} \mathbf{R}_i \mathbf{u}_e = \mathbf{N} \mathbf{u}_e$$

(4.19)

Since the strain formulation requires derivatives with respect to the Cartesian space, and the displacements are defined in parametric coordinates, the derivatives are transformed through the application of the chain rule. A matrix formulation for derivatives in this particular context is given as:

$$\begin{bmatrix} R_{i,\xi} \\ R_{i,\eta} \\ R_{i,\zeta} \end{bmatrix} = \mathbf{J} \begin{bmatrix} R_{i,x} \\ R_{i,y} \\ R_{i,z} \end{bmatrix}$$

(4.20)

where $\mathbf{J}$ is the Jacobian matrix, which is evaluated by:

$$\mathbf{J} = \begin{bmatrix} \sum_{i=1}^{np} R_{i,\xi} x_i & \sum_{i=1}^{np} R_{i,\xi} y_i & 0 \\ \sum_{i=1}^{np} R_{i,\eta} x_i & \sum_{i=1}^{np} R_{i,\eta} y_i & 0 \\ 0 & 0 & \dfrac{h}{2} \end{bmatrix}$$

(4.21)

Thus, it is possible to demonstrate that the in-plane and out-of-plane derivatives are uncoupled in this formulation. Finally, in order to obtain the functions in terms of Cartesian coordinates:

$$\begin{bmatrix} R_{i,x} \\ R_{i,y} \\ R_{i,z} \end{bmatrix} = \mathbf{J}^{-1} \begin{bmatrix} R_{i,\xi} \\ R_{i,\eta} \\ R_{i,\zeta} \end{bmatrix}$$

(4.22)

In this work, the second-order of in-plane derivatives are also required. Given their uncoupled nature, their evaluation in terms of ξ and η can be accomplished through a successive application of the chain rule:

$$
\begin{aligned}
R_{i,\xi\xi} &= \left(R_{,xx}x_{,\xi}^2 + R_{,x}x_{,\xi\xi}\right) + R_{,xy}x_{,\xi}y_{,\xi} + R_{,yx}y_{,\xi}x_{,\xi} + \\
&\quad \left(R_{,yy}y_{,\xi\xi}^2 + R_{,y}y_{,\xi\xi}\right) \\
R_{i,\eta\eta} &= \left(R_{,xx}x_{,\eta}^2 + R_{,x}x_{,\eta\eta}\right) + R_{,xy}x_{,\eta}y_{,\eta} + R_{,yx}y_{,\eta}x_{,\eta} + \\
&\quad \left(R_{,yy}y_{,\eta\eta}^2 + R_{,y}y_{,\eta\eta}\right) \\
R_{i,\xi\eta} &= \left(R_{,xx}x_{,\xi}x_{\eta} + R_{,x}x_{,\xi\eta}\right) + R_{,xy}x_{,\xi}y_{,\eta} + R_{,yx}y_{,\xi}x_{,\eta} + \\
&\quad \left(R_{,yy}y_{,\xi}y_{,\eta} + R_{,y}y_{,\xi\eta}\right)
\end{aligned}
\tag{4.23}
$$

These expressions can be written in the matrix form as:

$$
\begin{bmatrix} R_{i,\xi\xi} \\ R_{i,\eta\eta} \\ R_{i,\xi\eta} \end{bmatrix} = \mathbf{J}^s \begin{bmatrix} R_{i,xx} \\ R_{i,yy} \\ R_{i,xy} \end{bmatrix} + \begin{bmatrix} x_{,\xi\xi} & y_{,\xi\xi} \\ x_{,\eta\eta} & y_{,\eta\eta} \\ x_{,\xi\eta} & y_{,\xi\eta} \end{bmatrix} \begin{bmatrix} R_{i,x} \\ R_{i,y} \end{bmatrix}
\tag{4.24}
$$

where:

$$
\mathbf{J}^s = \begin{bmatrix} x_{,\xi}^2 & y_{,\xi}^2 & 2x_{,\xi}y_{,\xi} \\ x_{,\eta}^2 & y_{,\eta}^2 & 2x_{,\eta}y_{,\eta} \\ x_{,\xi}x_{,\eta} & y_{,\xi}y_{,\eta} & (x_{,\xi}y_{,\eta} + x_{,\eta}y_{,\xi}) \end{bmatrix}
\tag{4.25}
$$

Thus, the second-order in-plane derivatives can be evaluated using:

$$
\begin{bmatrix} R_{i,xx} \\ R_{i,yy} \\ R_{i,xy} \end{bmatrix} = (\mathbf{J}^s)^{-1} \left(\begin{bmatrix} R_{i,\xi\xi} \\ R_{i,\eta\eta} \\ R_{i,\xi\eta} \end{bmatrix} - \begin{bmatrix} x_{,\xi\xi} & y_{,\xi\xi} \\ x_{,\eta\eta} & y_{,\eta\eta} \\ x_{,\xi\eta} & y_{,\xi\eta} \end{bmatrix} \begin{bmatrix} R_{i,x} \\ R_{i,y} \end{bmatrix} \right)
\tag{4.26}
$$

In order to account for the influences of geometric nonlinearity, the contributions from von Karman membrane strains are incorporated:

$$
\varepsilon = \begin{bmatrix} \varepsilon_x \\ \varepsilon_y \\ \varepsilon_z \\ \gamma_{xy} \\ \gamma_{xz} \\ \gamma_{yz} \end{bmatrix} = \underbrace{\begin{bmatrix} u_{,x} \\ v_{,y} \\ w_{,z} \\ u_{,y}+v_{,x} \\ u_{,z}+w_{,x} \\ u_{,z}+w_{,y} \end{bmatrix}}_{\varepsilon_l} + \underbrace{\begin{bmatrix} \frac{1}{2}w_{,x}^2 \\ \frac{1}{2}w_{,y}^2 \\ 0 \\ w_{,x}w_{,y} \\ 0 \\ 0 \end{bmatrix}}_{\varepsilon_{nl}}
\tag{4.27}
$$

Thus, given the displacement-strain relations shown in Eq. (4.10), the matrix formulation is defined as:

$$\varepsilon = \sum_{i=1}^{np} \begin{bmatrix} R_{i,x} & 0 & (f(z)-z)R_{i,xx} & -f(z)R_{i,x} & 0 & h(z)R_{i,xx} & g(z)R_{i,xx} \\ 0 & R_{i,y} & (f(z)-z)R_{i,yy} & 0 & -f(z)R_{i,y} & h(z)R_{i,yy} & g(z)R_{i,yy} \\ 0 & 0 & 0 & 0 & 0 & -h''(z)R_i & -g''(z)R_i \\ R_{i,y} & R_{i,x} & 2(f(z)-z)R_{i,xy} & -f(z)R_{i,y} & -f(z)R_{i,x} & 2h(z)R_{i,xy} & 2g(z)R_{i,xy} \\ 0 & 0 & f'(z)R_{i,x} & -f'(z)R_i & 0 & 0 & 0 \\ 0 & 0 & f'(z)R_{i,y} & 0 & -f'(z)R_i & 0 & 0 \end{bmatrix} \mathbf{u}_e$$

$$+ \frac{1}{2}\sum_{i=1}^{np} \begin{bmatrix} 0 & 0 & W_x R_{i,x} & 0 & 0 & 0 & 0 \\ 0 & 0 & W_y R_{i,y} & 0 & 0 & 0 & 0 \\ 0 & 0 & 0 & 0 & 0 & 0 & 0 \\ 0 & 0 & W_y R_{i,x} + W_x R_{i,y} & 0 & 0 & 0 & 0 \\ 0 & 0 & 0 & 0 & 0 & 0 & 0 \\ 0 & 0 & 0 & 0 & 0 & 0 & 0 \end{bmatrix} \mathbf{u}_e = \sum_{i=1}^{np} \left(\mathbf{B}_0 + \frac{1}{2}\mathbf{B}_L \right) \mathbf{u}_e \qquad (4.28)$$

in which:

$$W_x = \sum_{i=1}^{np} R_{i,x} w_i, \quad W_y = \sum_{i=1}^{np} R_{i,y} w_i \qquad (4.29)$$

4.3 Equilibrium Equations

After defining the matrices $\mathbf{B}_0$ and $\mathbf{B}_L$ in accordance with the Quasi-3D formulation, the internal virtual work can be computed is terms of the internal force vector ($\mathbf{g}$):

$$\delta U = \int_V \delta\varepsilon^T \sigma = \delta\mathbf{u}^T \mathbf{g} \qquad (4.30)$$

Since the geometric nonlinearity strains are considered by the von Karman terms, it can be shown that:

$$\delta\varepsilon = \overline{\mathbf{B}}\delta\mathbf{u} \qquad (4.31)$$

where:

$$\overline{\mathbf{B}} = \mathbf{B}_0 + \mathbf{B}_L \qquad (4.32)$$

resulting in:

$$\mathbf{g} = \int_V \overline{\mathbf{B}}^T \sigma \, dV \qquad (4.33)$$

It is imperative to notice that, although the Quasi-3D formulation is considered a plate kinematic theory, it presents a general state of stress. Thus, since none of the stress components are neglected, it enables the integral shown in Eq. (4.33) to be directly integrated with respect to the volume, thereby resembling a solid element.

Some studies within the literature[33, 34] adopts a methodology wherein the integration is performed first across the thickness and subsequently over the area. This approach aligns with the mathematical development of other plate theories, being employed to provide matrices related to internal forces and resultants, which can also be used to easily define the natural boundary conditions. However, since this process is limited to materials under elastic behavior, Eq. (4.33) is exclusively evaluated over the volume in this work.

Then, the external virtual work (δW_{ext}) and external load vector ($\mathbf{f}$) are computed by the equations previously presented in Section 3.2. The structural equilibrium is achieved when:

$$\mathbf{g} = \mathbf{f} \tag{4.34}$$

4.4 Tangent Stiffness Matrix

It is pertinent to remark that the approach to nonlinear analysis remains consistent with the one outlined in Section 3.4, given that the Quasi-3D structures under consideration in this study are also subjected to displacement-independent loads.

Additionally, due Quasi-3D elements being integrated over the volume and incorporating integration points across three directions, the tangent constitutive matrix can be evaluated with the same constitutive model previously employed for the 3D state. Consequently, the tangent stiffness matrix is as:

$$\mathbf{K}_T = \frac{\partial \mathbf{g}}{\partial \mathbf{u}} = \underbrace{\int_V \overline{\mathbf{B}}^T \frac{\partial \boldsymbol{\sigma}}{\partial \mathbf{u}} dV}_{\mathbf{K}_E} + \underbrace{\int_V \frac{\partial \overline{\mathbf{B}}^T}{\partial \mathbf{u}} \boldsymbol{\sigma} \, dV}_{\mathbf{K}_G} = \mathbf{K}_E + \mathbf{K}_G \tag{4.35}$$

where $\mathbf{K}_E$ and $\mathbf{K}_G$ represent the material and geometric stiffness matrices. The partial derivative $\partial \boldsymbol{\sigma} / \partial \mathbf{u}$ is defined as:

$$\frac{\partial \boldsymbol{\sigma}}{\partial \mathbf{u}} = \frac{\partial \boldsymbol{\sigma}}{\partial \boldsymbol{\varepsilon}} \frac{\partial \boldsymbol{\varepsilon}}{\partial \mathbf{u}} = \mathbf{C}_T \overline{\mathbf{B}} \tag{4.36}$$

In this context, since the same constitutive model can be adopted, the tangent constitutive matrix $\mathbf{C}_T$ is computed as detailed in 3.5. Moreover, the material stiffness matrix contribution is defined

as:

$$\mathbf{K}_E = \int_V \overline{\mathbf{B}}^T \mathbf{C}_T \overline{\mathbf{B}} \, dV \tag{4.37}$$

and the contribution from the geometric stiffness matrix is evaluated by:

$$\mathbf{K}_G = \int_V \mathbf{G}^T \mathbf{S} \mathbf{G} \, dV \tag{4.38}$$

where:

$$\mathbf{G} = \begin{bmatrix} 0 & 0 & R_{i,x} & 0 & 0 & 0 & 0 \\ 0 & 0 & R_{i,y} & 0 & 0 & 0 & 0 \end{bmatrix}, \quad \mathbf{S} = \begin{bmatrix} N_x & N_{xy} \\ N_{xy} & N_y \end{bmatrix} \tag{4.39}$$

Finally, the integration of these matrices is conducted using the Gaussian integration technique, involving integration points spanning the three parametric directions, akin to the procedure employed for a 3D element. The number of points used depends on the basis functions and on the degree of profile gradation. At each Gaussian point, the properties of Functionally Graded Materials are assessed to capture the gradation profile. The assembly of the finite elements' contributions to the global stiffness matrix is accomplished through the use of the direct stiffness method.

4.5 Boundary conditions

As previously discussed, the Quasi-3D approach involves 7 Degrees of Freedom (u, v, w, β_x, β_y, β_z, ϕ_z) for each control point. The imposition of these boundary conditions is easily achievable by Isogeometric Analysis, similar to how it is done in FEM. Consequently, modeling simply supported ends is pretty straightforward. However, as the development of the kinematic theory also accounts for another 6 essential boundary conditions ($w_{,x}$, $w_{,y}$, $\beta_{z,x}$, $\beta_{z,y}$, $\phi_{z,x}$, $\phi_{z,y}$), the imposition of clamped ends is made alternatively[41].

In this work, open knot vectors are employed, meaning that the derivatives of the shape functions at the boundaries are defined solely by the nearest two control points. Consequently, clamped ends were enforced by additionally setting $w = 0$, $\beta_z = 0$, $\phi_z = 0$ for all the control points adjacent to the boundary, as illustrated in Fig. 8. This methodology makes the NURBS approach for Quasi-3D - and every other C^1 kinematic theory - practical and efficient when compared to other numerical approaches[82]. However, it is important to note that this method of enforcing essential boundary conditions is an approximation, which may result in a marginally stiffer performance of clamped ends.

Figure 8 – Dirichlet's boundary conditions imposition.
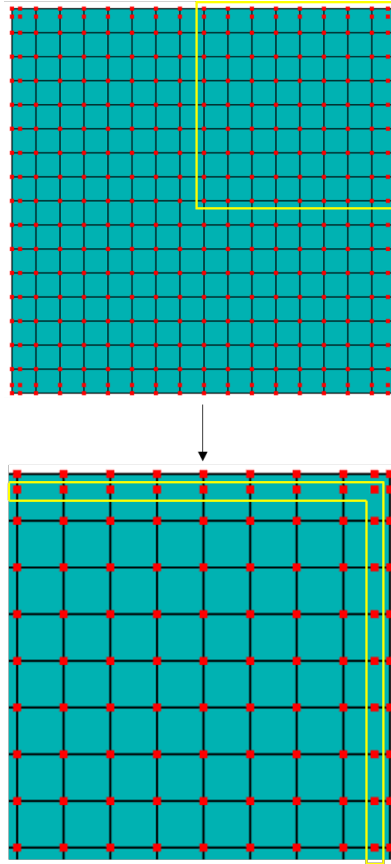
Source: The author.

It is interesting to note that for FG plates with non-symmetric material distribution along the thickness, the mechanical centroid does not coincide with the cross-section centroid. Consequently, the structure exhibits lateral deflection for any in-plane compressive load. Thus, it can be concluded that FG plates do not undergo bifurcation buckling unless displacement is constrained on all borders, which is equivalent to clamped boundary conditions all-around[83, 84]. In a complementary manner, it can also be asserted that simply-supported FG plates can only present bifurcation when exhibiting a symmetric material distribution.

4.6 Displacements and strains specialization to the 6-DoF Quasi-3D theory

The omission of the stretching linear term by setting $h(z) = 0$ leads to a new displacement field, as shown in Eq. (4.14). Therefore, it is important to note that, despite the high resemblance from majority of the NURBS-based approach presented for the 7 DoF formulation,

some key matrices are different. Each displacement can be defined as:

$$u = \sum_{i=1}^{np} R_i u_i, \quad v = \sum_{i=1}^{np} R_i v_i, \quad w = \sum_{i=1}^{np} R_i w_i, \quad \beta_x = \sum_{i=1}^{np} R_i \beta_{x,i}, \quad \beta_y = \sum_{i=1}^{np} R_i \beta_{y,i},$$

$$\phi_z = \sum_{i=1}^{np} R_i \phi_{z,i}$$

(4.40)

Since there is no β_z, the new matrix formulation excludes the row and column related to it from Eq. (4.19):

$$\hat{\mathbf{u}} = \begin{bmatrix} u \\ v \\ w \\ \beta_x \\ \beta_y \\ \beta_z \\ \phi_z \end{bmatrix} = \sum_{i=1}^{np} \begin{bmatrix} R_i & 0 & 0 & 0 & 0 & 0 \\ 0 & R_i & 0 & 0 & 0 & 0 \\ 0 & 0 & R_i & 0 & 0 & 0 \\ 0 & 0 & 0 & R_i & 0 & 0 \\ 0 & 0 & 0 & 0 & R_i & 0 \\ 0 & 0 & 0 & 0 & 0 & R_i \end{bmatrix} \begin{bmatrix} u_i \\ v_i \\ w_i \\ \beta_{x,i} \\ \beta_{y,i} \\ \phi_{z,i} \end{bmatrix} = \sum_{i=1}^{np} \mathbf{R}_i \mathbf{u}_e = \mathbf{N}\mathbf{u}_e$$

(4.41)

Furthermore, the strain-displacement relations are also different, as defined by Eq. (4.15). Consequently, the updated matrix formulation for this approach is obtained by excluding the column related to β_z from Eq. (4.19):

$$\varepsilon = \sum_{i=1}^{np} \begin{bmatrix} R_{i,x} & 0 & (f(z)-z)R_{i,xx} & -f(z)R_{i,x} & 0 & g(z)R_{i,xx} \\ 0 & R_{i,y} & (f(z)-z)R_{i,yy} & 0 & -f(z)R_{i,y} & g(z)R_{i,yy} \\ 0 & 0 & 0 & 0 & 0 & -g''(z)R_i \\ R_{i,y} & R_{i,x} & 2(f(z)-z)R_{i,xy} & -f(z)R_{i,y} & -f(z)R_{i,x} & 2g(z)R_{i,xy} \\ 0 & 0 & f'(z)R_{i,x} & -f'(z)R_i & 0 & 0 \\ 0 & 0 & f'(z)R_{i,y} & 0 & -f'(z)R_i & 0 \end{bmatrix} \mathbf{u}_e$$

$$+ \frac{1}{2} \sum_{i=1}^{np} \begin{bmatrix} 0 & 0 & W_x R_{i,x} & 0 & 0 & 0 \\ 0 & 0 & W_y R_{i,y} & 0 & 0 & 0 \\ 0 & 0 & 0 & 0 & 0 & 0 \\ 0 & 0 & W_y R_{i,x} + W_x R_{i,y} & 0 & 0 & 0 \\ 0 & 0 & 0 & 0 & 0 & 0 \\ 0 & 0 & 0 & 0 & 0 & 0 \end{bmatrix} \mathbf{u}_e = \sum_{i=1}^{np} \left(\mathbf{B}_0 + \frac{1}{2}\mathbf{B}_L \right) \mathbf{u}_e$$

(4.42)

in which:

$$W_x = \sum_{i=1}^{np} R_{i,x} w_i, \quad W_y = \sum_{i=1}^{np} R_{i,y} w_i$$

(4.43)

The rest of the formulation, encompassing the equilibrium equations, in Section 4.3, and the evaluation of the tangent stiffness matrix, in Section 4.4, remains applicable after the incorporation of the revised matrices related to the 6-DoF approach.

On the other hand, considering the framework of Higher-order Shear Deformation Theories, a reduced stress state is attained during the mathematical development, wherein the stretching terms are disregarded, leading to $\varepsilon_{zz} = 0$. Consequently, the integration process for the HSDT matrices are very different from the methodology presented for the Quasi-3D theories. If required, a detailed formulation can be found within the literature[16, 29].

5   NUMERICAL RESULTS

In this chapter, the behavior of Functionally Graded plates is studied by using the proposed formulations, considering both geometric and material nonlinearities. The results are presented in two distinct sections. Initially, the computational implementation of the previously discussed theories is validated using examples available within the literature. The numerical values are then also compared with the literature or evaluated by commercial analysis software.

Following that, parametric studies are conducted. In order to provide a thorough discussion on the influence of the nonlinearities over the mechanical response, different analyses are carried out. Moreover, when considering FG structures, many constituents are used to consider distinct composites, and their properties are presented in Table 2. The numerical analyses also encompass various length-to-thickness ratios and gradation profiles (multiple N).

Table 2 – Constituents mechanical properties.

Property	Material							
	Al	$Al-2$	ZrO_2-2	ZrO_2	SUS304	SiC	Si_3N_4	Al_2O_3
E (GPa)	70	85.8	151	200	208	302	323	380
v	0.30	0.28	0.30	0.30	0.28	0.17	0.28	0.30

Source: The author.

For a better understanding regarding the analysis methodology, it is crucial to highlight a few computational aspects. The software Rhino was used for the modeling and meshing of NURBS surfaces and solids.

Subsequently, a Python routine was employed to export the mesh to FASTModDef, where additional steps of the analysis preprocessing take place, such as the definition of sections, loads and boundary conditions. The analysis is then executed by FAST, and the results can be visualized using other compatible in-house software, such as CAP3D and NlPos.

For cases where a variation profile through NURBS basis functions is required, an Octave routine was developed to correctly evaluate a volume fraction to each control point. As previously discussed, since control points are not generally interpolated by NURBS, the approximation is computed by employing the least squares method.

Additionally, results obtained by the software ABAQUS were also used for comparison in some examples. In this case, the modeling of Functionally Graded structures was achieved by employing the virtual layer approach, where a number of fictitious plies is inserted across

the gradation direction, and the properties of each ply are evaluated using their mid-surface coordinates.

5.1 Verification examples

This section discusses the numerical examples used to guarantee the correct implementation of the formulations presented in this work. Despite the Quasi-3D kinematic theory being the main focus, other algorithms were implemented in order to fulfill the requirements to achieve the objectives presented in this work. Therefore, they are also validated.

5.1.1 Functionally Graded beam with circular cross-section

A Functionally Graded cantilever beam is subjected to a load at the tip. It has a circular cross-section and the volume fraction variation is defined in the x-axis direction:

$$V_c = 1 - \left(\frac{x}{L}\right)^N \tag{5.1}$$

where N is a user-controlled factor that allows the employment of multiple profiles. The effective properties are evaluated using the Rule of Mixtures, with $E_c = 380$ GPa and $E_m = 90$ GPa. For this example, the tip load is $P = 40$ kN, the length is $L = 10$ m, the diameter is $d = 1.456$ m and $N = 1$, as seen in Fig. 9. The essential boundary conditions are defined by a clamped end ($u = v = 0$ at $x = 0$).

Figure 9 – Functionally Graded Beam.
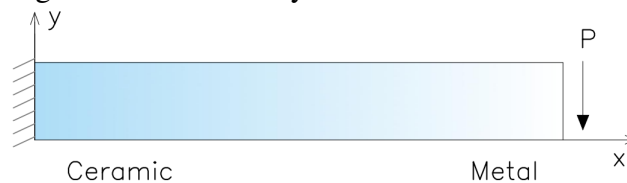
Source: The author.

Since the beam is statically determinate, a reference solution can be obtained by employing the unit load method (ULM)[85]. To enhance the accuracy of the solution, the shear contribution is considered. The tip displacement of a cantilever beam is given by:

$$w_{max} = \int_L \frac{\overline{M}M}{EI}dx + \int_L f_s\frac{\overline{Q}Q}{GA}dx = \int_0^L \frac{P(L-x)^2}{E(x)I}dx + \int_0^L f_s\frac{P}{G(x)A}dx \tag{5.2}$$

In this work, the structure is modeled as a 3D solid using IGA. The mesh comprises 8 x 4 x 4 isogeometric elements, with a finer discretization along the gradation direction. Notably,

due to the circular cross-section, shape functions need to be at least quadratic within the plane. The mesh along with the deformed configuration can be seen in Fig. 10, and the results are presented in Table 3.

Figure 10 – Isogeometric analysis of FG beam.
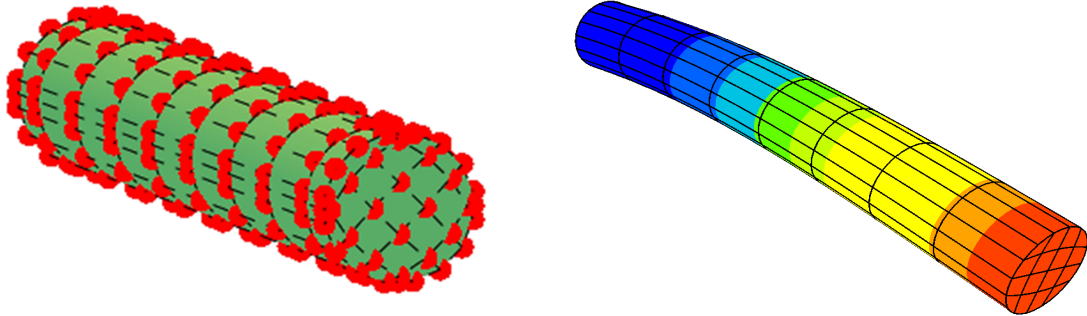
(a) 8 x 4 x 4 isogeometric quadratic mesh.   (b) Structural deformed configuration.

Source: The author.

Table 3 – FG cantilever beam tip transverse displacement.

Material	8 x 4 x 4		ULM (mm)	Diff. (Quad.)	Diff. (Cubic)
	Quadratic	Cubic			
Ceramic	0.1579	0.1588	0.1591	-0.70%	-0.17%
FGM	0.2058	0.2068	0.2081	-1.09%	-0.66%
Metal	0.6668	0.6704	0.6716	-0.70%	-0.17%

Source: The author.

As indicated in Table 3, the results are in excellent agreement. The ULM adopts beam theory assumptions, which explains the slight discrepancy when compared to the 3D model. Furthermore, due to the effective properties variation, FGM results exhibit a greater difference than the homogeneous ones.

Since geometric nonlinearity is considered in this work, the total Lagrangian 3D formulation is employed to analyze the structure under large displacements. The nonlinear load-displacement curves are presented in Fig. 11. It is interesting to note that the displacements initially increase linearly, presenting a nonlinear stiffening response for larger loads.

The displacements of a ceramic beam ($N = 0$) are compared with results obtained using the *Elastica* solution through elliptic integrals [86]. Both axial and transverse displacements are studied. The variables are measured in terms of dimensionless parameters, evaluated respectively for load and displacements by PL^2/E_cI and $v, u/L$. Then, the load-displacements curves

for ceramic, metallic, and FGM beams are shown in Fig. 11.

Figure 11 – Load-displacement curves.

(a) Transverse displacement.   (b) Axial displacement.
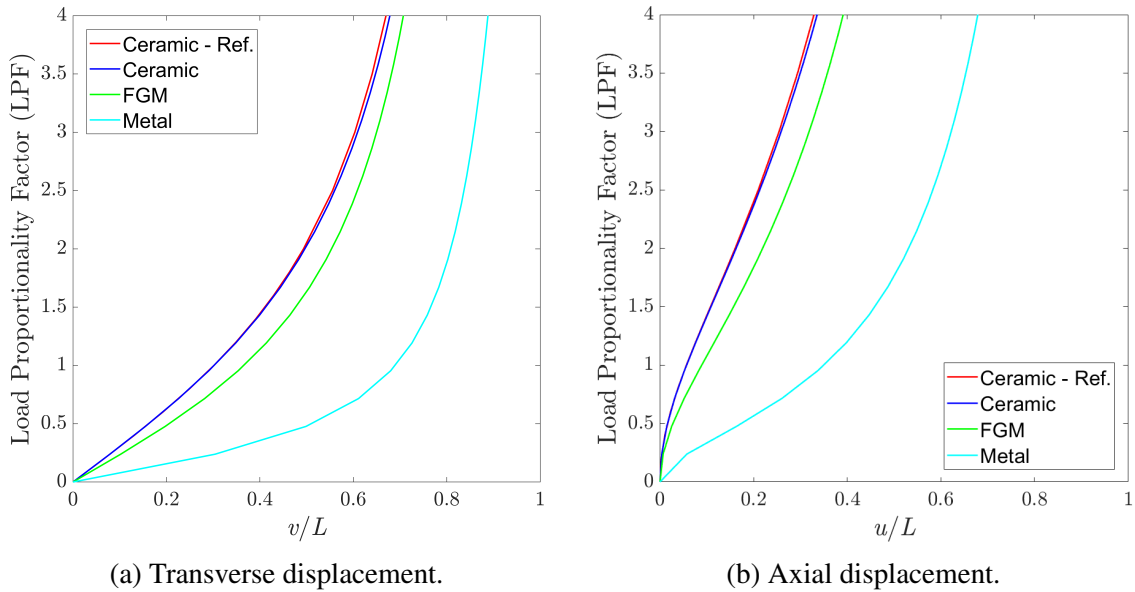
Source: The author.

It can be seen that the ceramic nonlinear response is in close agreement with the reference solution. Additionally, the FGM structure presents an intermediate load-displacement curve when regarding the constituents, which is expected. Hence, the consistency of the geometric nonlinear implementation is guaranteed.

5.1.2 *Internally pressurized cylinder*

To validate the von Mises plasticity algorithms, a thick-walled cylinder subjected to internal pressure[59] is analyzed. The outer radius is $R = 20$ cm, and the inner radius is $r = 10$ cm. The standard twenty-node finite element with (2 x 2 x 2) Gauss integration points is used to model discretization. Due to symmetry, only a quarter of the entire cylinder cross-section is modeled, as shown in Fig. 12a. The imposed boundary conditions include symmetry displacements constraints: $u = 0$ across the upper face and $v = 0$ across the lower face. The material is homogeneous, with $E = 210$ GPa, $v = 0.3$ and $\sigma_y = 0.24$ GPa, with material nonlinearity considered perfectly plastic.

The internal pressure is increased until structural collapse occurs. Plastic yielding initiates at the inner surface and progress steadily until reaching the outer surface, as illustrated in Fig. 12b. For reference, an analytical closed-form solution is used[87], with the limit pressure

being defined as:

$$P_{lim} = \frac{2\sigma_y}{\sqrt{3}} \ln(R/r) \quad \Rightarrow \quad P_{lim} \approx 0.19209 \text{ GPa} \tag{5.3}$$

Fig. 13 presents the internal pressure curve in terms of the axial displacement of the outer node, resulting in $P_{lim} = 0.19206$ GPa. The numerical results are in excellent agreement with the reference solution. The evolution of the plastic front is also shown: The transition between elastic and plastic behavior happens while there are integration points within both elastic and plastic domains.

Figure 12 – Quarter of a cylinder subjected to internal pressure.

(a) 8x5x2 mesh.　　　　　　　　(b) Partly plastified cylinder cross-section.
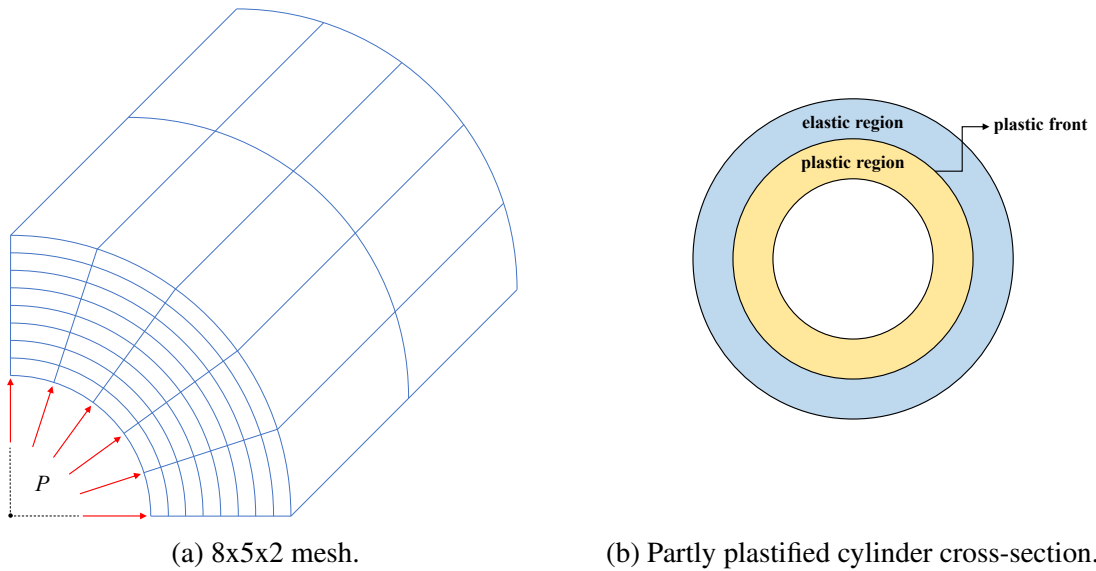
Source: The author.

5.1.3 *Square plate subjected to transverse loading*

This section verifies the proposed novel NURBS-based isogeometric approach for the Reddy's Quasi-3D Theory. Various types of analysis will be performed to ensure the correct computational implementation. Results are compared with the general 3D formulation and with other plate theories derived from the specialization of the Reddy's Quasi-3D Theory, as discussed in Section 4.1.1.

The numerical results are based on a square plate subjected to a transverse uniform load, as shown in Fig. 14. The 3D mesh consists of 16 elements in each direction over the $x - y$ plane and 4 elements in thickness (z) direction. Boundary conditions, materials and length-to-thickness relations are detailed within the description of each analysis.

Figure 13 – Pressure versus displacement diagram.
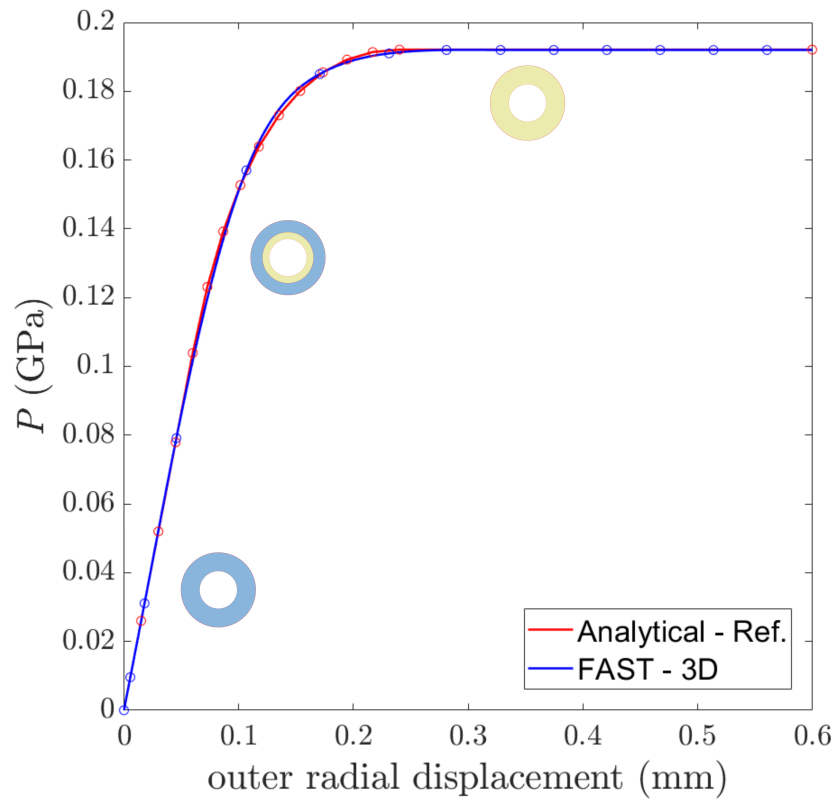
Figure 14 – Square plate subjected to transverse load.
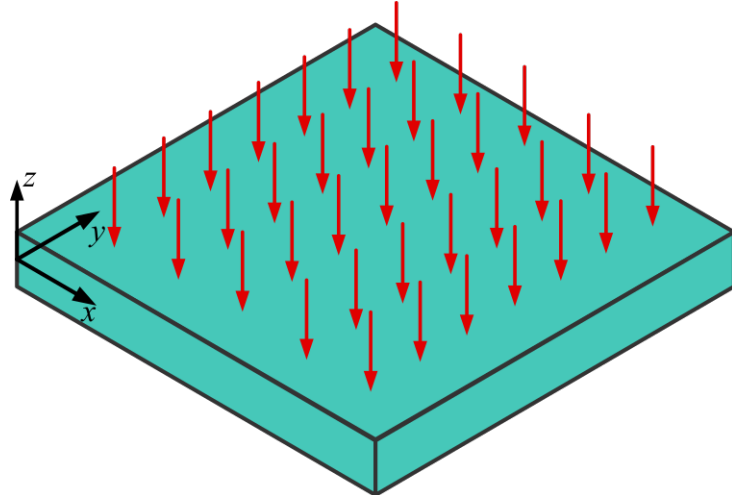
While geometry and mesh are based on a solid model for the 3D formulation, both are based on a surface model for typical plate kinematic theories. In this work, the Quasi-3D formulation, due to the degenerate solid approach, is characterized by a surface-based mesh and a solid-based section. Therefore, while it presents integration points across the three directions and performs integration over the volume, the adopted mesh is the same as for other plate theories. This aspect is illustrated in Fig. 15.

5.1.3.1 Linear elastic analysis

In this example, both Quasi-3D formulations proposed in this work (Q3D6 and Q3D7) are compared with the results obtained by Moita et al.[34] using a Quasi-3D theory with 6-DoFs (Q3D6). A linear elastic analysis is carried out for a Al/ZrO_2 FG plate subjected to a transverse load of $q = -10$ kN/m^2. Simply supported and clamped ends are employed. Results shown in Tables 4 and 5 are obtained for multiple N and length-to-thickness ratios. The dimensionless deflections are evaluated by $\overline{w} = 100E_m h^3 w/(12a^4(1-v^2)q)$.

Figure 15 – Element representation of each formulation.

(a) 3D (Solid model)   (b) HSDT (Surface model)   (c) Quasi-3D
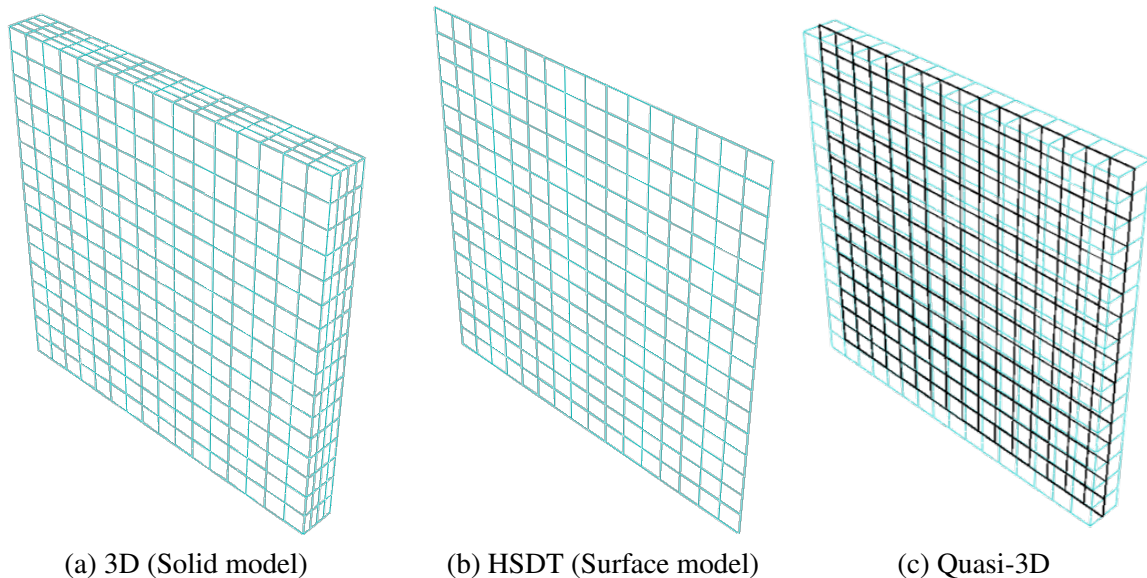
Source: The author.

As can be seen in Tables 4 and 5, the results present an excellent agreement, especially when considering Q3D6 and reference values, since both adopt the same kinematic hypotheses. Regarding the Q3D7 approach, it presents larger displacements for every instance, as expected due to the additional degree of freedom, resulting in more flexible structures.

Table 4 – Dimensionless deflection for simply-supported ends.

N	a/h	$\overline{w}$		
		Ref.[34]	Q3D6	Q3D7
0.5	5	0.231	0.233	0.234
	10	0.202	0.203	0.205
1	5	0.271	0.272	0.275
	10	0.236	0.237	0.240
2	5	0.312	0.312	0.317
	10	0.269	0.269	0.274

Source: The author.

Table 5 – Dimensionless deflection for clamped ends.

N	a/h	$\overline{w}$		
		Ref.[34]	Q3D6	Q3D7
0.5	5	0.096	0.096	0.097
	10	0.069	0.068	0.069
1	5	0.112	0.112	0.114
	10	0.080	0.080	0.081
2	5	0.131	0.131	0.134
	10	0.092	0.092	0.093

Source: The author.

Furthermore, the formulations are also compared with the 3D model to assess the overall accuracy. The dimensionless deflections for clamped ends are shown in Table 6. As can be observed, the Q3D7 formulation presents a better agreement with the solid model.

Table 6 – Dimensionless deflection for clamped ends (including the 3D model).

N	a/h	$\overline{w}$		
		Q3D7	Q3D6	3D
0.5	5	0.097	0.096	0.100
	10	0.069	0.068	0.071
1	5	0.114	0.112	0.116
	10	0.081	0.080	0.083
2	5	0.134	0.131	0.136
	10	0.093	0.092	0.095

Source: The author.

Additionally, the evaluation of stresses is also considered. For a length-to-thickness ratio $a/h = 5$ and a non-homogeneity index $N = 0.5$, the dimensionless stress is computed as $\overline{\sigma} = \sigma/(q(a/h)^2)$. The stress distribution over the thickness along a transverse normal passing through the center of the mid-surface is shown in Tables 7 and 8, and in Fig. 16. To include the

entire thickness interval, the Lobatto quadrature is employed[88] in all directions.

Table 7 – Dimensionless stresses at integration points - Quasi-3D.

z/h	$\overline{\sigma}_{xx}$		$\overline{\sigma}_{xz}$		$\overline{\sigma}_{zz}$	
	Q3D7	Q3D6	Q3D7	Q3D6	Q3D7	Q3D6
0.50	0.3930	0.3913	0.0	0.0	-0.0010	-0.0208
0.4499	0.3384	0.3369	0.0022	0.0022	-0.0037	-0.0240
0.3386	0.2272	0.2260	0.0060	0.0060	-0.0066	-0.0280
0.1816	0.0914	0.0903	0.0090	0.0090	-0.0054	-0.0281
0.0	-0.0393	-0.0405	0.0095	0.0095	-0.0007	-0.0243
-0.1816	-0.1432	-0.1447	0.0073	0.0073	0.0033	-0.0203
-0.3386	-0.2054	-0.2072	0.0039	0.0039	0.0037	-0.0186
-0.4499	-0.2174	-0.2193	0.0011	0.0011	0.0017	-0.0176
-0.50	-0.1704	-0.1720	0.0	0.0	0.0004	-0.0137

Source: The author.

As can be seen in Fig. 16, the transverse shear ($\overline{\sigma}_{xz}$) and normal ($\overline{\sigma}_{xx}$) stresses are in close agreement with the solid model, despite presenting some minor differences, which is expected due to distinct kinematic assumptions.

On the other hand, the normal stress along the thickness direction ($\overline{\sigma}_{zz}$) presents a different behavior for all of the approaches. Regarding the 3D model, since the load is applied at the upper surface, σ_{zz} presents a larger-value in $z/h = 0.5$ and decreases until reaching the lower surface. For the Quasi-3D formulations, the Q3D7 profile resembles the Q3D6, but is displaced over the x axis. It can be explained due to the additional DoF that returns a constant value over the stretching evaluation.

Table 8 – Dimensionless stresses at integration points - 3D.

z/h	3D		
	$\overline{\sigma}_{xx}$	$\overline{\sigma}_{xz}$	$\overline{\sigma}_{zz}$
0.50	0.3982	0.0006	0.0425
0.375	0.2680	0.0048	0.0368
0.250	0.1540	0.0084	0.0354
0.125	0.0494	0.0093	0.0252
0.0	-0.0409	0.0099	0.0190
-0.125	-0.1191	0.0082	0.0108
-0.250	-0.1817	0.0064	0.0044
-0.375	-0.2206	0.0030	0.0017
-0.50	-0.1747	0.0001	-0.0012

Source: The author.

Figure 16 – Dimensionless stress distribution.

(a) $\overline{\sigma}_{xx}$ (b) $\overline{\sigma}_{xz}$ (c) $\overline{\sigma}_{zz}$
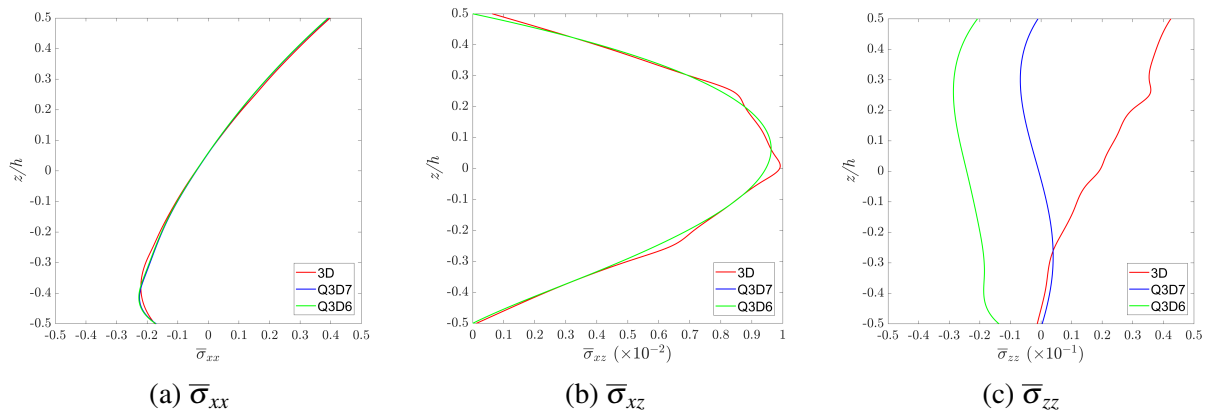
Source: The author.

5.1.3.2 *Nonlinear elastic analysis*

In this example, a geometric nonlinear elastic analysis is carried out for a Al/ZrO_2-2 FG plate subjected to a reference load of $q = -50$ kN/m^2, being further multiplied by a Load Proportionality Factor (LPF). Simply supported with constrained membrane displacements ends are employed. The length-to-thickness ratio is $a/h = 40$ and several N are adopted. The dimensionless deflections are evaluated by $\overline{w} = w/a$. Results are compared with the Reddy's Third-order Shear Deformation Theory (TSDT), which uses the same von Karman hypotheses, and the 3D model, as shown in Tables 9, 10, 11 and 12 and illustrated in Fig. 17.

Table 9 – Dimensionless deflection with geometric non-linearity - Q3D7.

LPF	N				
	0	1	2	5	∞
1	0.959	1.359	1.480	1.609	2.052
2	1.905	2.741	2.991	3.234	3.997
3	2.830	4.109	4.487	4.823	5.771
4	3.723	5.429	5.927	6.331	7.361
5	4.581	6.678	7.283	7.736	8.781
6	5.399	7.844	8.540	9.029	10.054
7	6.178	8.925	9.699	10.216	11.203
8	6.917	9.925	10.764	11.305	12.248
9	7.617	10.851	11.745	12.306	13.205

Source: The author.

As seen in Fig. 17, the Q3D7, TSDT and 3D results are in very close agreement. As expected, the plate theories' displacements reduces as the formulation present more restraining kinematic hypotheses. Additionally, due to the distinct consideration of geometric nonlinearity,

the difference between plate theories and the 3D model grows for larger deflections.

Table 10 – Dimensionless deflection with geometric nonlinearity - Q3D6.

LPF	N				
	0	1	2	5	∞
1	0.958	1.353	1.471	1.602	2.047
2	1.901	2.717	2.960	3.204	3.960
3	2.816	4.048	4.411	4.744	5.672
4	3.693	5.311	5.781	6.179	7.181
5	4.527	6.486	7.048	7.493	8.510
6	5.316	7.568	8.207	8.687	9.690
7	6.060	8.560	9.264	9.772	10.748
8	6.761	9.471	10.230	10.761	11.706
9	7.422	10.310	11.114	11.666	12.580

Source: The author.

Table 11 – Dimensionless deflection with geometric nonlinearity - TSDT.

LPF	N				
	0	1	2	5	∞
1	0.958	1.359	1.479	1.609	2.052
2	1.905	2.740	2.990	3.234	3.996
3	2.829	4.108	4.486	4.822	5.769
4	3.722	5.428	5.926	6.330	7.359
5	4.579	6.676	7.281	7.734	8.778
6	5.398	7.842	8.538	9.027	10.050
7	6.176	8.923	9.696	10.213	11.199
8	6.914	9.923	10.761	11.301	12.243
9	7.615	10.848	11.742	12.302	13.200

Source: The author.

On the other hand, it is also important to note that the Q3D6 presents a poor agreement for large displacements, despite close results for initial loads. Since other 6-DoF formulations have presented Poisson locking due to the insufficient consideration of the thickness stretching behavior, this possibility is further investigated. Consequently, the analyses are executed a second time setting $v_c = v_m = 0$. Results are shown in Tables 13, 14 and 15, and also in Figs. 18 and 19.

The results show that the differences between Q3D7 and 3D results are similar for both Poisson's ratio. However, when considering the Q3D6, the difference reduces from a maximum of about 6.5% to about 1.5% when the Poisson ratio is disregarded. This showcases the

Poisson locking of the Q3D6 formulation, which can only be solved by including an additional

DoF to improve the representation of the thickness stretching, as in the Q3D7.

Table 12 – Dimensionless deflection with geometric
nonlinearity - 3D.

LPF	N				
	0	1	2	5	∞
1	0.961	1.364	1.486	1.615	2.058
2	1.911	2.750	3.001	3.243	4.016
3	2.840	4.121	4.501	4.836	5.812
4	3.740	5.446	5.947	6.354	7.429
5	4.606	6.703	7.312	7.773	8.879
6	5.435	7.880	8.582	9.084	10.182
7	6.225	8.975	9.757	10.292	11.360
8	6.976	9.990	10.840	11.402	12.433
9	7.690	10.931	11.840	12.427	13.417

Source: The author.

Figure 17 – Dimensionless deflection with geometric
nonlinearity.
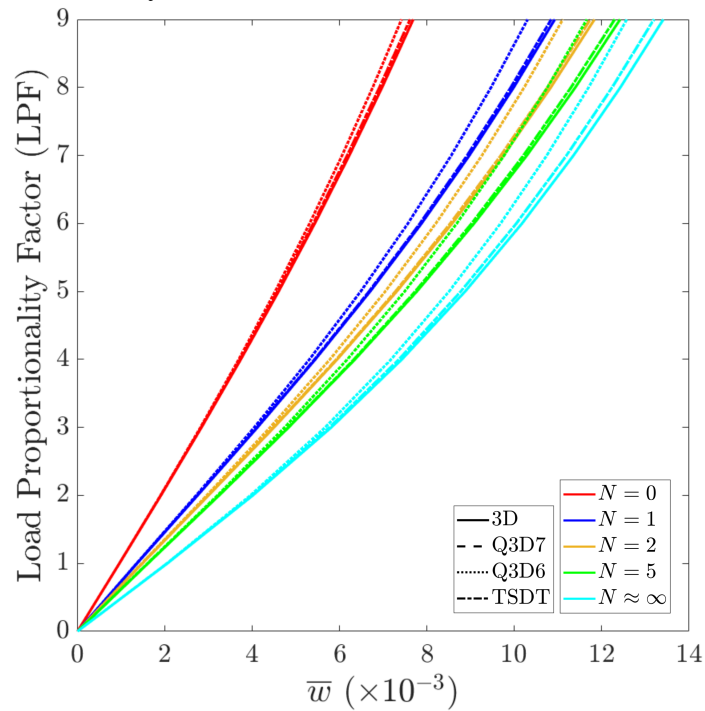
Source: The author.

Table 13 – Dimensionless deflection with geometric nonlinearity ($v = 0$) - Q3D7.

LPF	N				
	0	1	2	5	∞
1	1.060	1.506	1.641	1.783	2.269
2	2.107	3.030	3.308	3.576	4.414
3	3.128	4.531	4.948	5.317	6.364
4	4.113	5.970	6.515	6.961	8.105
5	5.057	7.325	7.982	8.484	9.655
6	5.956	8.585	9.337	9.882	11.042
7	6.809	9.750	10.582	11.161	12.292
8	7.619	10.826	11.725	12.333	13.427
9	8.385	11.820	12.778	13.410	14.467

Source: The author.

Figure 18 – Dimensionless deflection with geometric nonlinearity ($v = 0$).
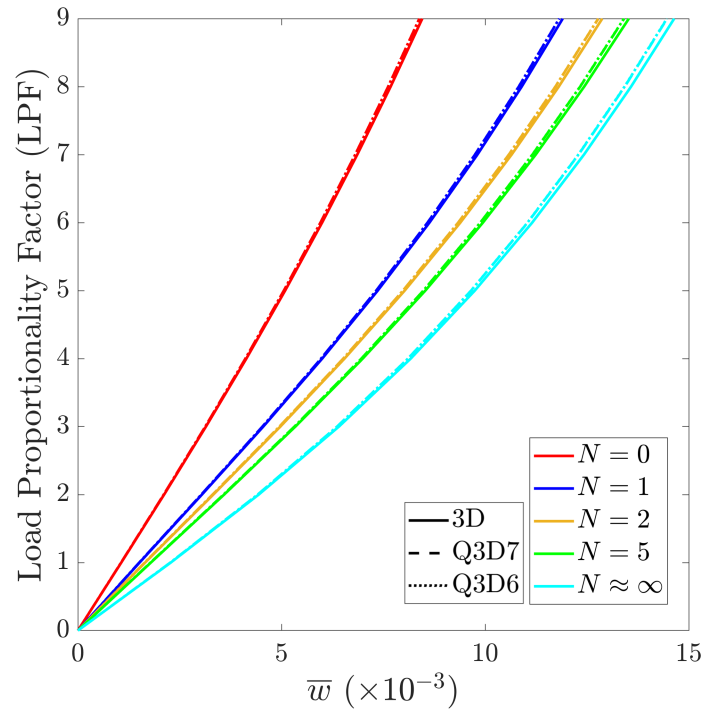
Source: The author.

Table 14 – Dimensionless deflection with geometric nonlinearity ($v = 0$) - Q3D6.

LPF	N				
	0	1	2	5	∞
1	1.060	1.506	1.641	1.783	2.269
2	2.107	3.030	3.308	3.576	4.414
3	3.128	4.531	4.948	5.317	6.363
4	4.113	5.970	6.515	6.961	8.104
5	5.056	7.324	7.982	8.483	9.653
6	5.955	8.584	9.336	9.880	11.039
7	6.809	9.749	10.581	11.159	12.288
8	7.617	10.824	11.723	12.330	13.422
9	8.383	11.818	12.775	13.407	14.461

Source: The author.

Table 15 – Dimensionless deflection with geometric nonlinearity ($v = 0$) - 3D.

LPF	N				
	0	1	2	5	∞
1	1.065	1.514	1.650	1.792	2.280
2	2.117	3.045	3.324	3.591	4.440
3	3.144	4.551	4.971	5.339	6.409
4	4.136	5.998	6.546	6.993	8.172
5	5.088	7.361	8.023	8.530	9.745
6	5.996	8.632	9.390	9.944	11.154
7	6.859	9.809	10.649	11.241	12.426
8	7.678	10.897	11.807	12.431	13.581
9	8.455	11.904	12.874	13.527	14.640

Source: The author.

5.1.3.3 *Elastoplastic analysis*

This section discusses the material nonlinear analysis of simply supported FG plates subjected to a transverse load of $q = -5$ MN/m^2. First, an homogeneous plate with $E = 200$ GPa, $v = 0.3$ and $\sigma_y = 250$ MPa with perfect plastic behavior is studied. Dimensionless deflections are evaluated by $\overline{w} = w/a$, and shown in Fig. 20 and in Table 16.

Table 16 – Ultimate load considering material nonlinearity.

v	LPF		
	Q3D7	Q3D6	3D
0.3	2.985	3.043	2.998
0.0	2.978	3.036	2.996

Source: The author.

Figure 19 – Dimensionless deflection difference between Q3D and 3D formulations.

(a) $v = 0.0$

(b) $v = 0.3$
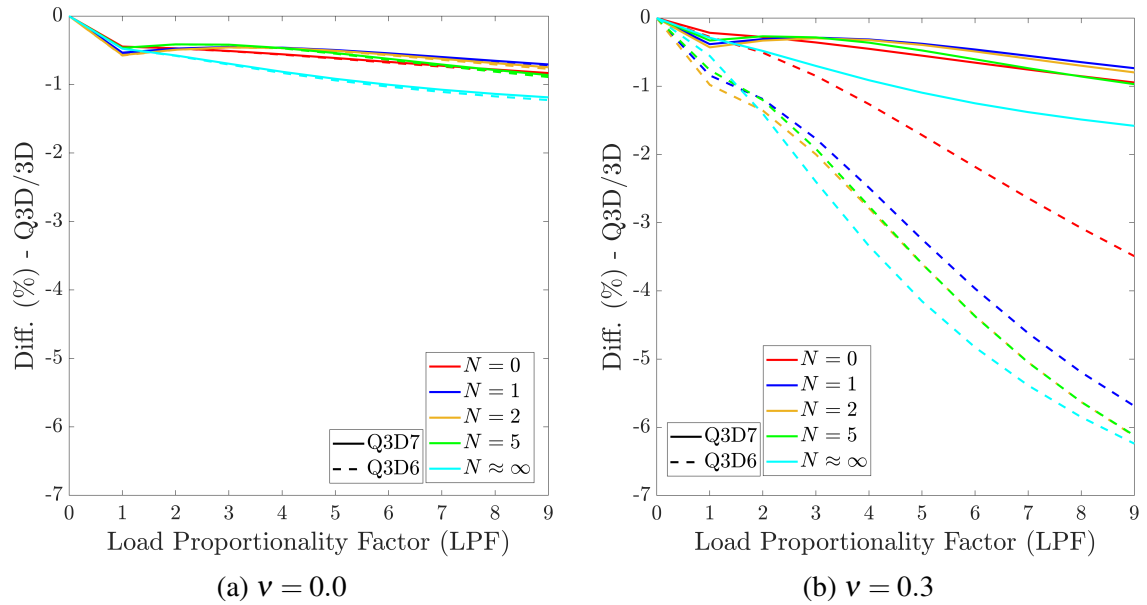
Source: The author.

Figure 20 – Load-displacement curve considering material nonlinearity.

(a) $v = 0.0$

(b) $v = 0.3$
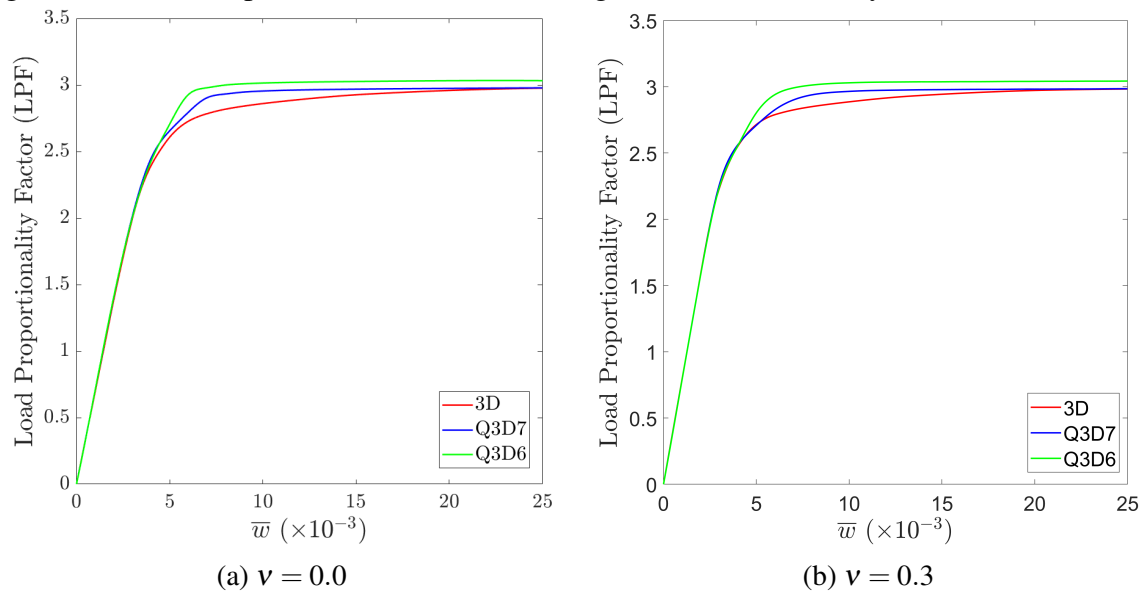
Source: The author.

In Fig. 20, it can be observed that the load-displacement curves for the Q3D7 and 3D models present an excellent agreement with respect to the ultimate load and a good overall agreement for the load-displacement curve. However, the Q3D approaches present a more flexible plastic response, reaching the critical load earlier than the solid. This can be explained due to the solid model having many more DoFs and thus a better representation of the through-thickness behavior.

Furthermore, regarding the Q3D6 approach, the results present a higher difference when compared to the 3D. However, in this case, the Poisson locking is not observed, as the differences remain stable for both values of v, as seen in Table 16. Therefore, since the Q3D7 exhibits a better overall performance, it will be employed in further analyses.

Finally, it is important to note that, in this section, the Q3D results are only compared with 3D models. While some works in the literature use the same methodology employed in solids for other plate theories, plasticity algorithms would need to be modified to be employed in problems with reduced stress states[60, 59], and none of these works consistently discusses this phenomenon.

5.2 Parametric Studies

In this section, the 7-DoF Quasi-3D formulation (Q3D7) is employed for the analysis of Functionally Graded plates. Multiple FGM components, micromechanical models, length-to-thickness ratios and types of analyses are considered. Additionally, for the sake of brevity, unless otherwise stated in the description of each problem: The gradation occurs in the thickness direction and the employed micromechanical model is the Rule of Mixtures. The mesh comprises 16x16 cubic isogeometric elements, and the Gauss quadrature is employed with 4x4x4 integration points in each element.

5.3 Elastic analysis

The first example deals with Functionally Graded square plates with linear consti-tutive relations. Both simply supported and clamped ends are considered. The influence of length-to-thickness ratios and micromechanical models in deflections and buckling critical loads is assessed.

5.3.1 Static analysis

For the static analysis of FG square plates, three distinct FGM are considered: SUS304/Si_3N_4, Al/ZrO_2 and Al/Al_2O_3. Considering simply supported ends, the dimensionless center deflection w/a is evaluated for both micromechanical models, Rule of Mixtures (RoM) and Mori-Tanaka (MT). Results are shown in Tables 17, 18 and 19.

As shown in Table 17, there is a high agreement between the results, with a maximum difference of 1.5% across various N and length-to-thickness ratios. in contrast, Table 19 indicates a poor agreement overall, with a maximum difference of 23.3%, reflecting the discrepancies between evaluations from the distinct micromechanical models. The variations in mechanical properties of the FGM components contribute to these differences. For example, while the Young's modulus ratio between SUS304 and Si_3N_4 is only 1.55, it reaches 5.43 for the Al/Al_2O_3 composite. Table 18 supports this discussion, showing intermediate differences regarding Al/ZrO_2, which presents an Young's modulus ratio is 2.86, also an intermediate value.

Table 17 – Dimensionless center deflection - SUS304/Si_3N_4.

a/h	N	$\overline{w}-$ SUS304$/Si_3N_4$		
		RoM	MT	Diff. (%)
	0	-6.99E-03	-6.99E-03	0.0
	0.5	-8.10E-03	-8.22E-03	-1.46
100	1	-8.62E-03	-8.71E-03	-1.11
	2	-9.02E-03	-9.10E-03	-0.87
	5	-9.46E-03	-9.55E-03	-1.02
	0	-8.83E-04	-8.83E-04	0.0
	0.5	-1.02E-03	-1.04E-03	-1.46
50	1	-1.09E-03	-1.10E-03	-1.11
	2	-1.14E-03	-1.15E-03	-0.88
	5	-1.20E-03	-1.21E-03	-1.01
	0	-5.88E-05	-5.88E-05	0.0
	0.5	-6.81E-05	-6.91E-05	-1.47
20	1	-7.25E-05	-7.33E-05	-1.14
	2	-7.60E-05	-7.67E-05	-0.90
	5	-7.98E-05	-8.06E-05	-1.01
	0	-7.94E-06	-7.94E-06	0.0
	0.5	-9.18E-06	-9.32E-06	-1.49
10	1	-9.78E-06	-9.90E-06	-1.18
	2	-1.03E-05	-1.04E-05	-0.95
	5	-1.08E-05	-1.09E-05	-1.00

Source: The author.

Moreover, it is important to note that the gradation profile can greatly influence the deflections regarding the micromechanical model choice. The difference in results peaks at $N = 0.5$ and reduces as the index increases. For $N = 0$, however, where the material becomes homogeneous with constant effective properties throughout the gradation, the evaluations from both models are equal. This discussion is better illustrated in Fig. 21.

Additionally, the impact of length-to-thickness ratios on the choice of the micromechanical model is found to be negligible, despite the difference in outputs still slightly increases as the plate thickness grows, which is expected.

5.3.2 *Buckling analysis*

In this example, the FG plate is now subjected to a compression load of $q = 1.0$ MN/m in the x direction, as shown in Fig. 22. A linear buckling analysis is conducted. In order to guarantee the bifurcation within the equilibrium-path, all of the plate's ends are enforced with clamped boundary conditions. Due to the non-symmetric gradation over the thickness, simply supported plates present transverse displacements for every applied load. The clamped boundary conditions are enforced as depicted in Section 4.5. Since the length-to-thickness ratio effect over the micromechanical model was found to be negligible, only two different ones are used. On the other hand, all of the three FG material are once again employed. The results are shown in Tables 20, 21 and 22.

Therefore, it can be seen that the discussion used for the static analysis in the previous section remains valid in this example. It is important to note that the Rule of Mixtures evaluates higher critical buckling loads when compared to the Mori-Tanaka model. This is illustrated in Fig. 23.

Finally, it is important to remark that the Rule of Mixtures simulates stiffer structures, evaluating higher effective mechanical properties across the entire range of gradation in contrast to the Mori-Tanaka. Therefore, despite being the most used micromechanical model within the literature, it may overestimate structural strength.

5.4   Elastoplastic analysis

This section presents a material nonlinear analysis of a FG circular plate, presenting a radius-to-thickness ratio of $r/h = 10$. Simply supported ends are enforced at the boundaries.

The effects of different micromechanical models in the elastoplastic behavior is investigated.

Table 18 – Dimensionless center deflection - Al/ZrO_2.

a/h	N	$\overline{w} - Al/ZrO_2$		
		RoM	MT	Diff. (%)
100	0	-1.11E-02	-1.11E-02	0.0
	0.5	-1.51E-02	-1.66E-02	-8.96
	1	-1.76E-02	-1.90E-02	-7.16
	2	-2.00E-02	-2.11E-02	-5.22
	5	-2.22E-02	-2.36E-02	-6.03
50	0	-1.41E-03	-1.41E-03	0.0
	0.5	-1.91E-03	-2.09E-03	-8.98
	1	-2.23E-03	-2.40E-03	-7.20
	2	-2.52E-03	-2.66E-03	-5.27
	5	-2.81E-03	-2.99E-03	-6.04
20	0	-9.37E-05	-9.37E-05	0.0
	0.5	-1.27E-04	-1.39E-04	-9.01
	1	-1.48E-04	-1.60E-04	-7.31
	2	-1.68E-04	-1.78E-04	-5.43
	5	-1.87E-04	-2.00E-04	-6.06
10	0	-1.27E-05	-1.27E-05	0.0
	0.5	-1.70E-05	-1.87E-05	-9.07
	1	-1.99E-05	-2.15E-05	-7.56
	2	-2.27E-05	-2.41E-05	-5.76
	5	-2.55E-05	-2.72E-05	-6.07

Source: The author.

Figure 21 – Difference between deflection evaluations - $a/h = 100$.
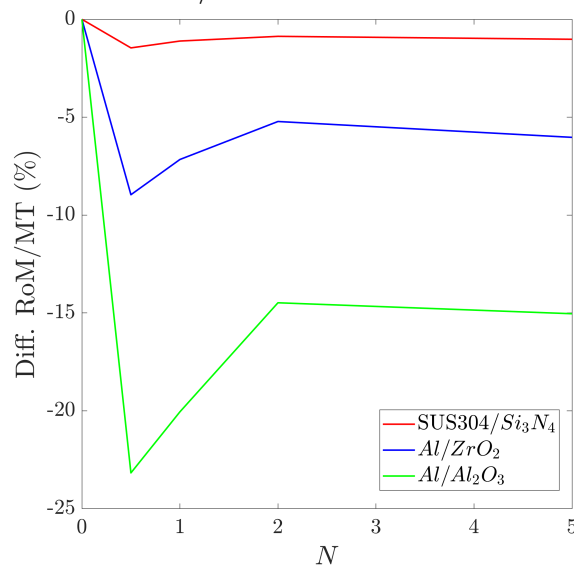
Source: The author.

Figure 22 – Square plate subjected to axial load.
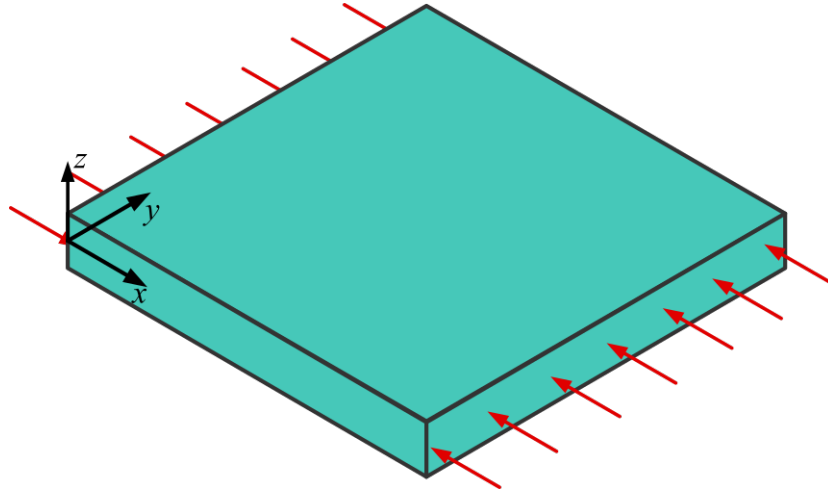
The circular mesh is first validated by analyzing a benchmark example presented in the literature[59]. The isogeometric mesh used for the Q3D7 approach and the axisymmetric FE mesh used by the reference are shown in Fig. 24. Considering a perfect plastic material of $E = 10$ MPa, $v = 0.24$ and $\sigma_y = 16$ kPa, the plate is subjected to a uniform transverse load p. The load-displacement curve for the dimensionless central deflection (w/r) is illustrated in Fig. 25. The limit load for the present problem can be computed by using the finite difference method combined with methods of limit analysis[89], which results in $P = 260.8$. The Q3D formulation achieved an ultimate load of $p = 265.87$, presenting a difference of 2%. Hence, the results present a close agreement. It is important to remark that, due to the use of rational basis functions, the isogeometric mesh is able to exactly represent the circular geometry of the plate.

Then, the circular plate is now comprised of a $Al - 2/SiC$ material[90, 91], in which $q = 183.2$ GPa[13]. Material nonlinearity is considered to be perfectly plastic. The Rule of Mixtures (RoM) and the Mori-Tanaka technique (MT) are used to evaluate the effective elastic properties. The plate is subjected to a uniform load of $p = -1.0$ MN/m^2. The load-displacement curve for the dimensionless center deflection (w/r) for multiple N is given in Fig. 26. It can be seen that the the Rule of Mixtures, by evaluating stiffer mechanical properties, presents lower displacements for any given load in every N when compared to the Mori-Tanaka.

Therefore, despite the micromechanical models being directly related to the elastic behavior, they can still influence the Tamura-Tomota-Ozawa evaluations due to the use of effective Young's modulus on the hardening modulus. However, since this is a perfectly plastic nonlinearity, the ultimate load achieved by both micromechanical models is approximately equal,

as the structure is then fully on plastic domain.

Table 19 – Dimensionless center deflection - Al/Al_2O_3.

a/h	N	$\overline{w} - Al/Al_2O_3$		
		RoM	MT	Diff. (%)
	0	-5.86E-03	-5.86E-03	0.0
	0.5	-8.88E-03	-1.16E-02	-23.17
100	1	-1.14E-02	-1.43E-02	-20.05
	2	-1.44E-02	-1.69E-02	-14.48
	5	-1.72E-02	-2.02E-02	-15.04
	0	-7.41E-04	-7.41E-04	0.0
	0.5	-1.12E-03	-1.46E-03	-23.18
50	1	-1.44E-03	-1.81E-03	-20.12
	2	-1.82E-03	-2.13E-03	-14.62
	5	-2.17E-03	-2.56E-03	-15.09
	0	-4.93E-05	-4.93E-05	0.0
	0.5	-7.43E-05	-9.68E-05	-23.22
20	1	-9.56E-05	-1.20E-04	-20.34
	2	-1.21E-04	-1.42E-04	-15.02
	5	-1.45E-04	-1.71E-04	-15.22
	0	-6.66E-06	-6.66E-06	0.0
	0.5	-9.98E-06	-1.30E-05	-23.31
10	1	-1.28E-05	-1.62E-05	-20.81
	2	-1.62E-05	-1.93E-05	-15.88
	5	-1.98E-05	-2.35E-05	-15.46

Source: The author.

Table 20 – Critical buckling load - SUS304/Si_3N_4.

a/h	N	$P_{cr}(\text{LPF}) - \text{SUS304}/Si_3N_4$		
		RoM	MT	Diff (%)
	0	2.96	2.96	0.0
	0.5	2.55	2.51	1.51
100	1	2.39	2.37	1.13
	2	2.29	2.27	0.86
	5	2.18	2.16	1.01
	0	351.34	351.34	0.0
	0.5	303.21	298.67	1.52
20	1	284.52	281.22	1.17
	2	271.04	268.60	0.91
	5	258.23	255.67	1.00

Source: The author.

Furthermore, to ensure physical consistency, it is important to note that the Mori-Tanaka micromechanical model is based on the Mean Field Homogenization, being connected to

the Eshelby Tensor[92]. In the context of isotropic materials, this tensor is symmetric. However, when FG structures undergo plastic deformation, a potential anisotropic behavior may appear, which makes this model not recommended for this type of analysis.

Table 21 – Critical buckling load - Al/ZrO_2.

a/h	N	$P_{cr}(\text{LPF}) - Al/ZrO_2$		
		RoM	MT	Diff (%)
	0	1.86	1.86	0.0
	0.5	1.37	1.24	10.19
100	1	1.16	1.08	7.86
	2	1.02	0.97	5.27
	5	0.92	0.87	6.05
	0	220.82	220.82	0.0
	0.5	162.55	147.44	10.25
20	1	138.12	127.75	8.11
	2	120.98	114.54	5.63
	5	108.58	102.39	6.04

Source: The author.

In the previous examples, the homogenization process for estimating the elastic properties occurred prior to the application of any load and the results regarding the Mori-Tanaka model were used solely for verification purposes. Therefore, the Rule of Mixtures is the only micromechanical model further employed for material nonlinear analysis in this work.

Table 22 – Critical buckling load - Al/Al_2O_3.

a/h	N	$P_{cr}(\text{LPF}) - Al/Al_2O_3$		
		RoM	MT	Diff (%)
	0	3.54	3.54	0.0
	0.5	2.31	1.76	31.65
100	1	1.77	1.40	25.79
	2	1.38	1.19	16.08
	5	1.16	1.00	15.83
	0	419.56	419.56	0.0
	0.5	275.58	209.27	31.69
20	1	210.96	166.84	26.44
	2	164.12	140.00	17.23
	5	136.37	117.43	16.12

Source: The author.

Figure 23 – Difference between critical buck-
ling evaluations for both micromechanical
models.
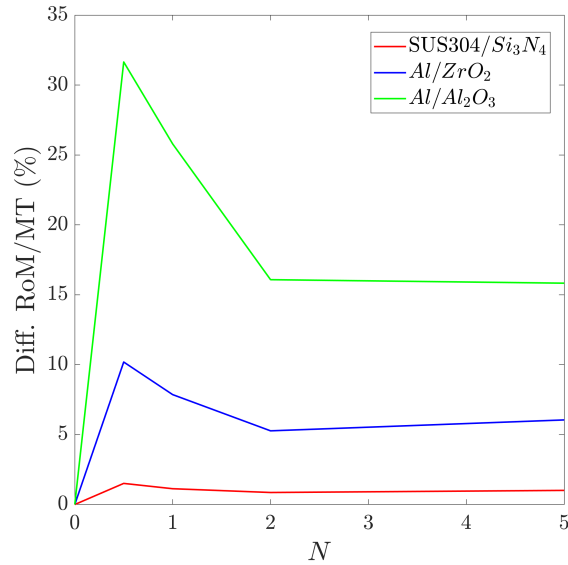
Figure 24 – Circular plate mesh.

(a) 16x16 isogeometric cubic mesh.

(b) Axisymmetric Finite Element mesh.
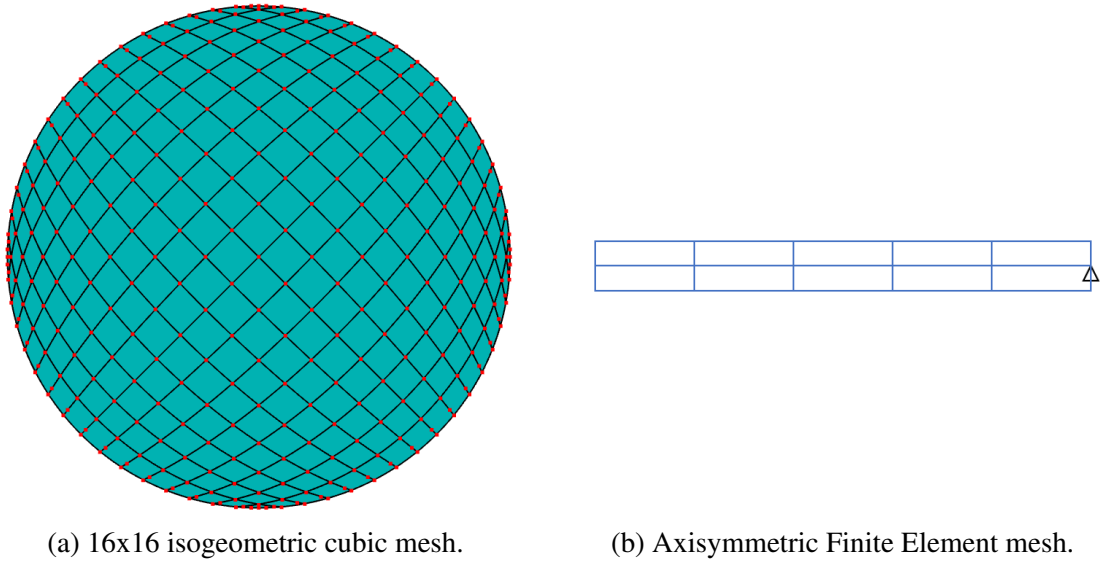
5.5 Nonlinear analysis

Finally, this example assess the nonlinear behavior of square plates. First, a homoge-
neous SUS304 plate with perfect plasticity ($\sigma_y = 205.0$ MPa) is subjected to a uniform transverse
load of -5 MN/m^2. Simply supported boundary conditions are enforced at the boundaries and
dimensionless center deflection is given by $\overline{w} = w/a$. Then, the effect of the length-to-thickness
ratio on the nonlinear behavior is assessed, as multiple load-displacement curves are shown in

Fig. 27. To present a thorough discussion, three types of analyses are carried out for each case: geometrically nonlinear (GNL), materially nonlinear (MNL), and geometrically and materially nonlinear (GMNL).

When considering the GMNL analysis, the load-displacement curve start resembling the material nonlinear behavior and, as the length-to-thickness ratio increases, it begins to resemble the geometric nonlinear behavior. For thick plates, material nonlinearity is predominant, since membrane effects are negligible when compared to the bending ones.

Figure 25 – Dimensionless deflection for homogeneous circular plate.
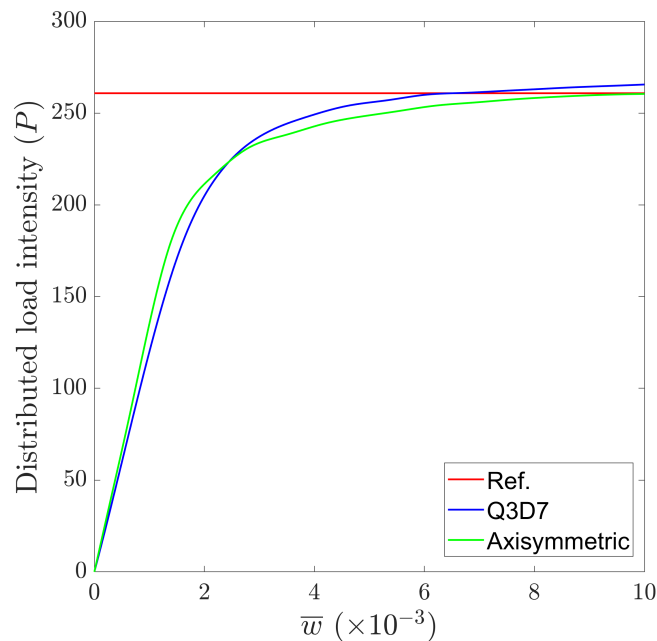
Source: The author.

This behavior can be observed in Fig. 27a, as plasticity occurs before any geometric nonlinear effect takes place. On the other hand, for thin plates the behavior is the opposite. Due to the high slenderness, membrane effects are much greater than the bending ones. Hence, in this case, the geometric nonlinearity effects already takes place during the elastic response, as seen in Fig. 27d. For intermediate values of a/h, however, both nonlinearities effects are observed, illustrated in Figs. 27b and 27c.

Then, a Functionally Graded SUS304/Si_3N_4 plate is subjected to an axial compression load $q = 1$ MN/m along the ends that are perpendicular to the x direction, as shown in Fig. 22. The material presents linear hardening plasticity, where the adopted plastic variables are $\sigma_{y,m} = 398.83$ MPa, $H_m = 1.883$ GPa and $q = 183.2$ GPa. Simply supported boundary condi-

tions are enforced at the boundaries and dimensionless center deflection is given by $\overline{w} = w/a$. Load-displacement curves for two distinct length-to-thickness ratios are shown in Fig. 28, where geometrically nonlinear analysis (GNL), and geometrically and materially nonlinear analysis (GMNL) are carried out.

Figure 26 – Dimensionless deflection for a FG circular plate.
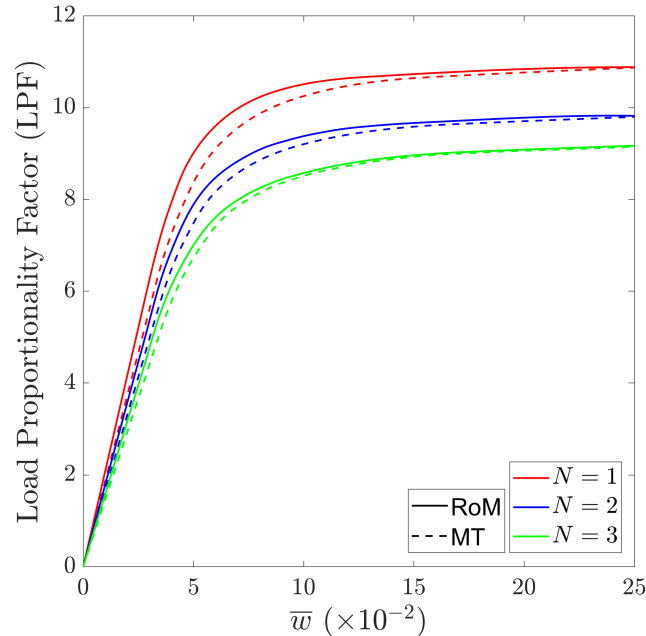
Source: The author.

Since for any $N \neq 0$ the gradation acts like an imperfection, the transverse displacements begin with the load application. In these cases, the structural load-capacity grows permanently if only the geometric nonlinearity is considered. However, when both nonlinearities are considered, the load-displacement curve changes due to the reduced structural stiffness from the plastic behavior.

In Fig. 28a, it can be observed that the material nonlinearity greatly influences the behavior early, especially for higher values of N. In some cases, the equilibrium path even presents a decrease in load capacity. On the other hand, as shown in Fig. 28b, for a thinner plate, due to the predominance of membrane effects, the material nonlinearity is only taken into account for relatively large displacements. Nevertheless, it still greatly influences the equilibrium path.

Additionally, it is important to remark that, since the plasticity is associated with the metal constituent volume fraction, the TTO cannot be employed for a homogeneous plate of

ceramic constituent, as it presents a brittle material failure. Therefore, a very small N is used to simulate its behavior. In this case, while not presenting a bifurcation point as there is a minor imperfection, the material nonlinearity effects are very small due to the negligible metal volume fraction.

Figure 27 – Load-displacement curve for a FG square plate.

(a) $a/h = 10$

(b) $a/h = 20$

(c) $a/h = 40$

(d) $a/h = 100$
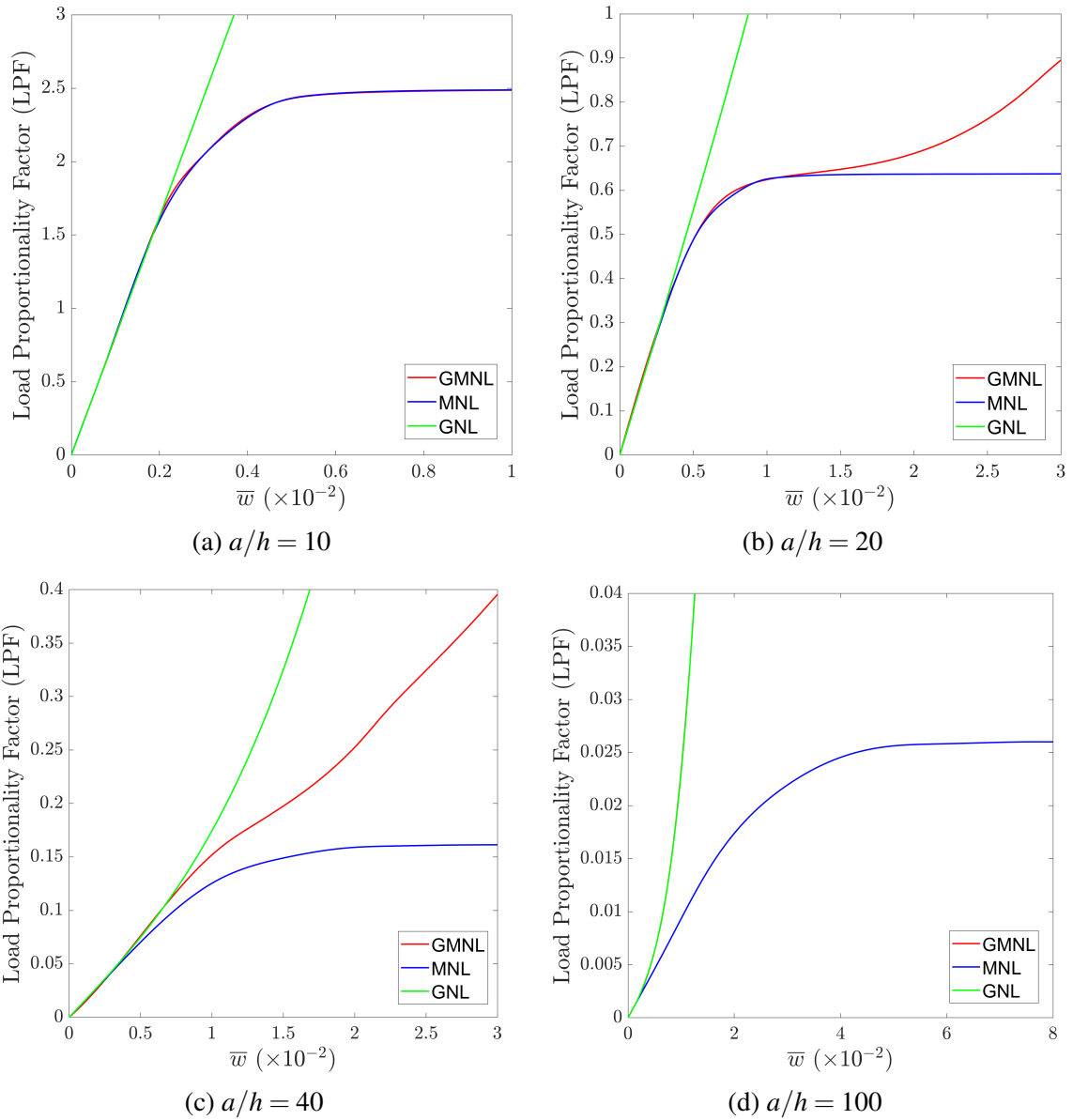
Source: The author.

Figure 28 – Load-displacement curve for a FG square plate.

(a) $a/h = 100$.

(b) $a/h = 40$.
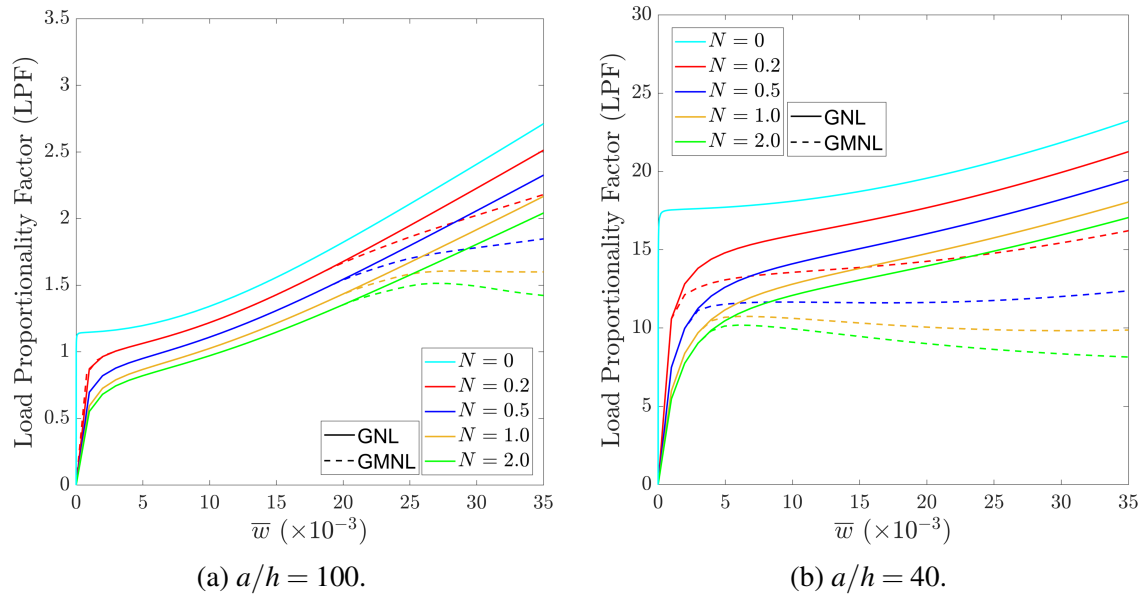
6   CONCLUSION

This work introduced a methodology for the material and geometric nonlinear analysis of Functionally Graded structures, particularly focusing on plates. It presented a general 3D formulation capable of handling tridirectional gradation, incorporating algorithms for both material and geometric nonlinearities, and considering isogeometric and finite elements approaches. Furthermore, a novel NURBS-based 7-DoF Quasi-3D (Q3D7) formulation was developed using the degenerated solid approach. Multiple kinematic theories derived from the specialization of the Q3D7 were also explored. The accuracy of the proposed formulations was assessed through several types of analyses involving different geometries and materials.

The mathematical developments were implemented in an in-house software named Finite Element Analysis Tool (FAST), developed in C++. The implementation covered the von Mises and Tamura-Tomota-Ozawa plasticity models, the Quasi-3D formulations with von Karman strains, and the shape function gradations for both Finite Element Methods and Isogeometric Analysis approaches.

For the general 3D formulation, the results exhibited a close agreement with literature examples for both homogeneous and FG materials. The plasticity algorithms were validated through comparison with reference solutions available in the literature.

Additionally, concerning the Quasi-3D kinematic theories, the Q3D7 formulation presented an excellent agreement with reference solutions and 3D benchmarks for displacements, ultimate loads and buckling behavior. The degenerated solid approach allowed the seamless integration of 3D plasticity algorithms into the formulation. In contrast, the 6-DoF Quasi-3D theory (Q3D6) presented Poisson locking, making it unsuitable for structural analysis in general.

Regarding the assessment of the behavior of FG plates, the micromechanical model choice was found to be substantial to the analysis results, depending on the mechanical properties of constituents and gradation profile. Furthermore, the inclusion of both nonlinearities into the analysis was essential to accurately define the equilibrium-path, particularly for intermediate values of length-to-thickness ratios, as it could significantly alter the nonlinear load-displacement curve behavior. It is important to remark that, in thick plates, structural failure was primarily influenced by material nonlinearity caused by bending effects, while in thin plates, geometric nonlinearity played a predominant role due to membrane effects.

Overall, the 7-DoF Quasi-3D theory demonstrated excellent agreement with benchmarks and reference values. It offered significant advantages over the solid model, requiring a

simpler mesh and facilitating the enforcement of boundary conditions and applied loads. Additionally, it also presented advantages over other plate kinematic theories by correctly employing 3D plasticity algorithms and eliminating the Poisson locking observed in the Q3D6.

In conclusion, the use of the Q3D7 is generally recommended over the 3D model for analysis of FG plates due to the close agreement in results and less complex methodology. However, for analyses where material nonlinearity is not required, simpler plate theories may be preferable over the Q3D7, following the same reasoning.

The following suggestions can be further explored in future works:

(a) Employment of alternatives plasticity models for Functionally Graded Materials;

(b) Use of other functions to define both the transverse shear strains and thickness stretching, adopting the same general formulation;

(c) Adjustment of plasticity algorithms to be employed in reduced stress states, capable of being used with simpler plate theories;

(d) Development of other benchmarks problems using the general 3D formulation to model bidirectional and tridirectional graded structures;

(e) Study of other types of Functionally Graded Materials besides the MMC, such as the Carbon-Nanotube Reinforced and Porous FGM.

BIBLIOGRAPHY

1 REDDY, J. N. *Mechanics of laminated composite plates and shells: theory and analysis*. [S.l.]: CRC Press, 2004.

2 BARBERO, E. J. *Introduction to Composite Materials Design*. Philadelphia, PA: Taylor & Francis, 1999. ISBN 9781560327028.

3 ILCEWICZ, L.; HOFFMAN, D.; FAWCETT, A. Composite applications in commercial airframe structures. *Comprehensive Composite Materials*, p. 87–119, 2000.

4 LEVY NETO, F.; PARDINI, L. C. *Compósitos Estruturais*. [S.l.]: BLUCHER, 2016.

5 SHEN, H.-S. *Functionally Graded Materials*. [S.l.]: CRC Press, 2016. ISBN 9781420092578.

6 EL-WAZERY, A. P. D. M. S.; EL-DESOUKY, A. A review on functionally graded ceramic-metal materials. *Journal of Materials and Environmental Science*, v. 6, p. 1369–1376, 01 2015.

7 KOIZUMI, M. Fgm activities in japan. *Composites Part B*, p. 1–4, 1997.

8 JHA, D.; KANT, T.; SINGH, R. A critical review of recent research on functionally graded plates. *Composite Structures*, v. 96, p. 833–849, 2013.

9 NAEBE, M.; SHIRVANIMOGHADDAM, K. Functionally graded materials: A review of fabrication and properties. *Applied Materials Today*, v. 5, p. 223–245, 2016.

10 UDUPA, G.; RAO, S. S.; GANGADHARAN, K. Functionally graded composite materials: An overview. *Procedia Materials Science*, v. 5, p. 1291–1299, 2014.

11 AKGOZ, B.; CIVALEK, O. Longitudinal vibration analysis of strain gradient bars made of functionally graded materials (fgm). *Composites Part B: Engineering*, v. 55, p. 263–268, 2013.

12 MURíN, J.; AMIMBAGHAI, M.; HRABOVSKý, J. Elastostatic aanalysis of the spatial fgm structures. *Journal of Mechanical Engineering*, v. 65, p. 27–56, 2015.

13 MEDEIROS, M. S.; RIBEIRO, L. G. Micromechanical elastoplastic limit analysis of in-plane bending of functionally graded pipe elbows. *Thin-Walled Structures*, v. 171, p. 108778, 2022. ISSN 0263-8231.

14 AKBARZADEH, A. H.; ABEDINI, A.; CHEN, Z. T. Effect of micromechanical models on structural responses of functionally graded plates. *Composite Structures*, v. 119, p. 598–609, 2015.

15 ZUIKER, J. R. Functionally graded materials: Choice of micromechanics model and limitations in property variation. *Composites Engineering*, v. 5, n. 7, p. 807–819, 1995. ISSN 0961-9526. Use of Composites in Multi-Phased and Functionally Graded Materials.

16 BARROS, R. M.; PARENTE, E.; MEDEIROS, M. S. Stability analysis of functionally graded plates considering different micromechanical models. *Journal of the Brazilian Society of Mechanical Sciences and Engineering*, Springer Science and Business Media LLC, v. 45, n. 10, set. 2023. ISSN 1806-3691.

17   KUMAR, L.; HARSHA, S. P. Effect of carbon nanotubes on cnt reinforced fgm nano plate under thermo mechanical loading. *Procedia Technology*, v. 23, p. 130–137, 2016.

18   HUSSAIN, M.; NAEEM, M. N. Vibration characteristics of zigzag fgm single-walled carbon nanotubes based on ritz method with ring-stiffeners. *Indian Journal of Physics*, v. 23, p. 130–137, 2020.

19   S, N. K. H.; KATTIMANI, S.; NGUYEN-THOI, T. Influence of porosity distribution on nonlinear free vibration and transient responses of porous functionally graded skew plates. *Defence Technology*, Elsevier BV, v. 17, n. 6, p. 1918–1935, dez. 2021. ISSN 2214-9147.

20   FOUAIDI, M.; JAMAL, M.; BELOUAGGADIA, N. Nonlinear bending analysis of functionally graded porous beams using the multiquadric radial basis functions and a taylor series-based continuation procedure. *Composite Structures*, Elsevier BV, v. 252, p. 112593, nov. 2020. ISSN 0263-8223.

21   HUGHES, T. J. R.; COTRELL, J. A.; BAZILEVS, Y. Isogeometric analysis: Cad, finite elements, nurbs, exact geometry and mesh refinement. *Computer Methods in Applied Mechanics and Engineering*, v. 194, p. 4135–4195, 2005.

22   PIEGL, L.; TILLER, W. *The NURBS Book*. 2. ed. Berlin, Germany: Springer, 1996. (Monographs in Visual Communication).

23   BARROSO, E. S. *Análise e otimização de estruturas laminadas utilizando a formulação isogeométrica*. 2015. 156 f. Dissertação (Mestrado) — Universidade Federal do Ceará, Fortaleza, 2015.

24   BATENI, M.; KIANI, Y.; ESLAMI, M. A comprehensive study on stability of fgm plates. *International Journal of Mechanical Sciences*, Elsevier BV, v. 75, p. 134–144, out. 2013. ISSN 0020-7403.

25   ZANJANCHI, M.; GHADIRI, M.; SABOURI-GHOMI, S. Dynamic stability and bifurcation point analysis of fg porous core sandwich plate reinforced with graphene platelet. *Acta Mechanica*, Springer Science and Business Media LLC, v. 234, n. 10, p. 5015–5037, jul. 2023. ISSN 1619-6937.

26   MARS, J. et al. Numerical analysis of geometrically non-linear behavior of functionally graded shells. *Latin American Journal of Solids and Structures*, FapUNIFESP (SciELO), v. 14, n. 11, p. 1952–1978, 2017. ISSN 1679-7817.

27   XUE, L. J. et al. Elastoplastic analysis of a functionally graded material beam subjected to uniformly distributed load. *Journal of Mechanics*, Cambridge University Press, v. 36, n. 1, p. 73–85, 2020.

28   NIKBAKHT, S.; SALAMI, S. J.; SHAKERI, M. Three dimensional analysis of functionally graded plates up to yielding, using full layer-wise finite element method. *Composite Structures*, Elsevier BV, v. 182, p. 99–115, dez. 2017. ISSN 0263-8223.

29   WANG, C. M.; REDDY, J. N.; LEE, K. H. *Shear Deformable Beams and Plates: Relationships with Classical Solutions*. [S.l.]: Elsevier Science Ltd., 2000.

30   MINDLIN, R. D. Influence of rotatory inertia and shear on flexural motions of isotropic, elastic plates. *Journal of Applied Mechanics*, ASME International, v. 18, n. 1, p. 31–38, mar. 1951. ISSN 1528-9036.

31   MOITA, J. S. et al. Material and geometric nonlinear analysis of functionally graded plate-shell type structures. *Applied Composite Materials*, Springer Science and Business Media LLC, v. 23, n. 4, p. 537–554, mar. 2016. ISSN 1573-4897.

32   SHARMA, K.; KUMAR, D. Elastoplastic stability and failure analysis of fgm plate with temperature dependent material properties under thermomechanical loading. *Latin American Journal of Solids and Structures*, FapUNIFESP (SciELO), v. 14, n. 7, p. 1361–1386, ago. 2017. ISSN 1679-7825.

33   REDDY, J. N. A general nonlinear third-order theory of functionally graded plates. *International Journal of Aerospace and Lightweight Structures (IJALS) -*, Research Publishing Services, v. 01, n. 01, p. 01, 2011. ISSN 2010-4286.

34   MOITA, J. et al. Higher-order finite element models for the static linear and nonlinear behaviour of functionally graded material plate-shell structures. *Composite Structures*, Elsevier BV, v. 212, p. 465–475, mar. 2019.

35   ZENKOUR, A. M.; ALJADANI, M. H. Buckling response of functionally graded porous plates due to a quasi-3d refined theory. *Mathematics*, MDPI AG, v. 10, n. 4, p. 565, fev. 2022. ISSN 2227-7390.

36   ZAOUI, F. Z.; OUINAS, D.; TOUNSI, A. New 2d and quasi-3d shear deformation theories for free vibration of functionally graded plates on elastic foundations. *Composites Part B: Engineering*, v. 159, p. 231–247, 2019. ISSN 1359-8368.

37   NEVES, A. et al. A quasi-3d hyperbolic shear deformation theory for the static and free vibration analysis of functionally graded plates. *Composite Structures*, v. 94, n. 5, p. 1814–1825, 2012. ISSN 0263-8223.

38   CARRERA, E. et al. Effects of thickness stretching in functionally graded plates and shells. *Composites Part B: Engineering*, v. 42, n. 2, p. 123–133, 2011. ISSN 1359-8368.

39   SHINOHARA, Y. Functionally graded materials. Elsevier, p. 1179–1187, 2013.

40   SHIOTA, I.; MIYAMOTO, Y. (Ed.). *Functionally Graded Materials 1996*. Amsterdam: Elsevier Science B.V., 1997. ISBN 978-0-444-82548-3.

41   TRAN, L. V.; FERREIRA, A. J. M.; NGUYEN-XUAN, H. Isogeometric analysis of functionally graded plates using higher-order shear deformation theory. *Composites: Part B*, v. 51, p. 368–383, 2013.

42   PRACIANO, J. S. C. *Análise da Estabilidade de Estruturas Laminadas e de Materiais com Gradação Funcional utilizando uma Formulação Isogeométrica*. 2018. 101 f. Dissertação (Mestrado) — Universidade Federal do Ceará, Fortaleza, 2018.

43   RIBEIRO, L. G. et al. Surrogate based optimization of functionally graded plates using radial basis functions. *Composite Structures*, v. 252, 2020.

44   RIBEIRO, L. G. *Efficient optimization of composite structures using multi-fidelity models*. 2022. 219 f. Dissertação (Mestrado) — Universidade Federal do Ceará, Fortaleza, 2022.

45   REUSS, A. Berechnung der fließgrenze von mischkristallen auf grund der plastizitätsbedingung für einkristalle. *Zeitschrift Für Angewandte Mathematik Und Mechanik*, p. 49 – 58, 1929.

46   VOIGT, W. Ueber die beziehung zwischen den beiden elasticitätsconstanten isotroper körper. *Annalen Der Physik*, p. 573 – 587, 1889.

47   MEDEIROS JR., M. S.; PARENTE JR., E.; MELO, A. M. C. Influence of the micromechanics models and volume fraction distribution on the overall behavior of sic/al functionally graded pressurized cylinders. *Latin American Journal of Solids and Structures*, v. 16, n. 4, 2019.

48   GROSS, D.; SEELIG, T. *Fracture mechanics*. 2. ed. Berlin, Germany: Springer, 2011. (Mechanical Engineering Series).

49   MISHNAEVSKY, L. L. *Computational mesomechanics of composites*. New York: Wiley-Interscience, 2007.

50   MORI, T.; TANAKA, K. Average stress in matrix and average elastic energy of materials with misfitting inclusions. *Acta Metallurgica*, p. 571 – 574, 1973.

51   REITER, T.; DVORAK, G. J.; TVERGAARD, V. Micromechanical models for graded composite materials. *Journal of the Mechanics and Physics of Solids*, v. 45, n. 8, p. 1281–1302, 1997. ISSN 0022-5096.

52   REITER, T.; DVORAK, G. J. Micromechanical models for graded composite materials : ii. thermomechanical loading. *Journal of the Mechanics and Physics of Solids*, v. 46, n. 9, p. 1655–1673, 1998. ISSN 0022-5096.

53   CHRISTENSEN, R.; LO, K. Solutions for effective shear properties in three phase sphere and cylinder models. *Journal of the Mechanics and Physics of Solids*, v. 27, n. 4, p. 315–330, 1979. ISSN 0022-5096.

54   CHRISTENSEN, R. M. A critical evaluation for a class of micro-mechanics models. *Journal of the Mechanics and Physics of Solids*, v. 38, n. 3, p. 379–404, 1990. ISSN 0022-5096.

55   SOROUR, S. S.; SHAZLY, M.; MEGAHED, M. M. Limit load analysis of thin-walled as-fabricated pipe bends with low ovality under in-plane moment loading and internal pressure. *Thin-Walled Structures*, v. 144, p. 106336, 2019. ISSN 0263-8231.

56   TAMURA, I. Strength and ductility of fe-ni-c alloys composed of austenite and martensite with various strength. *Proceedings of the third international conference on strength of metals and alloys*, Cambridge, Institute of Metals, v. 1, p. 611–615, 1973.

57   JRAD, H. et al. Geometrically nonlinear analysis of elastoplastic behavior of functionally graded shells. *Engineering with Computers*, Springer Science and Business Media LLC, v. 35, n. 3, p. 833–847, ago. 2018. ISSN 1435-5663.

58   JIN, Z.-H.; PAULINO, G. H.; DODDS, R. H. Cohesive fracture modeling of elastic–plastic crack growth in functionally graded materials. *Engineering Fracture Mechanics*, Elsevier BV, v. 70, n. 14, p. 1885–1912, set. 2003. ISSN 0013-7944.

59   NETO, E. A. de S.; PERIC, D.; OWEN, D. R. J. *Computational methods for plasticity*. Hoboken, NJ: Wiley-Blackwell, 2008.

60   SIMO, J. C.; HUGHES, T. J. R. *Computational Inelasticity*. 1. ed. New York, NY: Springer, 2000. (Interdisciplinary Applied Mathematics).

61 NAYAK, P.; BHOWMICK, S.; SAHA, K. N. Elasto-plastic analysis of thermo-mechanically loaded functionally graded disks by an iterative variational method. *Engineering Science and Technology, an International Journal*, Elsevier BV, v. 23, n. 1, p. 42–64, fev. 2020. ISSN 2215-0986.

62 KIM, J. H.; PAULINO, G. H. Isoparametric graded finite elements for nonhomogeneous isotropic and orthotropic materials. *Journal of Applied Mechanics*, v. 69, n. 4, p. 502–514, 2002.

63 KIM, J. H.; PAULINO, G. H. The weak patch test for nonhomogeneous materials modeled with graded finite elements. *Journal of the Brazilian Society of Mechanical Sciences and Engineering*, v. 29, p. 63–81, 2007.

64 DE BORST, R. et al. *Non-Linear Finite Element Analysis of Solids and Structures*. [S.l.]: Wiley, 2012. ISBN 9781118375938.

65 BATHE, K.-J. *Finite Element Procedures*. [S.l.]: Klaus-Jürgen Bathe, 2008.

66 PARENTE JR., E.; DE HOLANDA, A. S.; SILVA, S. M. B. A. d. Tracing nonlinear equilibrium paths of structures subjected to thermal loading. *Computational Mechanics*, Springer Science and Business Media LLC, v. 38, n. 6, p. 505–520, 2005. ISSN 1432-0924.

67 BATOZ, J.; DHATT, G. Incremental displacement algorithms for nonlinear problems. *International Journal for Numerical Methods in Engineering*, Wiley, v. 14, n. 8, p. 1262–1267, jan. 1979. ISSN 1097-0207.

68 RIKS, E. An incremental approach to the solution of snapping and buckling problems. *International Journal of Solids and Structures*, v. 15, n. 7, p. 529–551, 1979. ISSN 0020-7683.

69 RAMM, E. Strategies for tracing the nonlinear response near limit points. In: *Nonlinear Finite Element Analysis in Structural Mechanics*. Berlin, Heidelberg: Springer Berlin Heidelberg, 1981. p. 63–89. ISBN 978-3-642-81589-8.

70 COOK, R. D. et al. *Concepts and applications of finite element analysis*. 4. ed. Nashville, TN: John Wiley & Sons, 2001.

71 SIMO, J. C.; KENNEDY, J. G.; GOVINDJEE, S. Non-smooth multisurface plasticity and viscoplasticity. loading/unloading conditions and numerical algorithms. *International Journal for Numerical Methods in Engineering*, v. 26, p. 2161–2185, 1988.

72 BORDEN, M. J. et al. Isogeometric finite element data structures based on bézier extraction of nurbs. *International Journal for Numerical Methods in Engineering*, Wiley, v. 87, n. 1–5, p. 15–47, ago. 2010. ISSN 1097-0207.

73 FARIN, G. (Ed.). *Curves and Surfaces for CAGD (Fifth Edition)*. Fifth edition. San Francisco: Morgan Kaufmann, 2002. (The Morgan Kaufmann Series in Computer Graphics). ISBN 978-1-55860-737-8.

74 REDDY, J. A refined nonlinear theory of plates with transverse shear deformation. *International Journal of Solids and Structures*, Elsevier BV, v. 20, n. 9–10, p. 881–896, 1984. ISSN 0020-7683.

75 TOURATIER, M. An efficient standard plate theory. *International Journal of Engineering Science*, Elsevier BV, v. 29, n. 8, p. 901–916, jan. 1991. ISSN 0020-7225.

76   SOLDATOS, K. P. A transverse shear deformation theory for homogeneous monoclinic plates. *Acta Mechanica*, Springer Science and Business Media LLC, v. 94, n. 3–4, p. 195–220, set. 1992. ISSN 1619-6937.

77   MANTARI, J.; OKTEM, A.; SOARES, C. G. Static and dynamic analysis of laminated composite and sandwich plates and shells by using a new higher-order shear deformation theory. *Composite Structures*, Elsevier BV, v. 94, n. 1, p. 37–49, dez. 2011. ISSN 0263-8223.

78   NEVES, A. et al. A quasi-3d sinusoidal shear deformation theory for the static and free vibration analysis of functionally graded plates. *Composites Part B: Engineering*, Elsevier BV, v. 43, n. 2, p. 711–725, mar. 2012. ISSN 1359-8368.

79   SI, J.; YI, S. A quasi-3d model of composite laminated micro plate based on new modified couple stress theory under thermal loading. *Mechanics of Advanced Materials and Structures*, Informa UK Limited, p. 1–12, jan. 2023. ISSN 1537-6532.

80   BISCHOFF, M.; RAMM, E. Shear deformable shell elements for large strains and rotations. *International Journal for Numerical Methods in Engineering*, v. 40, n. 23, p. 4427–4449, 1997.

81   PAYETTE, G.; REDDY, J. A seven-parameter spectral/hp finite element formulation for isotropic, laminated composite and functionally graded shell structures. *Computer Methods in Applied Mechanics and Engineering*, v. 278, p. 664–704, 2014. ISSN 0045-7825.

82   THAI, C. H. et al. Isogeometric analysis of laminated composite and sandwich plates using a new inverse trigonometric shear deformation theory. *European Journal of Mechanics, A/Solids*, Elsevier Ltd, v. 43, p. 89–108, 2014.

83   AYDOGDU, M. Conditions for functionally graded plates to remain flat under in-plane loads by classical plate theory. *Composite Structures*, Elsevier BV, v. 82, n. 1, p. 155–157, jan. 2008. ISSN 0263-8223.

84   SHEN, H.-S. *Postbuckling behavior of plates and shells*. Singapore, Singapore: World Scientific Publishing, 2017.

85   RIBEIRO, L. G.; PARENTE, E.; MELO, A. M. C. de. Alternative variable-fidelity acquisition functions for efficient global optimization of black-box functions. *Structural and Multidisciplinary Optimization*, Springer Science and Business Media LLC, v. 66, n. 7, jun. 2023. ISSN 1615-1488.

86   MATTIASSON, K. Numerical results from large deflection beam and frame problems analyzed by means of elliptic integrals. *International Journal for Numerical Methods in Engineering*, v. 17, p. 145 – 153, 1981.

87   HILL, R. *The mathematical theory of plasticity*. London, England: Oxford University Press, 1950. (Engineering Science S.).

88   GAUTSCHI, W.; LI, S. Gauss—radau and gauss—lobatto quadratures with double end points. *Journal of Computational and Applied Mathematics*, v. 34, n. 3, p. 343–360, 1991. ISSN 0377-0427.

89   SKRZYPEK, J.; HETNARSKI, R. B. *Plasticity And Creep*. Boca Raton, FL: CRC Press, 1993.

90   GUNES, R. et al. The elasto-plastic impact analysis of functionally graded circular plates under low-velocities. *Composite Structures*, Elsevier BV, v. 93, n. 2, p. 860–869, jan. 2011. ISSN 0263-8223.

91   CHAWLA, N. et al. Cyclic stress-strain behavior of particle reinforced metal matrix composites. *Scripta Materialia*, Elsevier BV, v. 38, n. 10, p. 1595–1600, abr. 1998. ISSN 1359-6462.

92   ESHELBY, J. D. The determination of the elastic field of an ellipsoidal inclusion, and related problems. The Royal Society, v. 241, n. 1226, p. 376–396, ago. 1957.

APPENDIX A – NURBS BASIS FUNCTIONS

Geometric modeling is an applied mathematical theory used to represent and describe geometric shapes. It plays a crucial role in computer graphics and is extensively employed by Computer Aided Design (CAD) based softwares. These softwares' applications are utilized in various industries, ranging from electronic games to diverse engineering fields.

The mathematical framework used by CAD systems, emphasizing the modeling of free-form curves, surfaces and solids, is frequently presented in recent literature as Bézier, B-Splines, Non-Uniform Rational B-Splines and T-Splines representations. These representations not only enable the modeling of complex geometries, but also account for holes and trimmed surfaces.

In engineering applications, CAD systems are frequently used in conjunction to Computer Aided Engineering (CAE) systems, resulting in an integrated performance between geometric modeling and numerical analysis.

In this appendix, since this work employed NURBS-based formulation, the basis functions provided by this geometric representation are presented, and some of their notable properties and features are defined. Anyhow, if needed, more in-depth discussions and concepts can be found within the literature[22, 23].

A.1 B-Splines

B-Splines are a type of curve description in a parametric space known for their capacity to describe distinct segments within a single parametric representation. This is achieved by narrowing the influence of their basis functions over specific regions of the parametric space, defined as knot-vectors. A B-Spline curve is defined by associating the basis functions $N_{i,p}(\xi)$ with the control points $\mathbf{p}_i$:

$$C(\xi) = \sum_{i=1}^{n} N_{i,p}(\xi)\,\mathbf{p}_i \tag{A.1}$$

where n is the number of control points and p denotes the curve degree.

B-Splines basis functions require the use of a knot-vector, which is a set of non-negative, non-decreasing parametric values along the range $[\xi_1, \xi_{n+p+1}]$ where the curve is defined. These basis functions can be computed using the Cox-de Boor recursion formula. Given

a knot vector $\Xi = \left[\xi_1, \xi_2, ..., \xi_{n+p+1} \right]$, the B-spline basis functions are expressed as[22]:

$$N_{i,0}(\xi) = \begin{cases} 1, & \text{if } \xi_i \leq \xi < \xi_{i+1} \\ \\ 0, & \text{otherwise} \end{cases} \tag{A.2}$$

$$N_{i,p}(\xi) = \frac{\xi - \xi_i}{\xi_{i+p} - \xi_i} N_{i,p-1}(\xi) + \frac{\xi_{i+p+1} - \xi}{\xi_{i+p+1} - \xi_{i+1}} N_{i+1,p-1}(\xi) \tag{A.3}$$

A knot-vector is labeled as uniform if its parameters vary based on a constant factor, otherwise it is said to be non-uniform. For instance, $\Xi = [0,0,0,0.33,0.67,1,1,1]$ is uniform, whereas the vector $\Xi = [0,0,0,0.4,0.75,1,1,1]$ is non-uniform. The size of a knot vector directly impacts on the number of basis functions[22]:

$$n = ks - p - 1 \tag{A.4}$$

where n is the number of basis functions and ks is the size of the knot vector.

Furthermore, it is essential to emphasize other features and properties of B-splines basis functions, as these attributes are proven to be valuable in subsequent process of structural analysis[22]:

– Compact support: $N_{i,p} = 0$ if ξ is outside of the interval $\left[\xi_i, \xi_{i+p+1} \right]$;
– Partition of unity: $\sum\limits_{i=1}^{n} N_{i,p}(\xi) = 1$;
– Non-negative functions: $N_{i,p} \geq 0$;
– Each *knot span* $\left[\xi_j, \xi_{j+1} \right]$ carries exactly $p+1$ non-negative basis functions;
– Every $N_{i,p}$ derivative exist within the knot spans. For each knot, the basis function can be differentiated $p - m$ times, given that m is the knot multiplicity.

The Isogeometric analysis allows three distinct B-spline curve refinement algorithms: the h, p and k schemes. In the h refinement approach, the knot span size is reduced by introducing new knots into the knot vector. This increases the number of existing spans and results in the creation of a new basis function and an associated control point. It resembles the h refinement method in FEM, where the number of elements is increased while their size is reduced.

The p refinement consists in elevating the curve degree. During this process, the multiplicity of every knot is increased by one, which maintains the continuity. This scheme does not alter the number of knot spans, but, in order to preserve the multiplicity, it leads to the addition of a new basis function and an associated control point. This approach is similar to the p refinement in FEM, where the degree associated with polynomial basis functions is increased.

The third refinement algorithm in the IGA is the *k* refinement. Unlike both methods previously discussed, there is not a similar procedure presented for FEM, being exclusive to this computational approach. The *k* refinement combines aspects of both the *p* and *h* refinements respectively. Consequently, it results in basis functions with an increased degree, a greater number of knot spans and also a higher continuity between these spans. This feature is particularly valuable for isogeometric elements that require functions of higher continuity than the usual C^0. This is the reason that makes IGA a more suitable computational method for the development and implementation of C^1 kinematic theories, as presented in this work.

A.2 NURBS

NURBS stands for Non Uniform Rational B-Splines[22]. They are widely employed by commercial softwares for geometric modelling. Their high popularity is attributed to their rational basis functions, which allow for the exact representation of non-polynomial geometries, including shapes like ellipses and circumferences. Besides this upfront advantage, NURBS curves present multiple other valuable properties, among which are:

(a) The capability to achieve a wide range of geometries by manipulating the control points and the weights associated with them;

(b) Speed and stability during their numerical evaluation;

(c) The ability to apply conventional geometric transformations, such as rotation and translation;

(d) The capacity to represent other simpler design curves, such as B-Splines and Bézier elements.

These attributes make NURBS a versatile tool in the field of geometric modeling.

The rational basis functions are obtained by dividing one polynomial by another. Furthermore, weight values are associated with each control point to provide a parameter that better controls the curve's behavior. This behavior is mathematically described by:

$$R_{i,p}(\xi) = \frac{N_{i,p}(\xi)w_i}{\sum_{i=1}^{n} N_{i,p}(\xi)w_i} = \frac{N_{i,p}(\xi)w_i}{W(\xi)} = \frac{A(\xi)}{W(\xi)} \tag{A.5}$$

where $R_{i,p}$ is the rational basis, $N_{i,p}$ stands for the polynomial basis and $w_i(\xi)$ denotes the weight functions of each control point, and ξ is the parametric coordinate. Therefore, in order to construct a NURBS curve, the basis functions are required to be paired to the curve control

points (P_i):

$$C(\xi) = \sum_{i=1}^{n} R_{i,p}(\xi) \mathbf{P}_i \tag{A.6}$$

These curves can also be refined using the three techniques previously defined for B-Splines, as discussed in Section A.1.

Additionally, due to the mechanical formulation requirements, obtaining the derivatives of NURBS functions is essential. The first-degree derivative can be easily computed using the quotient rule:

$$R'_{i,p}(\xi) = \frac{W(\xi)A'(\xi) - W'(\xi)A(\xi)}{W(\xi)^2} = \frac{A'(\xi) - W'(\xi)R_{i,p}(\xi)}{W(\xi)} \tag{A.7}$$

For higher degree derivatives, the Leibnitz technique is employed, where the k-th derivative is given by:

$$R_{i,p}^{(k)}(\xi) = \frac{A^{(k)}(\xi) - \sum_{j=1}^{k} \binom{k}{j} W^{(j)}(\xi) R_{i,p}^{(k-j)}(\xi)}{W(\xi)} \tag{A.8}$$

This work aims for the analysis of 3D and 2D models, requiring the combination of multiple NURBS curves to model geometries in higher space dimensions. A NURBS surface is the result of a tensor product between two univariate NURBS curves, as illustrated in Figure 29. Assuming a degree p curve along the (ξ) direction with a knot vector $\Xi = \left[\xi_1, \xi_2, ..., \xi_{n+p+1}\right]$, another degree q curve in the direction (η) with a knot vector $H = \left[\eta_1, \eta_2, ..., \eta_{m+q+1}\right]$ and a control point matrix $\mathbf{P}(n \times m)$, the NURBS surface is expressed as:

$$\mathbf{S}(\xi, \eta) = \sum_{i=1}^{n} \sum_{j=1}^{m} R_{ij}(\xi, \eta) \mathbf{P}_{ij} \tag{A.9}$$

where R_{ij} is given by:

$$R_{ij}(\xi, \eta) = \frac{w_{ij}N_{i,p}(\xi)N_{j,q}(\eta)}{W(\xi, \eta)} = \frac{\mathbf{A}(\xi, \eta)}{W(\xi, \eta)} \tag{A.10}$$

and $W(\xi, \eta)$ is the bivariate weight function:

$$W(\xi, \eta) = \sum_{\hat{i}=1}^{n} \sum_{\hat{j}=1}^{m} w_{\hat{i}\hat{j}}N_{\hat{i},p}(\xi)N_{\hat{j},q}(\eta) \tag{A.11}$$

As the surfaces are now defined by two parameters, each representing a parametric direction, it is necessary to evaluate the partial derivatives. Considering the weight functions,
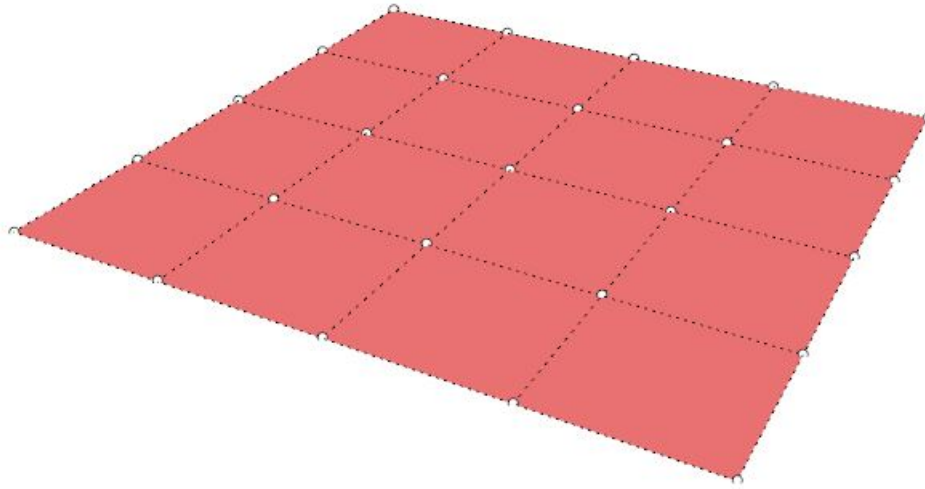
they are calculated by:

$$\frac{\partial}{\partial \xi} W(\xi, \eta) = \sum_{\hat{i}=1}^{n} \sum_{\hat{j}=1}^{m} w_{\hat{i}\hat{j}} N'_{\hat{i},p}(\xi) N_{\hat{j},q}(\eta)$$

$$\frac{\partial}{\partial \eta} W(\xi, \eta) = \sum_{\hat{i}=1}^{n} \sum_{\hat{j}=1}^{m} w_{\hat{i}\hat{j}} N_{\hat{i},p}(\xi) N'_{\hat{j},q}(\eta)$$

(A.12)

Next, the partial derivatives for the NURBS surface are evaluated by:

$$\frac{\partial}{\partial \xi} R_{ij}(\xi, \eta) = w_{ij} \frac{W(\xi, \eta) N'_{i,p}(\xi) N_{j,q}(\eta) - \frac{\partial}{\partial \xi} W(\xi, \eta) N_{i,p}(\xi) N_{j,q}(\eta)}{W^2(\xi, \eta)}$$

$$\frac{\partial}{\partial \eta} R_{ij}(\xi, \eta) = w_{ij} \frac{W(\xi, \eta) N_{i,p}(\xi) N'_{j,q}(\eta) - \frac{\partial}{\partial \eta} W(\xi, \eta) N_{i,p}(\xi) N_{j,q}(\eta)}{W^2(\xi, \eta)}$$

(A.13)

Figure 29 – NURBS surface.

For a NURBS solid, which represents a 3D model, the equations are analogous to those presented for the two-dimensional structures. The main difference is that, for this instance, a tensor product is employed for three univariate NURBS basis functions, as shown in Figure 30. Given a degree p curve along the (ξ) direction with a knot vector $\Xi = \left[\xi_1, \xi_2, ..., \xi_{n+p+1}\right]$, a degree q curve in the direction (η) with a knot vector $H = \left[\eta_1, \eta_2, ..., \eta_{m+q+1}\right]$, a degree l curve in the direction (ζ) with a knot vector $Z = [\zeta_1, \zeta_2, ..., \zeta_{o+l+1}]$ and a control point matrix $\mathbf{P}(n \times m \times o)$, the NURBS solid is given by:

$$\mathbf{V}(\xi, \eta, \zeta) = \sum_{i=1}^{n} \sum_{j=1}^{m} \sum_{k=1}^{o} R_{ijk}(\xi, \eta, \zeta) \mathbf{P}_{ijk}$$
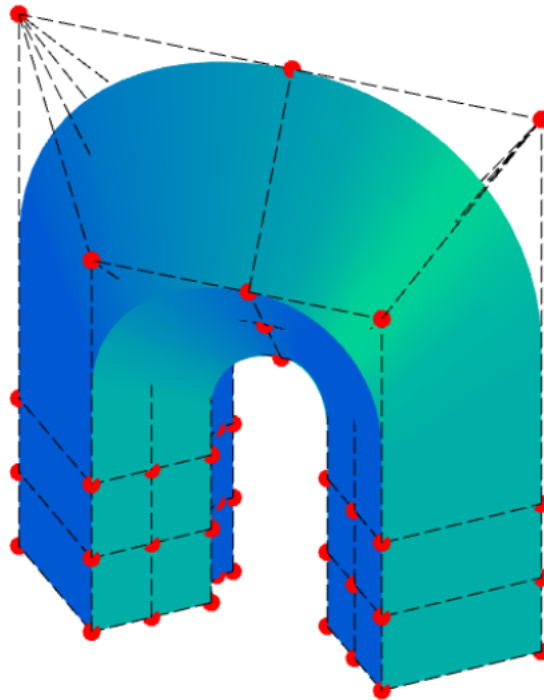
(A.14)

where R_{ijk} is defined as:

$$R_{ijk}(\xi,\eta,\zeta) = \frac{w_{ij}N_{i,p}(\xi)N_{j,q}(\eta)N_{k,l}(\zeta)}{W(\xi,\eta,\zeta)} = \frac{\mathbf{A}(\xi,\eta,\zeta)}{W(\xi,\eta,\zeta)} \qquad \text{(A.15)}$$

and $W(\xi,\eta,\zeta)$ is the trivariate weight function:

$$W(\xi,\eta,\zeta) = \sum_{\hat{i}=1}^{n}\sum_{\hat{j}=1}^{m}\sum_{\hat{k}=1}^{o} w_{\hat{i}\hat{j}\hat{k}}N_{\hat{i},p}(\xi)N_{\hat{j},q}(\eta)N_{\hat{k},l}(\zeta) \qquad \text{(A.16)}$$

This approach allows for the modeling of surfaces in higher dimensions, a crucial feature for the analysis conducted in this work.

Figure 30 – NURBS solid.

Source: Barroso[23].

The methodology for obtaining partial derivatives in 3D models follows the same approach as presented for 2D models. Beginning with the weight functions, they are calculated as follows:

$$\frac{\partial}{\partial \xi}W(\xi,\eta,\zeta) = \sum_{\hat{i}=1}^{n}\sum_{\hat{j}=1}^{m}\sum_{\hat{k}=1}^{o} w_{\hat{i}\hat{j}\hat{k}}N'_{\hat{i},p}(\xi)N_{\hat{j},q}(\eta)N_{\hat{k},l}(\zeta)$$

$$\frac{\partial}{\partial \eta}W(\xi,\eta,\zeta) = \sum_{\hat{i}=1}^{n}\sum_{\hat{j}=1}^{m}\sum_{\hat{k}=1}^{o} w_{\hat{i}\hat{j}\hat{k}}N_{\hat{i},p}(\xi)N'_{\hat{j},q}(\eta)N_{\hat{k},l}(\zeta) \qquad \text{(A.17)}$$

$$\frac{\partial}{\partial \zeta}W(\xi,\eta,\zeta) = \sum_{\hat{i}=1}^{n}\sum_{\hat{j}=1}^{m}\sum_{\hat{k}=1}^{o} w_{\hat{i}\hat{j}\hat{k}}N_{\hat{i},p}(\xi)N_{\hat{j},q}(\eta)N'_{\hat{k},l}(\zeta)$$

Then, the partial derivatives for the NURBS solid are evaluated by:

$$
\begin{aligned}
\frac{\partial}{\partial \xi} R_{ijk}(\xi, \eta, \zeta) &= w_{ijk} N_{j,q}(\eta) N_{k,l}(\zeta) \frac{W(\xi, \eta, \zeta) N'_{i,p}(\xi) - \frac{\partial}{\partial \xi} W(\xi, \eta, \zeta) N_{i,p}(\xi)}{W^2(\xi, \eta, \zeta)} \\
\frac{\partial}{\partial \eta} R_{ijk}(\xi, \eta, \zeta) &= w_{ijk} N_{i,p}(\xi) N_{k,l}(\zeta) \frac{W(\xi, \eta, \zeta) N'_{j,q}(\eta) - \frac{\partial}{\partial \eta} W(\xi, \eta, \zeta) N_{j,q}(\eta)}{W^2(\xi, \eta, \zeta)} \\
\frac{\partial}{\partial \zeta} R_{ijk}(\xi, \eta, \zeta) &= w_{ijk} N_{i,p}(\xi) N_{j,q}(\eta) \frac{W(\xi, \eta, \zeta) N'_{k,l}(\zeta) - \frac{\partial}{\partial \zeta} W(\xi, \eta, \zeta) N_{k,l}(\zeta)}{W^2(\xi, \eta, \zeta)}
\end{aligned}
\tag{A.18}
$$

These partial derivatives are essential for various analytical computations and modeling purposes involving NURBS surfaces and solids.